

**DOCTORAL THESIS**

***Advanced Electroactive Materials Derived from Protic Salts and Protic Ionic Liquids  
for Energy Conversion Devices Involving Oxygen Reduction Reaction***

(プロトン性塩及びプロトン性イオン液体から成る電気化学活性材料の酸素還元反応を用いたエネルギー変換デバイスへの展開。)

A Dissertation Submitted to Yokohama National University for the Partial  
Fulfillment of the Requirements for the Degree of

***Doctor of Philosophy in Chemistry***

Submitted by

**MAHFUZUL HOQUE**

**マフズル ホック**

**D15SA591**

March 2018

Department of Chemistry and Biotechnology

**YNU** 横浜国立大学  
YOKOHAMA National University

## ACKNOWLEDGMENTS

To start with, the author would like to convey his profound gratitude towards almighty Allah, the most benevolent, most knowledgeable and most glorious, who aided him to overcome the challenges to complete this dissertation.

With due respect and veneration, the author wishes to express his deepest and sincere appreciation to his thesis supervisor Prof. Masayoshi Watanabe for his in-depth scientific insight and vision. His scholastic suggestions, invaluable directions and persistence for excellence were paramount to the development of this work. Without his prudent guidance, this research would have been impossible. Also, contribution in reviewing and improvement the thesis from the thesis committee members- Prof. Kaoru Dokko, Prof. Shigenori Mitsushima, Prof. Kazuhisa Sakakibara, and Prof. Satoshi Inagaki alongside with Prof. Masayoshi Watanabe are highly appreciated by the author.

Also, the author would like to appreciate the insightful comments and inspiration by Associate Prof. Kazuhide Ueno, and Dr. Hisashi Kokubo during this research.

Furthermore, the author is immensely grateful to Prof. Yoshio Kobayashi, Graduate School of Informatics and Engineering, The University of Electro-Communications for his support in Mossbauer Spectroscopic experiment. Also, for fruitful discussion regarding electrochemical measurement in acidic electrolyte the author conveys his gratitude to Prof. Shigenori Mitsushima and for ICP-AES measurement to Prof. Satoshi Inagaki. The author also feels fortunate to thank Prof. Doug MacFarlane, Department of Chemistry, Monash University, Australia for his kind discussion and encouragement during this work.

The author is also indebted to Dr. Morgan L. Thomas, Dr. Shiguo Zhang and Associate Prof. Muhammad Shah Miran and for their cooperation and undaunted effort for the improvement of this work.

Special thank is due to authors tutor, Kohei Ikeda for assisting in smoother settlement in the living life of Japan. To carry out the work under an amiable environment spontaneous cooperation and kind gestures from all the students, post doc researchers, and secretaries of the laboratory are heartfully appreciated. It will be unjust to mention few only by name.

Overall, to maintain the work without any sort of tense and anxiety heartfelt gratitude is conveyed to his family members, friends and well-wishers both in Japan and in Bangladesh for their relentless care and mental support.

At last but not the least, the author is thankful to his former teachers and professors, especially Prof. Md. Abu Bin Hasan Susan, Department of Chemistry, University of Dhaka, Bangladesh who encouraged and guided him to develop a consistent work ethic towards learning.

(Mahfuzul Hoque)

## SYNOPSIS

Electrochemical energy storage and conversion devices such as – fuel cells can offer alternative solution to the current natural energy sources which have caused serious environmental impacts. The construction of catalyst layer which uses Pt or Pt-alloy covers the major cost of polymer electrolyte membrane fuel cells (PEMFCs) necessitating the development of non-precious metal catalyst as alternative such as- iron. Amongst the wide array of precursors and synthetic strategy, natural or synthetic polymers as carbonaceous precursors has become popular for designing advanced iron doped carbons. Apart from polymeric and macrocyclic complexes, 1,10-phenanthroline (Phen) as a sole precursor for iron doped carbons came into contention owing to the formation of a catalytic active site at high temperature at the edge of the graphene layer (phenanthroline type, Fe-N<sub>2</sub>-C<sub>4</sub>+) irrespective of the precursors reported few years ago. Due to the poor thermal stability of Phen, conventional approaches relied on foreign activating agent, supports or additives to yield high oxygen reduction activity and thereby increasing the complexity and cost of the processes. So, the candidate undertook the challenge of fabrication of an efficient oxygen reduction electrocatalyst from a molecular precursor like Phen via an inexpensive and robust platform without a laborious preparation process, additives and activation technique.

In this study, the candidate has employed a protic salt, that is 1,10-phenanthroline dihydrogen sulfate ([Phen][2HSO<sub>4</sub>]) and iron halide (FeCl<sub>3</sub>) via nanocasting. The candidate has developed an in-depth understanding about the as synthesized iron doped catalyst by using series of spectroscopic techniques such as- Mössbauer, HR-TEM, XPS, XRD and ICP-AES etc. Under 14 wt% of iron loading and carbonization temperature of 900 oC, the prototype catalyst Fe14NDC-9 exhibited impressive activity in 0.1 M KOH. In contrast, Fe14NDC-9 exhibited inferior mass activity in 0.1 M HClO<sub>4</sub>. To improve the performance, Fe14NDC-9 was post treated by hot 2 M HCl to remove acid soluble, inactive inorganic particles and carbonized again at 900 oC to reduce the unstable functional groups (i.e., oxidized forms of carbon, nitrogen and sulfur etc.) at the graphene layer. After that, the catalyst named as Fe14NDC-9-W2M-9 displaying improved mass activity than Fe14NDC-9 under similar experimental conditions. The stability of the catalyst was assessed by chronoamperometry (i-t) and cyclic stability tests. Firstly, chronoamperometric analysis revealed higher retention of current density for Fe14NDC-9 (84.7%) than for Pt/C (77.5%). It was further improved for Fe14NDC-9-W2M-9 (87.9%) stressing the effect of post treatment. RDE voltammograms of Fe14NDC-9 exhibited 99.8% retention of the half-wave potential after 2000 CV cycles in O<sub>2</sub>-saturated 0.1 M KOH, which was comparable to the behavior of Pt/C (98.7%). In addition to this, Fe14NDC-9-W2M-9 also displayed high retention of current density and half-wave potential in 0.1 M KOH. On the other hand, in 0.1 M HClO<sub>4</sub>, Fe14NDC-9-W2M-9 showed higher retention (94.6%) of the half-wave potential after chronoamperometry at 0.7 V in contrast with Pt/C (91.4%). Also, active site responsible for the efficient oxygen reduction reaction has been explored and correlated with the mass activity in both alkaline and acidic solution. Interestingly, the candidate found that mass activity was dependent on the concentration of Nx-Fe and N-g (valley) which can act as a co-catalytic centre in iron doped carbons. The candidate concluded that balance doping of Nx-Fe and N-g (valley) in iron doped carbons which could be controlled by simple synthetic parameters. The candidate also envisaged that careful design of cationic and anionic structure of protic salt and anion of iron salt could be vital to control over the active sites and thus to achieve highly efficient catalyst.

On the contrary, the current PEMFCs operate at 80 oC and requires humidification and the cathode catalyst, that is, Pt or it's alloy get poisoned by CO. So, by increasing the functioning temperature (> 100 oC) of PEMFCs poisoning effect can be suppressed. In that regard, protic ionic liquids (PILs) have been coveted as the potential non-aqueous electrolyte and it has been previously reported that tertiary amine based PILs having only one transferrable proton has shown excellent oxygen reduction activity, for instance, diethylmethylammonium triflate, that is, [Dema][TFO]. But, such protic ionic liquids lacked high proton conductivity. In comparison with water, primary amines also have two protons in their functional group which makes them ideal system to consider for fuel cell applications. In this study, the candidate has attempted extensive series of primary amines with super strong acids such as- triflic acid (TFO), bistriflic acid (TFSA) etc. First breakthrough was obtained by using 2-Ethylhexyl ammonium cation with TFSA anion, that is, [2-Ehexa] [TFSA] which exhibited promising electrochemical activity. Then, to understand their electrochemical behavior with respect to cationic structure, alkyl chain length was varied

and following examples were, 2-Methylbutyl amine and 2-Methylpropyl amine formed corresponding PILs, that is, [2-Mbua] [TFSA], and [2-Mpra] [TFSA]. In terms of bulk properties, in general, such class of PILs showed lower thermal stability than tertiary amine ones measured by TG-DTA as the additional hydrogen bonds are much weaker in primary amine cation in PILs. Additionally, transport properties, such as- viscosity was measured by rheometer found to be much higher at room temperature due to the extensive hydrogen bonding exist in them, but reduced significantly with temperature rise and was comparable with isomeric tertiary amine based PILs at 120 °C. PILs based on amide anion such as [TFSA<sup>-</sup>] have lower activity than oxo anion ([TFO<sup>-</sup>]). For, primary amine [TFO<sup>-</sup>] based PILs were not possible to obtain thereby, the trifluoroacetate [TFA<sup>-</sup>] based primary amine-PILs [2-Mbua][TFA] were investigated as potential electrolyte and compared with [N-Eipra][TFA], and [Dema][TFA] at 80 °C. In such case, FeNDCs were synthesized by varying the cationic structure of the PSs, such as [Phen][HSO<sub>4</sub>], [oPDA][HSO<sub>4</sub>], and [4,4-DmoBpy][HSO<sub>4</sub>] respectively.

## DEDICATION

I Dedicate This Thesis to  
My Wife, Ohi and My family members for their unconditional support

## TABLE OF CONTENTS

ACKNOWLEDGMENTS .....	II
SYNOPSIS .....	III
DEDICATION.....	V
LIST OF SCHEMES.....	3
LIST OF FIGURES .....	3
LIST OF TABLES .....	4
LIST OF EQUATIONS .....	5
Chapter 1 General introduction .....	6
1.1. Perspective on Energy Conversion Devices .....	6
1.2. Electrochemical Reduction of Oxygen as Lynchpin for Sustainable Energy Conversion.....	7
1.3. Iron based Materials Design as Electrocatalyst for Fuel Cells.....	7
1.4. Ionic Liquids .....	9
1.5. Protic Ionic Liquids/salts as Emerging Precursor for Iron Doped Carbons.....	10
1.6. Nanostructuring of Catalysts and Hard and Soft Acid and Base (HSAB) Principle.....	10
1.7. Perspective of Protic Ionic Liquids as Electrolyte for Fuel Cells .....	12
1.8. Primary amine based Protic Ionic Liquids.....	13
1.9. Objectives and research scope of this study .....	13
1.10. Outlines of the current study.....	14
1.11. References.....	15
Chapter 2 Protic salts derived electrocatalyst .....	17
Iron, nitrogen, and sulfur doped mesoporous carbons for oxygen reduction reaction in alkaline and acidic media .....	17
2.1. Introduction .....	17
2.2. Experimental Details.....	19
2.2.1. Synthesis of protic salts.....	19
2.2.2. Synthesis of carbon materials.....	19
2.2.3. Materials characterization .....	19
2.2.4. Electrochemical characterization.....	21
2.3. Results and Discussion .....	23
2.3.1. Structural insight of protic salt derived iron-doped porous carbons.....	23
2.3.2. Catalytic activity and stability of protic salt derived iron-doped porous carbons.....	29
2.4. Conclusion.....	38
2.5. References .....	38
Appendix-A: Supplementary Data .....	43
✧ Illustration for the assignment of Raman bands and XRD peaks: .....	43
Table A 2.1. Mossbauer peak parameters for Fe <sup>14</sup> NDC-9. ....	44
✧ Illustration for the assignment of the peaks in the Mössbauer spectrum: .....	44
Appendix-B: References.....	48

Chapter 3 Protic salts and Protic ionic liquids derived electroactive materials .....	50
Promising oxygen electroreduction performance of iron doped mesoporous carbons in tertiary alkylamine-PILs.....	50
3.1. Introduction .....	50
3.2. Experimental Details.....	51
3.3. Results and Discussion .....	52
3.4. Concluding Remarks.....	53
3.5. References .....	53
Chapter 4 Protic ionic liquids derived electrolyte .....	54
Protic ionic liquids based on primary alkyl amine: Structure-property correlations and understanding their unique properties based on Hydrogen-bonding .....	54
4.1. Introduction .....	54
4.2. Experimental Details.....	55
4.2.1. Synthesis of protic ionic liquids/protic salts .....	55
4.2.2. Physicochemical characterization of protic ionic liquids .....	57
4.3. Results & Discussion .....	58
4.4. Conclusions .....	65
4.5. Note and References.....	65
Chapter 5 Protic salts and Protic ionic liquids derived electroactive materials .....	67
Molecular level tuning of electro-materials based on protic ionic liquids/salts oxygen reduction electrocatalysis: Effect of cationic structure.....	67
5.1. Introduction .....	67
5.2. Experimental Details.....	67
5.2.1. Synthesis of protic ionic liquids/salts.....	67
5.2.2. Synthesis of carbon materials.....	67
5.2.3. Materials characterization .....	67
5.2.4. Electrochemical characterization.....	67
5.3. Results and Discussion .....	67
5.3.1. Structural features of electro-materials based PILs/PSs.....	67
5.3.2. Electrochemical features of electro-materials based PILs/PSs .....	68
5.4. Closing Remarks.....	68
Chapter 6 General Conclusions and PROSPECTS.....	69
6.1. Overall summary .....	69
6.2. Future directions.....	69
6.3. List of publications.....	70
6.4. Other publications by the Author .....	70

## LIST OF SCHEMES

No table of figures entries found.

## LIST OF FIGURES

Fig. 1.1. (a) Image of fuel cell stack of polymer electrolyte membrane fuel cells, (b) Polarization curve shows the relationship between cell voltage and current density to evaluate cell performance. The various losses are also indicated in the same figure including their sources. ....	6
Fig. 1.2. Schematic representation of the qualitative Sabatier principle. ....	8
Fig. 1.3. Conventional and novel precursors for iron doped carbons. ....	9
Fig. 1.4. Schematic illustration for the design of doped carbon materials using PILs/PSs. ....	10
Fig. 1.5. Nanostructuring of iron doped carbons utilizing HSAB principle. ....	11
Fig. 1.6. PILs as electrolyte in intermediate temperature fuel cells under non-humidified condition. ....	12
Fig. 1.7. Isomeric structure of primary, secondary, and tertiary alkylamines. ....	13
Fig. 1.8. Structure of primary alkylamines used in this study. ....	14
Fig. 2.1. Schematic illustration of nanocasting synthesis of iron-doped porous carbons by direct carbonization of a mixture of a protic salt, a simple iron salt, and colloidal silica, LUDOX HS-40. ....	18
Fig. 2.2. Electrochemical cell design. ....	21
Fig. 2.3. HRTEM micrographs of (a, c) Fe14NDC-9, and (b, d) Fe14NDC-9-NT. Circles indicate mesopores and arrows indicate bent graphitic layers at the edge of the carbon. ....	24
Fig. 2.4. (a) Raman spectra (b) Adsorption-desorption isotherms, (c) BJH plots, and (d) 2D-NLDFT plots. ....	25
Fig. 2.5. t-plots for doped carbons showing presence of micropores. ....	25
Fig. 2.6. (a) Mössbauer spectrum, (b) Schematic representation of various bonding configurations of heteroatoms (Fe, N, S and O) in Fe14NDC-9. High resolution (c) N1s, (d) Fe2p, (e) S2p, and (f) C1s XPS spectra. ....	27
Fig. 2.7. Atomic concentration for nitrogen (Table S3) and its different configurations with the binding energy range for each site obtained from the deconvoluted N1s HR-XPS spectra (Fig. A 2.2, and Table A 2.3). ....	27
Fig. 2.8. (a) Survey XPS spectra, (b) enlarged view of Fe2p survey spectra, (c) Fe2p HR-XPS deconvoluted spectrum, and (d) TG-DTA curves under 100 mL min <sup>-1</sup> flow rate of O <sub>2</sub> . ....	28
Fig. 2.9. EDS elemental mapping image of Fe14NDC-9 showing the distribution of carbon, nitrogen, oxygen, sulfur, and iron over the selected area of FE-SEM image of the corresponding sample. ....	29
Fig. 2.10. (a) RDE voltammograms showing disk current density in O <sub>2</sub> -saturated 0.1 M KOH at a scan rate of 10 mV s <sup>-1</sup> under rotation rate of 1600 rpm. (b) RDE voltammograms as a function of rotation rate (600–2500 rpm) and the corresponding (c) Koutecky-Levich plots at potentials from 0.85 to 0.75 V. (d) Tafel plots. In all cases, the temperature was 25 °C and the loading amounts of NPM-based catalyst and Pt/C were 600 μg cm <sup>-2</sup> and 50 mg <sub>Pt</sub> cm <sup>-2</sup> respectively. ....	29
Fig. 2.11. RRDE voltammograms of (a) NDCs, (b) FeNDCs, and (c) Pt/C showing the disk and ring current densities at various rotation speeds in O <sub>2</sub> -saturated 0.1 M KOH after capacitive current correction. (d) calculated electron transfer number and peroxide yield based on the ring current densities as shown in Fig. S5a-c. Temperature was set at 25 °C and the loading amounts of NPM-based catalyst and Pt/C were 600 μg cm <sup>-2</sup> and 50 μg <sub>Pt</sub> cm <sup>-2</sup> respectively. ....	30
Fig. 2.12. RRDE voltammograms for iron doped carbons showing disk and ring current densities and the calculated electron transfer number based on the ring current densities for (a,c,e) alkaline (0.1 M KOH) and (b,d,f) acidic (0.1 M HClO <sub>4</sub> ) electrolytes respectively in O <sub>2</sub> -saturated under 1600 rpm with scan rate of 10 mV s <sup>-1</sup> at 25 °C. Loading of the catalyst was 600 μg cm <sup>-2</sup> . ....	31
Fig. 2.13. (a) LSV in 0.1 M KOH and 0.1 M HClO <sub>4</sub> , deconvoluted (b) N1s, (c) Fe2p, and (d) S2p XPS spectra. ....	32

Fig. 2.14. (a) RRDE voltammograms showing the disk and ring current densities, and (b) K-L plot between 0.6 to 0.7 V in O <sub>2</sub> -saturated 0.1 M HClO <sub>4</sub> under 1600 rpm with scan rate of 10 mV s <sup>-1</sup> at 25 °C. Loading of the catalyst was 600 μg cm <sup>-2</sup> .....	32
Fig. 2.15. RRDE voltammograms as a function of (a) carbonization temperature, (b) iron loading showing the disk and ring current densities in O <sub>2</sub> -saturated 0.1 M KOH 1600 rpm with scan rate of 10 mV s <sup>-1</sup> at 25 °C. Loading of the catalyst was 600 μg cm <sup>-2</sup> .....	33
Fig. 2.16. Change in onset potential and mass activity of carbons as a function of (a) annealing temperature, and (b) iron loading in 0.1 M KOH. Mass activity correlation plot with respect to (c) N <sub>x</sub> -Fe, and (d) N-g (valley). Onset potential was calculated from the LSV of each sample shown in Fig. S6a, S8a, c, and S9a. Content of N <sub>x</sub> -Fe, and N-g (valley) was taken from Table S3 which is also shown as a bar chart in Fig. 5.....	33
Fig. 2.17. RRDE voltammogram of FeNDCs showing (a) disk (inset: TEM micrograph) and (b) ring current density in O <sub>2</sub> -saturated 0.1 M KOH 1600 rpm with scan rate of 10 mV s <sup>-1</sup> at 25 °C. Loading of the catalyst was 600 μg cm <sup>-2</sup> .....	34
Fig. 2.18. Mass activity of FeNDCs as a function of N-py in 0.1 M KOH.....	35
Fig. 2.19. Effect of iron loading from 3.5 to 28 wt.% in a 2.0 g mixture of protic salt and FeCl <sub>3</sub> combined with colloidal silica.....	36
Fig. 2.20. (a) Chronoamperometry (i-t) at 0.8 V under 1600 rpm, (b) retention of current density and half-wave potential after 10000s, and 2000 CV cycles, (c-d) LSV before and after 2000 CV cycles. All the experiments were conducted in O <sub>2</sub> -saturated 0.1 M KOH and 0.1 M HClO <sub>4</sub> .....	37
Fig. 2.21. RDE voltammograms before and after (a-c) 2000 cycles cyclic stability test in 0.1 M KOH, and (d) chronoamperometric test in 0.1 M HClO <sub>4</sub> .....	37
Fig. 4.1. Structure of amines and acids employed in this study.....	55
Fig. 4.2. Schematic presentation of the synthesis of PILs/PSs.....	56
Fig. 4.3. Thermo-gravimetric curves for PILs with the variation in (a) alkyl chain length, and (b) number of hydrogen bond donors.....	58
Fig. 4.4. (a) Thermogravimetry curves of primary alkylamine-PILs showing the effect of anionic structure. (b) Thermal properties of all the PILs/PSs synthesized in this work.....	58
Fig. 4.5. Primary alkylamine (2-Ethylhexylamine) based PILs/PSs with the variation in the (a) alkyl chain length of cations, and (b) oxo-acids.....	59
Fig. 4.6. (a) DSC patterns of PILs, (b) FT-IR spectra of the neutral amine 2-Mbua and PILs.....	60
Fig. 4.7. Possible interaction sites for H-bonds and networking H-bonds in protic ionic liquids depending on the number of H-bond donors in the structure of cation.....	60
Fig. 4.8. FT-IR spectra of [2-Ehexa][TFSA] in comparison with [Dema][TFSA] at room temperature.....	61
Fig. 4.9. <sup>1</sup> H-NMR spectra of (a) primary amine (neutral) and the corresponding PILs, (b) PILs with primary and secondary amine cations measured at 40 °C.....	61
Fig. 4.10. Change of viscosity as a function of shear rate (a) at 25 °C, (b) under various temperatures. For Fig.3b, shear rate was limited to 4000 s <sup>-1</sup> at higher temperatures due to the expelling of the samples at very high shear rate.....	62
Fig. 4.11. Change of viscosity as a function of shear rate under various temperatures. Shear rate was limited to 4000 s <sup>-1</sup> from 40 °C due to the expelling of the samples at very high shear rate.....	62
Fig. 4.12. (a) Change of viscosity and conductivity as a function of temperature, (b) Walden plot (25 °C–40 °C).....	64
Fig. 4.13. Viscosity and conductivity as a function of temperature for (a) secondary and (b) tertiary amine-PILs.....	64

## LIST OF TABLES

Table 1.1. List of ORR reactions and their complementary thermodynamic potentials at ambient conditions in different reaction media.....	7
Table 2.1. Details of the preparation conditions for carbons.....	24

## LIST OF EQUATIONS

$\Delta G = nFE_{\text{cell}}$ (Eq. 1.1).....	6
$\eta = \eta_{\text{activation}} - \eta_{\text{ohmic}} - \eta_{\text{mass-transport}}$ (Eq. 1.2).....	6
$E_{\text{vs RHE}}^{\text{fuel cell}} = E_{\text{vs Ag/AgCl}}^{\text{activation}} + 0.209 + 0.059 \text{ pH}$ (Eq. 2.1).....	21
$J_k = J_D J_{D_0} - J$ (Eq. 2.2).....	22
$1J = 1B\omega_1 / 2 + 1J_k$ (Eq. 2.3).....	22
$B = 0.201nFC_{\text{CoDo2}} / 3v - 1 / 6$ (Eq. 2.4).....	22
$1J_k = 1nFkCo$ (Eq.2.5).....	22
$J_m = J_k (0.8 \text{ V vs RHE})L_{\text{cat}}$ (Eq. 2.6).....	22
$J_k = J_k 0.8 \text{ V vs RHE} * J_{\text{Lim}}/J_{\text{Lim}} - J_k (0.8 \text{ V vs RHE})$ (Eq. 2.7).....	23

## LIST OF FIGURES: APPENDIX-A

Fig. A 2.1. (a,b) Raman spectra, (c) XRD, and (d,e) Reference XRD pattern. ....	43
Fig. A 2.2. N1s HR-XPS spectra of doped carbons.....	46

## LIST OF TABLES: APPENDIX-A

Table A 2.1. Mossbauer peak parameters for Fe14NDC-9.....	44
Table A 2.2. List of XPS binding energy peak of different bonding configurations of nitrogen in doped carbons. ....	45
Table A 2.3. Atomic concentration for nitrogen and its different configurations. ....	46
Table A 2.4. ORR performance comparison between current study and earlier reports.....	47
Table A 2.5. Atomic concentrations of the elements determined from XPS survey spectra, specific surface areas and total pore volumes estimate from the adsorption-desorption isotherms via BET analysis method. ....	47

1.1. Perspective on Energy Conversion Devices

Unprecedented climate change in past few decades have been accelerated by the record-breaking outburst in CO<sub>2</sub> emissions owing to the fossil fuel based industrial revolutions since mid-19<sup>th</sup> century.<sup>1</sup> So, reduction of greenhouse gas emission is rudimentary which could be met by the concerted effort from multidisciplinary approach reinforced by Paris Agreement recently.<sup>2</sup> Owing to the depletion of reserve of fossil fuels and high safety-risk in nuclear based energy system, a paradigm shift in energy policy has taken place in most countries which is based on renewable and sustainable energy production.<sup>3</sup> Conventional fossil fuels based automobiles generate ~75% of the world-wide CO<sub>2</sub> emissions caused via transportation sector.<sup>4</sup> Electrochemical energy conversion devices transform chemical energy into electrical energy offer cleaner and relatively better environmental impact.<sup>4</sup> So, there has been an upsurge in interest in pure battery electric vehicles (BEVs), as well as hybrid electric vehicles and fuel cell electric vehicles (FCEVs).<sup>5</sup> Unlike batteries, fuel cells (FCs) do not need recharging as long as hydrogen as fuel is in supply, yet they are pivotal to the establishments of the concept of “Electromobility”.<sup>4</sup> Amongst all the variants of FCs, hydrogen powered FCEVs which utilizes a polymer electrolyte membrane fuel cell (PEMFC). On top of that, such systems are also promising for stationary power plants and co-generation of heat and power (CHP)<sup>5</sup> owing to its facile design and robust performance. In a PEMFC chemical energy is converted into electrical energy via a redox chemical reaction between hydrogen (fuel) and oxygen (oxidant) as shown **Fig. 1.1.1**.<sup>6</sup> The electrolyte could be both aqueous (water, solution of mineral acids or bases) and non-aqueous media (organic proton conducting media) separated by a proton exchange membrane (i.e., Nafion in humidified condition).<sup>7</sup>

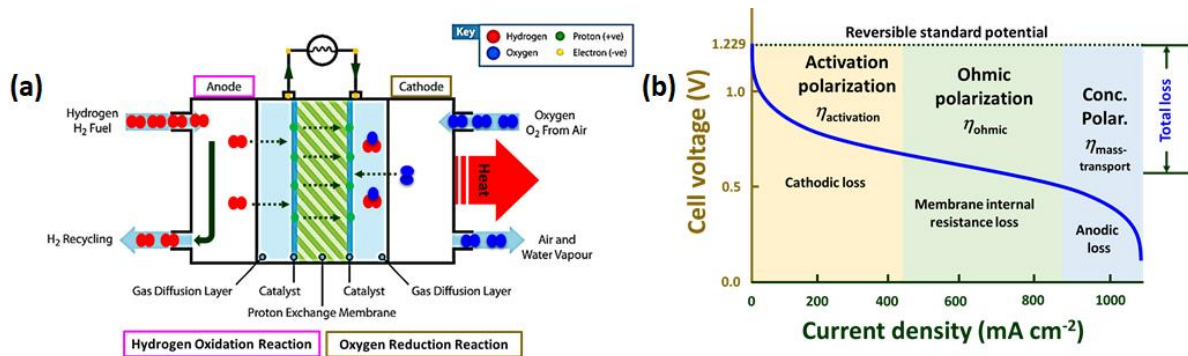


Fig. 1.1. (a) Image of fuel cell stack of polymer electrolyte membrane fuel cells, (b) Polarization curve shows the relationship between cell voltage and current density to evaluate cell performance. The various losses are also indicated in the same figure including their sources.

The efficiency of the reaction is thus crucial to the energy output of the system. Based on thermodynamic calculation (**Eq. 1.1**), efficiency ( $\eta_{\text{theory}}$ ) of the fuel cells is ~90%. But it can only achieve  $\eta_{\text{fuel cell}} \sim 56\text{-}64\%$  (0.7 V-0.8 V) in practice<sup>8</sup> due to the losses pertaining to activation overpotential for the reaction, ohmic resistance, and mass transport losses (**Eq. 1.2**).<sup>9</sup>

$$\Delta G = nFE_{\text{cell}} \tag{Eq. 1.1}$$

$$\eta_{\text{fuel cell}} = \eta_{\text{activation}} - \eta_{\text{ohmic}} - \eta_{\text{mass-transport}} \tag{Eq. 1.2}$$

The efficiency of the fuel cell depends on the reaction overpotential rather than Carnot cycle as for combustion engine. The origin of such deficiency comes from the oxygen reduction reaction at the cathode

which is sluggish kinetically owing to the requirement of the breaking of strong double of oxygen to initiate the reaction.<sup>10</sup> Thus, deployment of a catalyst is quintessential to achieve high thermodynamic efficiency of the fuel cell. In commercial, FCEVs, for instance MIRAI (“future” in Japanese) utilizes a platinum-cobalt alloy as cathode catalyst.<sup>5</sup> But, despite the increase in 1.8-fold mass activity compared to platinum (usual loading  $\sim 0.4 \text{ mg cm}^{-2}$ ), still the price of the vehicle is beyond the reach of the mass level consumers. So, despite the many technical challenges in the commercial realization of FCEVs, high cost of materials, i.e., Pt in the construction of cathode of the fuel cell has been remain the major bottleneck.<sup>11</sup> Therefore, replacing it completely with an earth-abundant and low-cost metal will foster the growth of the market of FCEVs.

### 1.2. Electrochemical Reduction of Oxygen as Lynchpin for Sustainable Energy Conversion

In FCs, reaction involving the anode such as hydrogen oxidation reaction (HOR) is faster than the oxygen reduction at the cathode. Kinetics of ORR is intrinsically slow requires a boost via a catalyst to reach a practical usable level in a fuel cell. Electrocatalytic ORR involves several reaction steps at the electrode-electrolyte interface rendering complicated reaction mechanism which varies depending on the type of electrolytes, and electrode materials. Generally, aqueous and non-aqueous (e.g. protic ionic liquids)<sup>11</sup> medium it follows two pathways: the direct 4-electron reduction pathway from  $\text{O}_2$  to  $\text{H}_2\text{O}$ , and the 2-electron reduction pathway from  $\text{O}_2$  to hydrogen peroxide ( $\text{H}_2\text{O}_2$ ). Despite the media, 4e transfer is desirable for practical purposes. Several typical ORR processes with their corresponding thermodynamic electrode potentials at standard conditions are listed in **Table 1.1**.<sup>12</sup>

Name of electrolyte	ORR reactions	Electrode potential, V (ambient condition)
<b>Acidic solution (aqueous)</b>	$\text{O}_2 (\text{g}) + 4\text{H}^+ (\text{aq}) + 4\text{e}^- \rightarrow \text{H}_2\text{O} (\text{l})$	1.229
	$\text{O}_2 (\text{g}) + 4\text{H}^+ (\text{aq}) + 2\text{e}^- \rightarrow \text{H}_2\text{O}_2 (\text{l})$	0.70
	$\text{H}_2\text{O}_2 (\text{l}) + 2\text{H}^+ + 2\text{e}^- \rightarrow 2\text{H}_2\text{O} (\text{l})$	1.76
<b>Alkaline solution (aqueous)</b>	$\text{O}_2 (\text{g}) + \text{H}_2\text{O} (\text{l}) + 4\text{e}^- \rightarrow 4\text{OH}^- (\text{aq})$	0.401
	$\text{O}_2 (\text{g}) + \text{H}_2\text{O} (\text{l}) + 2\text{e}^- \rightarrow \text{HO}_2^- (\text{aq}) + \text{OH}^- (\text{aq})$	-0.065
	$\text{HO}_2^- (\text{aq}) + \text{H}_2\text{O} (\text{l}) + 2\text{e}^- \rightarrow 3\text{OH}^- (\text{aq})$	0.867
<b>Protic ionic liquids (non-aqueous)</b>	$\text{O}_2 (\text{g}) + 4\text{H}^+ (\text{aq}) + 4\text{e}^- \rightarrow \text{H}_2\text{O} (\text{l})^*$	1.229

\* Protons are carried via protic ionic liquids via vehicular (V) or Grotthuss (G) mechanism. Details are given in section 1.7.

Table 1.1. List of ORR reactions and their complementary thermodynamic potentials at ambient conditions in different reaction media.

Until now, Pt-based materials are the most practical catalysts despite their cost and scarcity. So, usage of transition metals such as iron instead of platinum and its alloys has created much interest owing to their availability and competitive performance regarding precious metal ones.<sup>13</sup>

### 1.3. Iron based Materials Design as Electrocatalyst for Fuel Cells

Abundance of materials is paramount to the fabrication of any technological device. But, high crustal opulence does not ensure availability. Considering that iron is by far the best element in terms of mass production and market value.<sup>14</sup> Catalytic potency of iron based materials has been well-known in  $\text{NH}_3$  production,<sup>15</sup> Fischer-Tropsch synthesis<sup>16</sup> of hydrocarbon from syngas (a mixture of hydrogen and carbon monoxide) and high temperature water-gas shift reaction.<sup>17</sup> Although qualitative, Sabatier principle<sup>18</sup> can infer that the best catalysts should bind atoms and

molecules with an intermediate strength: not too weakly to be able to activate the reactants, and not too strongly to be able to desorb the products. This results to a volcano-type relationship between activity and bond strength as displayed in **Fig. 1.2**.<sup>16</sup> Iron is located at the strong binding side of the volcano curve (**Fig. 1.2**). For ORR, iron based materials have been designed in various forms such as iron based co-ordination complex,<sup>19</sup> iron co-ordinated by nitrogen integrated in the Basal plane of carbon lattice,<sup>20</sup> and iron capped by graphitic layers also known as core@shell structures.<sup>20</sup> So, the co-ordination chemistry of iron has been the driving force in controlling the surface chemistry of iron during catalytic processes, such as ORR.<sup>21</sup>

Iron based molecular catalysts, for instance macrocyclic complexes of phthalocyanines and their pyrolyzed analogues have been the focal point for oxygen reduction electrocatalysis.<sup>19</sup> Annealing of non-macrocyclic complex of iron such as Fe-Phenanthroline has also been utilized as catalyst.<sup>19</sup> Iron as a non-complexing compound (i.e. FeCl<sub>3</sub>) require an additional precursor in which options are diverse and innumerable as shown in **Fig. 1.3**.<sup>20</sup> Natural and synthetic polymers for example polyaniline, polypyrrole etc. and specially designed metal-organic frameworks (MOFs) such as ZIF-8 (**Fig.**

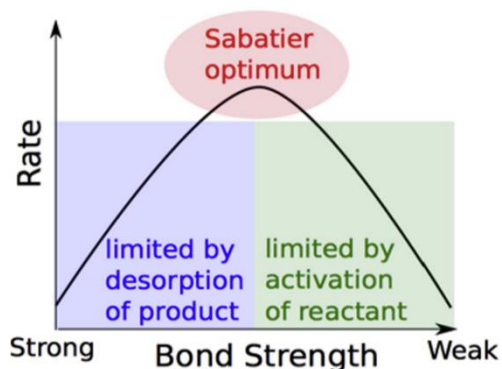


Fig. 1.2. Schematic representation of the qualitative Sabatier principle.

**1.3**) has been most popular amongst the researchers as carbonaceous precursor owing to their thermal stability and flexible building block design. In most cases, alongside the precursors, catalyst support materials with high surface area is added in the mixture of iron and carbon precursors. Most common examples are Ketjen black (KB), acetylene black (AB), black pearl, super P etc. Muckerjee et. al.<sup>21</sup> reported that Relatively well-ordered carbon supports such as graphite, acetylene black, and super-P surfaces yielded lower turnover number for ORR. On the contrary, highly disordered carbon supports such as activated carbon, ketjen EC600JD, and black pearl yielded higher turnover number. Shao-Horn et. al.<sup>22</sup> demonstrated the superior mass activity of iron and nitrogen doped carbons (Fe-N-rGO) synthesized from the mixture of FeCl<sub>3</sub>, graphitic carbon nitride g-C<sub>3</sub>N<sub>4</sub>, and reduced graphene oxide (rGO). Via using multi-walled carbon nanotube (MWCNT) as an alternative to rGO, excellent catalytic performance was also reported by the same group<sup>23</sup> in which type of iron salt affected the mass activity significantly. Very recently, carbon materialization of ionic liquids<sup>25</sup> has created lot of excitement amongst the materials scientists as a novel precursor system for iron doped carbons. Overall, from materials design perspective, type of carbon precursor, support material, and iron salt influence the mass activity of the iron doped carbons vehemently. Apart from that, preparation of iron doped carbons via pyrolysis is also quite flexible approach. High thermal treatment (HTT) process is a kinetic phenomenon, thus during carbonization process many synthetic variables for instance heating rate, holding time, flow rate of gas, type of gas (Ar or NH<sub>3</sub>) can be altered to fine-tune the properties of the iron doped carbons, in particularly, content of heteroatoms, graphitic degree, surface area etc.

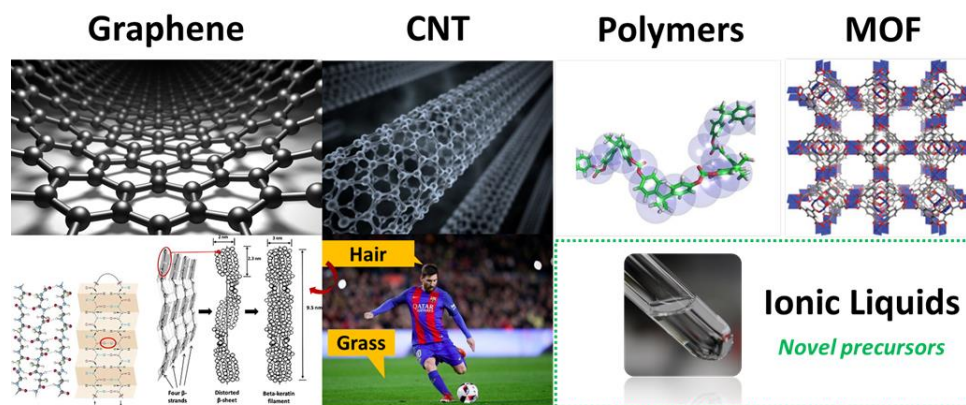


Fig. 1.3. Conventional and novel precursors for iron doped carbons.

#### 1.4. Ionic Liquids

Ionic liquids (ILs) are salts in liquid phase at the temperature of interest composed solely of ions. They are considered as “designer solvents”, one of their many superlatives due to the intrinsic variability of the cations and anions. Since its development from early 19<sup>th</sup> century, it has gone under several stages of evolution and can be classified into many branches and sub-branches.<sup>26</sup> But, generally, ILs are categorized into two types, that is, aprotic ionic liquids (AILs), and protic ionic liquids (PILs). The major research on ILs has been concentrated on their solvent behavior in electrochemical storage and conversion devices owing to their wide electrochemical window.<sup>11</sup> Recently, ILs has leapfrogged from conventional solution chemistry into materials science such as heteroatoms (nitrogen/sulfur/phosphorous/boron) doped carbons. Due to their carbon rich nature, negligible vapor pressure and high thermal stability carbon materialization of ILs (here is AILs) was initiated by the group of Markus Antonietti and Sheng Dai.<sup>25</sup> Most organic precursors usually vaporize at the initial stages of thermal annealing process resulting poor yield. Polymeric precursors require complicated multistep reactions and purification procedures.<sup>11</sup> On top of that solubility of the metal precursors with polymers is a serious issue. Functionalization of the metallic nanoparticles resolve such problem yet further complicating and increasing the overall cost of the synthesis processes.<sup>27</sup> Metal-organic Frameworks (MOFs) are still quite expensive and in most cases, additional high surface area carbon supports are necessary to exert suitable features.<sup>11</sup> Although being lesser in complexity than polymer synthesis, AILs also require multistep reactions and not cost-effective as well.

Therefore, it is paramount to develop a platform for carbon precursor to synthesize iron doped carbons which is not only easy to implement industrially but also low-cost and flexible for the continuous improvement of the materialistic features. So, in this thesis protic ionic liquids/salts (PILs/PSs) has been outlined as the potential candidate to fabricate efficient iron doped carbons.

### 1.5. Protic Ionic Liquids/salts as Emerging Precursor for Iron Doped Carbons

PILs/PSs are synthesized simply via certain Bronsted acid-Bronsted base reaction at stoichiometric compositions. Then, they can be directly subjected to carbonization process at ambient pressure without any prepolymerization steps and post treatment procedures as shown in **Fig. 1.4**. Overall, this approach is devoid of any complicity. PILs/PSs are also designable at the molecular level akin to that of ALLs. So, the properties of the carbons such as carbon yield, surface area, conductivity, porous structure and graphitic degree etc. are easily tunable by varying the cationic and anionic structures (**Fig. 1.4**). Cationic structure (e. g. non-functional amine) usually bestow nitrogen as a dopant and the type of co-dopants (S/P/B) depend on the choice of anions, such as N, S co-doping in the case of sulfuric acid. During carbonization process, the PILs/PSs undergo several complicated kinetically controlled processes aided by the both anions and cations. If the cation is non-functional as mentioned earlier, selection of the anion is quite vital. Until now, detail study about the effect of anion is yet to be explored. But, using sulfuric acid as the anionic source, that is hydrogen sulfate [ $\text{HSO}_4$ ], carbon yield of PILs/PSs derived carbon was found to be highest which is important from commercial perspective. Sulfuric acid also quite strong acid yields  $\Delta\text{pK}_a$  ( $\text{pK}_a$  difference between the acid and base precursors) in the range from medium to high depending on the acidity of the cation of PILs/PSs. Hydrogen sulfate can form inter-anionic hydrogen bonding network via the additional proton in its structure which may facilitate the formation of framework structure *in-situ* at lower temperature regime and then undergo cross-linking/oxidative polymerization and partial condensation to form polycyclic aromatic compounds and finally transform into nitrogen and sulfur doped carbon via rapid removal of low molecular weight gases such as  $\text{H}_2\text{O}$  and  $\text{SO}_2$ . In the seminal work by Zhang et. al.<sup>28</sup> Nitrogen doped carbons exhibited ORR activity in alkaline solution. Iron doped carbons has been reported from ALLs platform by Strasser et. al.<sup>29</sup> and exhibited good ORR performance. But, the mass activity was low and Ketjen black (KB) was used as support material. No attempt has been made so far for the fabrication of iron doped carbons utilizing PILs/PSs.

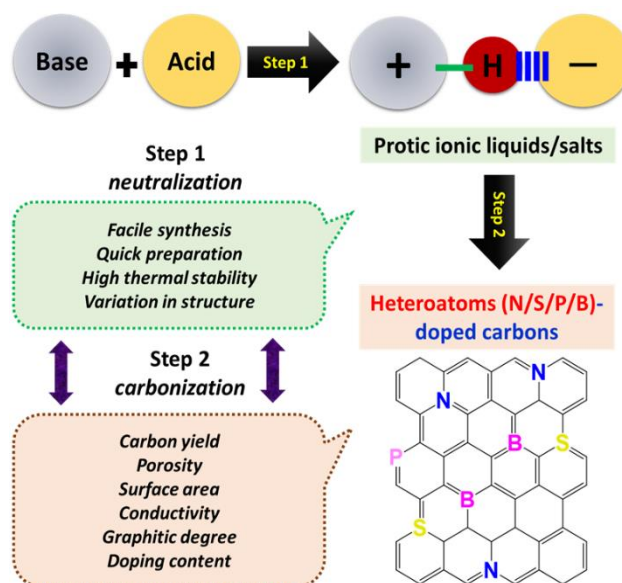


Fig. 1.4. Schematic illustration for the design of doped carbon materials using PILs/PSs.

### 1.6. Nanostructuring of Catalysts and Hard and Soft Acid and Base (HSAB) Principle

Nanostructure engineered materials are at heart of advanced electroactive materials research due to their high specific surface area. 3D porous topology coupled with high surface area is important regarding access and utilize the active site of the catalysts, efficient mass-transport of reactants ( $\text{O}_2$ ,  $\text{H}^+$ ,  $\text{e}^-$ ) and products ( $\text{H}_2\text{O}$  gas,  $\text{H}_2\text{O}$  liquid, and heat) during ORR.<sup>6</sup> In PILs/PSs platform, porous architecture is greatly dependent on the structure of the cations and anions. For example, allylammonium hydrogen sulfate,  $[\text{Allyl}][\text{HSO}_4]$  exhibited microporous structure with high surface area owing to the cross-linking polymerization provided by the double bond

of the cation.<sup>30</sup> On the contrary, para phenylenediammonium dihydrogen sulfate, [pPDA][2HSO<sub>4</sub>] yielded mesoporous structure owing to the self-oxidative polymerization supported by the amino groups at para position.<sup>31</sup> Also, adenium bis(trifluoromethane sulfonimide), [Adn][TFSA] resulted mesoporous NDCs due to the removal SO<sub>2</sub> from the anion.<sup>32</sup> But, in most cases, narrow distribution of micro/mesopores is difficult to achieve via simple molecular precursors. So, by using a template such as colloidal silica, it is possible to imprint 3D uniform porous network in the carbon materials. In such cases, selection of the size of particles of silica and suitability of the precursors and template are crucial factors. In such case, colloidal silica is commercially available with various sizes, nanostructures and properties. LUDOX<sup>®</sup> HS-40 colloidal silica is a 40 wt.% suspension of 12 nm silica in water.<sup>33</sup> It has been reported by Banham et. al.<sup>34</sup> that colloidal imprinted Pt/C (CIC-15) prepared via utilizing such template exerted better catalytic activity than the other silica suspensions with various sizes ranging from 22 nm to 80 nm. Disordered hexagonal close packing (hcp) arrangements resulted much thicker walls favoring facile oxygen diffusion and proper utilization of the active sites and thus the activity of the catalysts. Zhang et. al., demonstrated that PS, that is [Phen][2HSO<sub>4</sub>] was compatible with LUDOX<sup>®</sup> HS-40 resulting high surface area and narrow pore size distribution. Recently, [Adn][TFSA] also displayed similar results. NDCs from both reports showed good catalytic activity under alkaline media.<sup>32</sup> Using PSs, efficient catalyst in both alkaline and acidic media is yet to be reported.

To synthesize, iron doped carbons, transition metals in general choice of cationic structure is vital pertaining to the miscibility of the iron salt with the PILs/PSs. 1,10-phenanthroline (Phen) is known for its strong binding affinity towards iron. Also, ortho phenylenediamine (oPDA) and ortho bipyridine (oBpy) derived PILs/PSs could be suitable candidate. In such case, anion of the iron salt is also important. For example, FeCl<sub>3</sub> is soluble with [Phen][2HSO<sub>4</sub>]; but, not Fe(SCN)<sub>3</sub>. This is in accordance with Hard and Soft Acid and Base principle (HSAB) as shown in **Fig. 1.5**. PSs, such as [oPDA][2HSO<sub>4</sub>], and [oBpy][2HSO<sub>4</sub>] also exhibit the same trend as well transition metals other iron (**Fig. 1.5**).

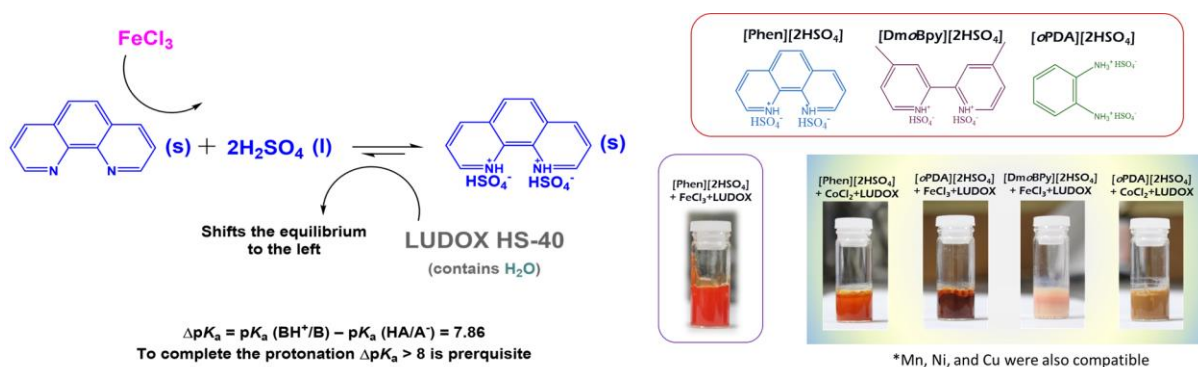


Fig. 1.5. Nanostructuring of iron doped carbons utilizing HSAB principle.

### 1.7. Perspective of Protic Ionic Liquids as Electrolyte for Fuel Cells

Polymer electrolyte membrane fuel cells (PEMFCs) technology conventionally operate below 80 °C to keep the membrane (Nafion) moist. The benefit of such variant of FCs is higher power density and quicker start-up but suffer from complex water management and CO poisoning of the catalyst. In a mineral acid-based system such as phosphoric acid (H<sub>3</sub>PO<sub>4</sub>) based FCs, operational temperature can be extended up to 200 °C. That overcomes few issues regarding fuel purity as at high temperature rendering very low CO tolerance limit. Design of the cell becomes also simpler via the exclusion of the humidifier. But, H<sub>3</sub>PO<sub>4</sub> causes corrosion of the catalyst layer. Angel et. al. recently showed that H<sub>3</sub>PO<sub>4</sub> functionalized silica (silicophosphate electrolyte, SiPOH) demonstrating excellent stability as well as activity. Quasi-solid electrolytes also suffer from cold start problem and sulfur sensitivity.

Thus, liquid electrolytes which can withstand wider operational temperature range is highly desirable. Protic ionic liquid as a non-

aqueous proton conducting electrolyte is a viable candidate beyond aqueous systems (**Fig. 1.6**). Susan et. al. from Watanabe group first demonstrated electrochemical activity of PILs as FCs electrolyte which sparked great drive in the FCs research community. Later, Nakamoto et. al. developed a PIL, that is diethylmethylammonium trifluoromethanesulfonate [Dema][TFO], exhibiting high activity and benign transport properties. Lee et. al. also showed using a PIL modified sulfonated polyimide (SPI) membrane and PILs as electrolyte non-humidified FCs could display reasonable performance. Angell and his co-workers reported that in PILs the extent of proton transfer during their synthesis by stoichiometric acid-base neutralization reaction is dictated by the  $\Delta pK_a$ .  $\Delta pK_a > 2$  is prerequisite for the initiation of proton transfer which becomes almost complete (>98%) approximately at  $\Delta pK_a > 8$  showed by group of McFarlane. Miran et. al. later mentioned that to obtain PILs with high thermal stability and ionicity  $\Delta pK_a > 15$  is prerequisite. After rigorous exploration using tertiary amine as cationic source, such as [Dema<sup>+</sup>], [Dema][TFO] has been the benchmark PIL till date having moderately high  $\Delta pK_a$  (17). Molecular level reason is still unclear. But, another PIL from tertiary amine system which is ethylmethylpropylammonium nonafluorobutanesulfonate [Empa][NFO] also displayed high activity like [Dema][TFO]. Varying anionic structure based on amide acids, Kanamura et. al. showed that [Dema][BETA] showed higher open circuit potential (OCP) owing to the non-adsorbing nature of the [BETA] anion in contrast with [Dema][FSA], and [Dema][TFSA].

Apart from being used as electrolyte PILs has been effectively deployed to boost activity of Pt/C by enhancing the ionic conduction process. In the pioneering work of Erlebacher's group, hydrophobic PILs ([MTBD][BETA]) coated NiPt nanoporous metal alloy nanoparticles [np-NiPt/C+[MTBD][BETA]] exhibited an order of magnitude in enhancement in activity comparing with Pt/C in acidic electrolyte. Later, Brennecke et. al. also demonstrated that the selection of anion and composition of PILs were vital to achieve an efficient performance of the electrocatalyst. Pt/C+[MTBD][NFO] displayed the highest specific activity in 0.1 M HClO<sub>4</sub>.

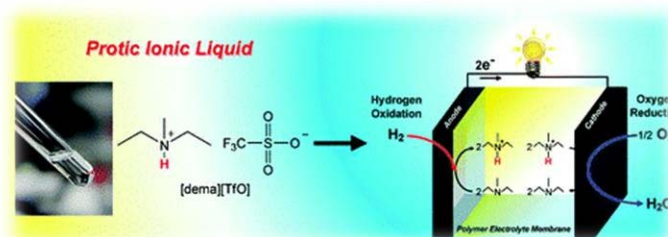


Fig. 1.6. PILs as electrolyte in intermediate temperature fuel cells under non-humidified condition.

### 1.8. Primary amine based Protic Ionic Liquids

Ethylammonium nitrate [EAN] is one of the beacon of ILs research founded by Walden in 1914. Since then despite the expansion of variants of ILs, primary amine-PILs has been the most difficult to materialize. The major bottleneck lies in their structure which dictate the thermodynamics of their phase behavior via subtle balance between Coulombic and supramolecular interactions such as hydrogen bonding (H-bonding). Primary amine has two additional protons providing less asymmetry which in turn result increase in the covalent character of H-bonds. Stronger H-bonding effect reduces the entropy of the system and thereby solidification of PILs. Both research group of Ludwig and Atkin have confirmed the existence of strong, dense and co-operative H-bonding in [EAN]. Beyond [EAN], reports on primary amine-PILs have become scarce.

To understand the molecular level reason, especially the role of protonic species which is the ammonium cation, cationic structural variation is key. By changing from tertiary amine to secondary and primary amine via isomeric structural variation, effect of the proton conducting moiety could be possible to unravel (**Fig. 1.7**). In this work, an extensive range of primary amines have been explored as the potential cationic segment of primary amine-PILs.

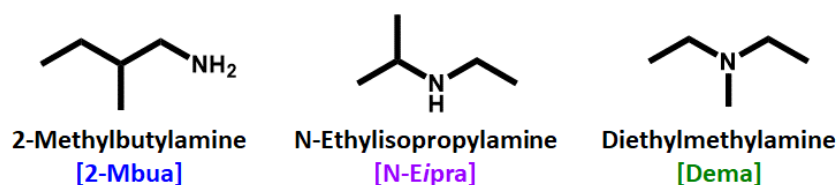


Fig. 1.7. Isomeric structure of primary, secondary, and tertiary alkylamines.

### 1.9. Objectives and research scope of this study

The primary objectives and scope of the current study is outlined as follows:

- ✧ To develop a robust and simple materials design of Fe, N, and S co-doped carbons (FeNDCs) via nanocasting approach based on protic salt.
- ✧ To provide an in-depth understanding about the structural features of the FeNDCs and their impact on the catalytic activity and stability in alkaline and acidic media.
- ✧ To demonstrate the diversity of electrocatalytic potency of the FeNDCs in alkaline, acidic, and protic ionic liquids (PILs).
- ✧ To explore the novel protic ionic liquids beyond conventional tertiary amine based PILs, for instance primary amine based PILs.
- ✧ To demonstrate the effect of supramolecular forces, such as H-bonding over the physico-chemical properties of PILs with variation in the structure of protonic species.
- ✧ To exhibit the effect of protonic species (structure of cation) in the electrochemical behavior of PILs.
- ✧ To present a correlation between atomic scale features of the electrocatalyst based on PSs during oxygen reduction electrocatalysis in non-aqueous electrolyte, such as PILs.
- ✧ To find a suitable combination of electroactive materials based PILs/PSs for the realization of the fuel cells under non-humidified conditions.

### 1.10. Outlines of the current study

Protic ionic liquids/Salts (PILs/PSs) have been prepared with various cationic and anionic structure. For, electrocatalyst study, hydrogen sulfate anion  $[\text{HSO}_4^-]$  based PSs have been synthesized with various cationic structures as shown in Fig. 1.5. All these PSs were compatible with iron salt ( $\text{FeCl}_3$ ) and template. For the development of electrolyte, PILs were synthesized with various cationic and anionic structures. To discover the primary amine PILs, a rigorous approach was taken by employing primary alkylamines as shown in **Fig. 1.8**.

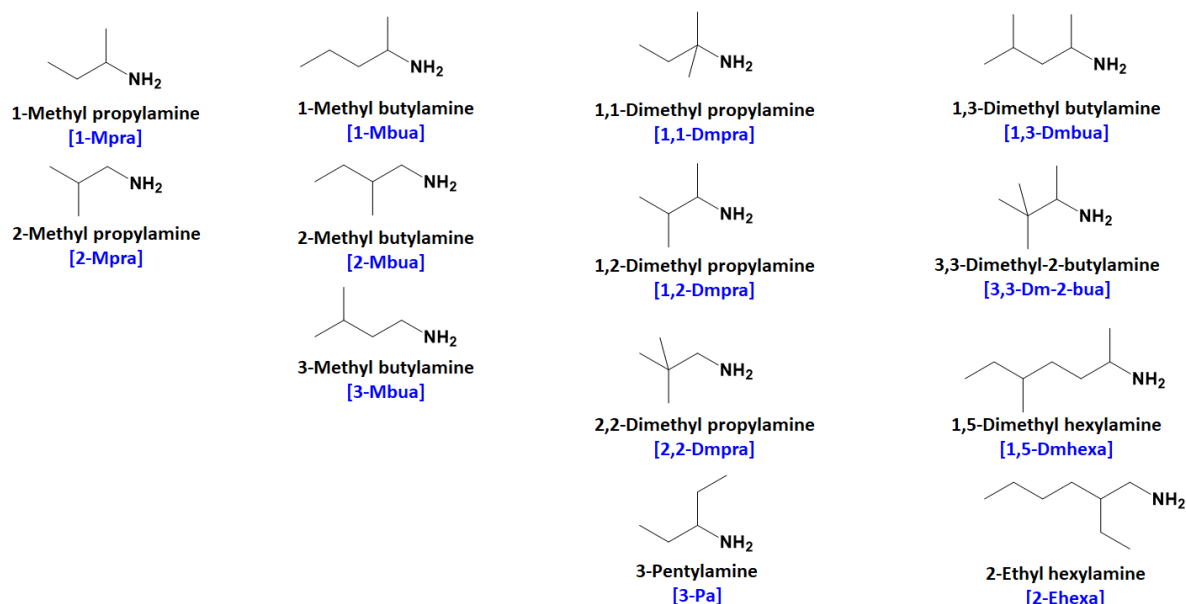


Fig. 1.8. Structure of primary alkylamines used in this study.

Firstly, Chapter 2 manifested of the viability and prospect of simple combination of PILs/PSs (e.g.  $[\text{Phen}][2\text{HSO}_4]$ ) and iron salt (e.g.  $\text{FeCl}_3$ ), to develop Fe, N, and S co-doped carbons (FeNDCs).

Chapter 2 was comprised of three main segments which are shown below:

- ✓ Synthesis of Fe, N, and S co-doped carbons (FeNDCs) via nanocasting of the mixture of  $[\text{Phen}][2\text{HSO}_4]$  and  $\text{FeCl}_3$ . During preparation, carbonization temperature was varied from 600 °C to 1000 °C, and the molar composition of the iron salt was changed from 3.5 mol% to 28 mol%.
- ✓ Characterization of Fe, N, and S co-doped carbons (FeNDCs) was performed via several spectroscopic techniques such as transmission electron microscopy (TEM), Mossbauer, x-ray photoelectron, Raman spectroscopy etc.
- ✓ Electrochemical performance of Fe, N, and S co-doped carbons (FeNDCs) in alkaline and acidic electrolyte was investigated via cyclic voltammetry, hydrodynamic voltammetry, and chronoamperometry.

Secondly, Chapter 3 displayed the prospect of Fe, N, and S co-doped carbons (FeNDCs) as electrocatalyst in protic ionic liquids (PILs) based on tertiary amine, that is  $[\text{Dema}][\text{TFO}]$ .

Then, Chapter 4 documented the discovery of primary amine based PILs and the correlation of their physico-chemical features against H-bonding. It also highlighted the fact of scarcity of primary amine-PILs in contrast with their secondary and tertiary amine analogues.

Finally, Chapter 5 showed the electrocatalytic activity of Fe, N, and S co-doped carbons (FeNDCs) with the variation in cationic part in PILs comprised of trifluoroacetate anion [TFA<sup>-</sup>] with the change in cationic structures of PILs from primary to tertiary alkylamines.

Chapter 5 was comprised of three segments which are shown below:

- ✓ Synthesis of Fe, N, and S co-doped carbons (FeNDCs) via nanocasting of the mixture of [X][2HSO<sub>4</sub>] and FeCl<sub>3</sub>, where X = [Phen], [oPDA], and [4,4-DmoBpy] and PILs, [Y][TFA], where X = [2-Mbua], [N-Eipra], and [Dema].
- ✓ Characterization of both FeNDCs and PILs via combination of spectroscopic, thermal, surface sensitive techniques.
- ✓ Evaluation of electrochemical behavior of Fe<sub>14</sub>NDC-Phen, Fe<sub>14</sub>NDC-oPDA, and Fe<sub>14</sub>NDC-4,4-DmoBpy in PILs ([2-Mbua][TFA], [N-Eipra][TFA], and [Dema][TFA]).

### 1.11. References

1. National Oceanic and Atmospheric Administration, U.S. Department of Commerce, The relentless rise of carbon dioxide, 2017. <https://climate.nasa.gov/vital-signs/carbon-dioxide/>
2. "Paris Agreement", United Nations Treaty Collection, 2016.
3. European Commission, EU Reference Scenario 2016 Energy, transport and GHG emissions Trends to 2050 Main results.
4. O. Groger, H. A. Gasteiger, and J.-P. Suchsland, *J. Electrochem. Soc.*, 2015, **162**, A2605-A2622.
5. S. M. Lyth, T. Ogura, J. Yamabe, A. Hayashi H.-W. Li, K. Sasaki, in *Hydrogen Energy Engineering: A Japanese Perspective*, Springer, 2016.
6. K. E. Swider-Lyons, and S. A. Campbell, *J. Phys. Chem. Lett.*, 2013, **4**, 393–401.
7. T. Yasuda and M. Watanabe, *MRS Bulletin*, 2013, **38**, 560-566.
8. D. A. McQuarrie, J. D. Simon, in *Molecular Thermodynamics*, University Science Books, Sausalito, CA, 1999.
9. J. Zhang, Z. Xia, L. Dai, *Sci. Adv.*, 2015, **1**, e1500564.
10. Z.-L. Wang, D. Xu, J.-J. Xu and X.-B. Zhang, *Chem. Soc. Rev.*, 2014, **43**, 7746—7786.
11. M. Watanabe, M. L. Thomas, S. Zhang, K. Ueno, T. Yasuda, and K. Dokko, *Chem. Rev.*, 2017, **117**, 7190–7239.
12. I. Katsounaros, S. Cherevko, A. R. Zeradjanin and K. J. J. Mayrhofer, *Angew. Chem. Int. Ed.*, 2014, **53**, 102 – 121.
13. D. Banham and S. Ye, *ACS Energy Lett.*, 2017, **2**, 629–638.
14. P. C. K. Vesborg, T. F. Jaramillo, *RSC Adv.*, 2012, **2**, 7933–7947.
15. A. J. Medford, A. V. J. S. Hummelshøj, J. Voss, F. Abild-Pedersen, F. Studt, T. Bligaard, A. Nilsson, J. K. Nørskov *J. Catal.*, 2015, **328**, 36–42.
16. P. Sirikulbodee, T. Ratana, T. Sornchamni, M. Phongakorn, S. Tungkamani, *Energy Procedia*, 2017, **138**, 998–1003.
17. F. Meshkani, M. Rezaei, *Int. J. Hydro. Energy*, 2014, **39**, 16318-16328.
18. P. Sabatier, A. Mailhe, *Comptes Rendus Paris*, 1911, **152**, 1212.
19. J. H. Zagal and M. T. M. Koper, *Angew. Chem. Int. Ed.*, 2016, **55**, 14510 – 14521.
20. M. Shao, Q. Chang, J.-P. Dodelet, and R. Chenitz, *Chem. Rev.*, 2016, **116**, 3594–3657.
21. N. Ramaswamy, U. Tylus, Q. Jia, and S. Mukerjee, *J. Am. Chem. Soc.*, 2013, **135**, 15443–15449.
22. H. R. Byon, J. Suntivich, and Y. Shao-Horn, *Chem. Mater.*, 2011, **23**, 3421–3428.
23. H. R. Byon, J. Suntivich, E. J. Crumlin and Y. Shao-Horn, *Phys. Chem. Chem. Phys.*, 2011, **13**, 21437–21445.
24. G. Wu, A. Santandreu, W. Kellogg, S. Gupta, O. Ogoke, H. Zhang, H.-L. Wang, L. Dai, *Nano Energy*, 2016, **29**, 83–110.
25. S. Zhang, K. Dokko and M. Watanabe, *Mater. Horiz.*, 2015, **2**, 168–197.

26. D. R. MacFarlane, A. L. Chong, M. Forsyth, M. Kar, R. Vijayaraghavan, A. Somers, and J. M. Pringle, *Faraday Discuss.*, 2018, **206**, 9–28.
27. Lin, Y.; Wang, X.; Qian, G.; Watkins, James J. Additive–Driven Self–Assembly of Well–Ordered Mesoporous Carbon/Iron Oxide Nanoparticle Composites for Supercapacitors. *Chem. Mater.* **2014**, *26*, 2128–2137.
28. S. Zhang, M. S. Miran, A. Ikoma, K. Dokko and M. Watanabe, *J. Am. Chem. Soc.*, 2014, **136**, 1690–1693.
29. N. R. Sahraie, J. P. Paraknowitsch, C. Göbel, A. Thomas and P. Strasser, *J. Am. Chem. Soc.*, 2014, **136**, 14486–14497.
30. S. Zhang, Z. Li, K. Ueno, R. Tataro, K. Dokko and M. Watanabe, *J. Mater. Chem. A*, 2015, **3**, 17849–17857.
31. S. Zhang, T. Mandai, K. Ueno, K. Dokko, M. Watanabe, *Nano Energy*, 2015, **13**, 376–386.
32. B.-B. Huang, Z.-Y. Luo, J.-J. Zhang, and Z.-L. Xie, *RSC Adv.*, 2017, **7**, 17941.
33. Grace Materials Technologies, USA. <https://grace.com/en-us/Pages/Ludox-Colloidal-Silica.aspx>.
34. D. Banham, F. Feng, T. Fürstenhaupt, K. Pei, S. Ye and V. Birss, *Catalysts*, 2015, **5**, 1046–1067.
35. R. G. Pearson, *J. Am. Chem. Soc.*, 1963, **85**, 3533–3539.

## CHAPTER 2 PROTIC SALTS DERIVED ELECTROCATALYST

### ***Iron, nitrogen, and sulfur doped mesoporous carbons for oxygen reduction reaction in alkaline and acidic media***

#### 2.1. Introduction

Overdependence on fossil fuels for automotive and on-site power sources appears to cause serious environmental changes.<sup>1</sup> Electrochemical energy storage and conversion devices, such as fuel cells, can offer alternative solutions to current energy sources.<sup>2</sup> Owing to its high efficiency and theoretical energy density, H<sub>2</sub>/air fuel cell technology is considered promising for replacing internal-combustion-engine-based automobiles.<sup>3</sup> The major bottleneck for widespread realization of fuel cells has been the usage of Pt/C or Pt-alloy/C at the cathode to minimize the overpotential for the oxygen reduction reaction (ORR) in aqueous electrolytes.<sup>3</sup> In the last few decades, extensive research has been devoted to finding efficient ORR electrocatalysts other than Pt, which is expensive and has limited natural resources. Most of these studies have focused on nonprecious metals, such as iron.<sup>1-3</sup> Since the early reports on synthetic macrocyclic iron complexes for oxygen reduction, such as porphyrins,<sup>4</sup> iron phthalocyanines<sup>5</sup> and then their corresponding annealed products<sup>6-7</sup>, recently active catalysts have been realized for ORR using mixtures of non-macrocyclic (i.e. simple) iron salts and high-surface-area carbons, such as acetylene black, super P, black pearl, and activated carbon.<sup>8-10</sup> Amongst the wide array of precursors and synthetic strategy for designing advanced iron-doped carbons,<sup>4,11</sup> there has been an upsurge of interest in natural or synthetic polymers as carbonaceous precursors. For instance, polyaniline,<sup>9,12</sup> poly(3,4-ethylenedioxythiophene),<sup>13</sup> polypyrrole,<sup>14</sup> polyacrylonitrile,<sup>15</sup> dicyandiamide,<sup>16</sup> etc. have been popular options due to the ease of polymerization over the microporous carbon support/mesoporous carbon spheres.

Apart from polymeric<sup>9-16</sup> and macrocyclic complexes,<sup>17</sup> 1,10-phenanthroline (Phen) as a sole precursor for iron doped carbons came into contention after the report from Lefevre *et. al.*<sup>18</sup> Using time-of-flight secondary ion mass spectrometry, a catalytic active site formed at high temperature was identified at the edge of the graphene layer of the carbon support with two-adjacent nitrogen atoms complexing the Fe ion (phenanthroline type, Fe-N<sub>2</sub>-C<sub>4</sub><sup>+</sup>).<sup>18</sup> However, carbons from the Fe-Phen complex has shown poor results owing to the low retention of the active site after high temperature pyrolysis.<sup>19</sup> Also, the carbon yield was relatively low at higher temperature (> 600 °C) due to the poor thermal stability of the complex (Fe-Phen) and evaporation of the excess Phen.<sup>19-21</sup> Thus, through using a high surface area carbon support, i.e., carbon black and carbonizing in gaseous NH<sub>3</sub>, activity of Fe-Phen complex derived carbons was improved,<sup>20</sup> yet still lagging compared to that of macrocyclic counterparts.<sup>20,22</sup> Then, ORR activity of such carbons was further enhanced by using metal-organic frameworks (MOFs), particularly ZIF.<sup>8,10,23,24</sup> Despite that, stability of Fe doped carbons prepared in gaseous NH<sub>3</sub> has not been satisfactory.<sup>9,25</sup> Annealing under Ar is one of the methods to improve the stability, but this often compromises the activity.<sup>26,27</sup> Overall, fabrication of an efficient ORR electrocatalyst from a molecular precursor like Phen via an inexpensive and flexible route without a laborious preparation process, additives and post treatments<sup>28</sup> is still lacking. Recently, we have demonstrated that a subclass of ionic liquids,<sup>29</sup> protic ionic liquids/protic salts (PILs/PSs) could be considered as versatile carbon precursors for

nitrogen doped carbons.<sup>29,30</sup> There are certain advantages of a PIL/PS being the precursor for carbons compared to thermally unstable molecules,<sup>31-34</sup> polymers,<sup>35-37</sup> MOFs,<sup>38-40</sup> and especially other variants of ionic liquids<sup>41-43</sup> for the following reasons:

(i) **Simple & quick:** *In-situ* doped carbons are synthesized via only two simple steps: neutralization (Brønsted acid-Brønsted base reaction) and subsequent direct carbonization at ambient pressure.<sup>44</sup>

(ii) **High carbon yield:** Protonation of the base (Phen) by the acid ( $\text{H}_2\text{SO}_4$ ) improves the thermal stability of the corresponding base.<sup>44</sup>

(iii) **Robust & cost-effective:** Intrinsic structural diversity (cation and anion) of PILs/PSs is pivotal for controlling the physico-chemical properties such as surface area, nitrogen content, graphitic degree, etc. of the carbons.<sup>45</sup> Moreover, a PIL/PS does not require any additional chemicals such as oxidants, additives etc. and avoids complicated multistep reactions.<sup>45</sup>

In this study, we prepared a PS from Phen and sulfuric acid, that is, 1,10-phenanthroline dihydrogen sulfate ([Phen][2HSO<sub>4</sub>]).

[Phen][2HSO<sub>4</sub>]-derived nitrogen doped carbons have high relative carbon yield and high nitrogen content but with low surface area ( $S_{\text{BET}} = 6 \text{ m}^2 \text{ g}^{-1}$ ).<sup>45</sup> Importantly, carbon yield from the [Phen][2HSO<sub>4</sub>] was much higher than Phen under the same pyrolyzing condition.<sup>46</sup> Colloidal silica, LUDOX HS-40 (12 nm diameter),<sup>47</sup> was introduced as a hard template in combination with PS and iron(III) chloride ( $\text{FeCl}_3$ ) (Fig. 2.1) to impart hierarchical porous structure in the catalyst architecture. With this

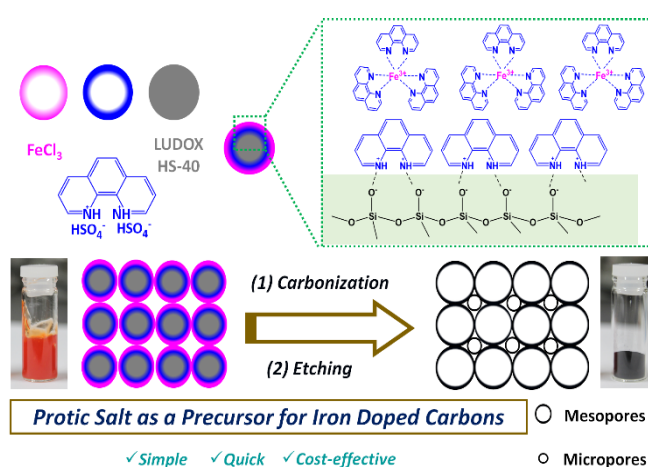


Fig. 2.1. Schematic illustration of nanocasting synthesis of iron-doped porous carbons by direct carbonization of a mixture of a protic salt, a simple iron salt, and colloidal silica, LUDOX HS-40.

strategy, the function of PS is two-fold. Firstly, compatibility of the PS with the template due to the possible electrostatic interaction<sup>48</sup> between the cationic moiety [Phen] of the PS and the negative surface of silica. Secondly, miscibility of the PS with the iron salt ( $\text{FeCl}_3$ ) due to the strong interaction<sup>49</sup> of the iron (III) ion with the free 1,10-phenanthroline present in the PS. This neutral base is present in non-negligible quantities in the protic salt stemming from the low value of  $\Delta\text{p}K_{\text{a}}$  (7.86), as the extent of proton transfer is governed by the difference between the  $\text{p}K_{\text{a}}$  values of the acid and base in a PIL/PS.<sup>50</sup> Due to the interplay between coordination and acid-base chemistry, this design principle is not only applicable to other transition metals such as nickel and cobalt etc.<sup>51</sup> but also to other PSs like ortho phenylenediamine-based [oPDA][2HSO<sub>4</sub>] and ortho bipyridine-derived [oBPY][2HSO<sub>4</sub>], etc. as well.<sup>52,53</sup> During carbonization [Phen][2HSO<sub>4</sub>] undergoes an oxidative cross-coupling polymerization in which the anion acts as an oxidant.<sup>44</sup> At high temperature, this polymerized framework condenses into a 2D nitrogen-, sulphur-doped carbon structure by releasing gaseous molecules such as  $\text{SO}_2$  and  $\text{H}_2\text{O}$ ,<sup>54</sup> in accordance with the annealing mechanism already proposed for PS<sup>54</sup> and AILs<sup>44</sup> derived carbon materials. The *in-situ* formed Fe-Phen also decomposes and integrates in the carbon

lattice at high temperature.<sup>19-20</sup> Excess FeCl<sub>3</sub> can also generate a mixture of iron oxide/carbide as well as iron nanoparticles.<sup>34,41</sup> Thus, we can obtain support-free iron, nitrogen, and sulfur co-doped carbon materials. Herein, we report for the first time, fabrication of highly efficient iron-doped porous carbons was achieved utilizing the 1,10-phenanthroline-based PS and an iron precursor via *nanocasting* without any supporting materials. Here, a prototype catalyst, Fe<sub>14</sub>NDC-9, will be presented as a model example to gain insight of the structural features. Then, the catalytic activity of Fe<sub>14</sub>NDC-9 will be elaborated in detail. A correlation plot for various iron doped carbons prepared in this study will be discussed to have deeper understanding about the active site responsible for catalytic activity. The post treated sample of Fe<sub>14</sub>NDC-9 termed as Fe<sub>14</sub>NDC-9-W<sub>2M</sub>-9 will also be evaluated for catalytic performance in acidic electrolyte and compared with alkaline media. In addition to activity, stability of the samples will also be investigated to probe the possibility of their application in fuel cells.

## 2.2. Experimental Details

### 2.2.1. Synthesis of protic salts

The PS, [Phen][2HSO<sub>4</sub>], was synthesized via a simple Brønsted acid-base neutralization reaction of 1,10-phenanthroline monohydrate (Wako, >99%) and sulfuric acid (Wako, 96-98%) (Fig. 1). Ethanol (Wako, 99.9%) was used as a diluting reaction solvent to limit the temperature increase during the exothermic reaction, and then removed by rotary evaporation at 40 °C. The product was then dried under vacuum for 48 h at 80 °C.<sup>29</sup>

### 2.2.2. Synthesis of carbon materials

The synthesized PS, [Phen][2HSO<sub>4</sub>], was mixed with the appropriate amount of anhydrous FeCl<sub>3</sub> (Junsei, 97%) for the desired loading of Fe, by keeping the total mass constant at 2.0 g. Subsequently, 5.0 g of colloidal silica particles, LUDOX HS-40 (Sigma-Aldrich, 40 wt.% suspension in H<sub>2</sub>O) was added. The dried precursor mixture was then transferred into a quartz boat for direct carbonization in a tube furnace under an Ar atmosphere (100 mL min<sup>-1</sup>) using the following temperature program: (1) degassing at room temperature for 1 h; (2) heating to 250 °C at a rate of 4 °C min<sup>-1</sup>; (3) holding the temperature at 250 °C for 2 h; (4) heating to the desired temperature (e.g., 900 °C) at a rate of 10 °C min<sup>-1</sup>; and finally, (5) maintaining the sample at this temperature for 2 h. After cooling the sample to room temperature, template was removed, washed and dried per to the previous report.<sup>46</sup> To apply the catalyst in acidic electrolyte, secondary acid washing was done by 2 M HCl (Wako, analytical grade) at 80 °C for 8 h and then washed out with deionized water until pH reached neutral and then dried at 100 °C for 8 h. Then, second carbonization was performed to remove volatile species and to stabilize the carbon using the following carbonization scheme: (1) degassing at room temperature for 1 h; (2) heating to the desired temperature (e.g., 900 °C) at a rate of 10 °C min<sup>-1</sup>; (3) maintaining the sample at this temperature for 2 h.

### 2.2.3. Materials characterization

High-resolution transmission electron microscopy (HR-TEM) was performed using a JEOL JEM-2100F field emission source transmission electron microscope operating at 20.0 kV. Field emission scanning electron microscopy (FE-SEM, Hitachi-SU8010) was operated at an accelerating voltage of 5.0 kV.

Elemental analysis performed using a Bruker Quantax EDS for SEM with an XFlash 5060 detector elemental analyser.

The  $^{57}\text{Fe}$  Mössbauer spectrum of  $\text{Fe}_{14}\text{NDC-9}$  was measured using a conventional Mössbauer spectrometer (Wissel) with a cryostat containing a Nb-Ti superconducting magnet (Torisha Co.). The Mössbauer source was a  $^{57}\text{Co}$  in Rh matrix (925 MBq, Ritverc), and Mössbauer  $\gamma$ -rays were detected by a proportional counter. Velocity calibration of the system was done by measuring the Mössbauer absorption lines of  $^{57}\text{Fe}$  in an iron foil. The Mössbauer spectral absorbers contained ca. 88 mg/cm<sup>2</sup> of  $\text{Fe}_{14}\text{NDC-9}$ . The spectrum was first scanned in a wider range ( $\pm 10$  mm s<sup>-1</sup>) to screen the magnetic particles in the FeNDCs. Then, the spectrum was recorded from -4 mm s<sup>-1</sup> to +4 mm s<sup>-1</sup> at 17 K. The Mössbauer spectrum was analysed by a least-squares fit using Lorentzian shape by fixing quadrupole splitting parameter and full-width half maxima (FWHM) per literature reports.<sup>61</sup>

Iron content was determined by the Shimadzu ICPE-9000 inductively coupled plasma atom emission spectroscope (ICP-AES) using standard solutions of iron nitrate as reference (Wako). Oxidation stability of the carbon was determined by thermogravimetry/differential thermal analyzer (TG-DTA 7200, Seiko Instruments) from room temperature to 800 °C at a heating rate of 10 °C min<sup>-1</sup> under O<sub>2</sub> flow of 100 mL min<sup>-1</sup> with open alumina pans.

X-ray photoelectron spectroscopy (XPS, PHI Quantera SXM) was done at a base pressure of  $6.7 \times 10^{-8}$  Pa with an Al K $\alpha$  (1486.6 eV) X-ray source and a pass energy of 280.00 eV (survey scan) or 69.00 eV (high-resolution scan). The C 1s line at 284.6 eV was utilized as a reference for the binding energies in the acquired spectra. Based on the Shirley-type background, all the high-resolution XPS spectra were deconvoluted via the peak components represented by an 80% Gaussian-20% Lorentzian function.

Powder X-ray diffraction (XRD) patterns were collected using a Rigaku RINT-2000 diffractometer with Cu K $\alpha$  ( $\lambda = 0.154$  nm) radiation. The diffraction patterns were recorded in a  $2\theta$  range of 10°-90° with a  $2\theta$  step size of 0.02° and a scanning speed of 10° min<sup>-1</sup>.

Raman spectra were recorded using a Raman spectrometer (RMP-300, JASCO, Japan) with a 532 nm laser excitation source at room temperature. Deconvolution of raw Raman spectra was performed by using Peak Fit software (v4.12) based on standard conventions after linear baseline correction.<sup>55-56</sup> The values of the correlation factor ( $R^2$ ) were greater than 0.998 for all spectral fits.

Nitrogen sorption isotherms were recorded on a BELSORP-mini II sorption analyser (BEL Japan, Inc.) at -96 °C (77 K). Prior to each measurement, the sample was pre-treated at 300 °C for 3 h under N<sub>2</sub> (g). The SSA was calculated using the Brunauer-Emmett-Teller (BET) method. The total pore volume ( $V_{\text{total}}$ ) was determined from the N<sub>2</sub> (g) uptake at a relative pressure,  $p/p_0$ , of 0.99. The distribution of mesopores was determined by using the Barrett-Joyner-Halenda (BJH) method based on the Kelvin equation.<sup>59</sup> The two-dimensional nonlocal density functional method (2D-NLDFT) was used to calculate the distribution of micropores using the SAIEUS program (Micromeritics) developed by Jagiello *et al.* for microporous carbons.<sup>60</sup>

#### 2.2.4. Electrochemical characterization

All electrochemical experiments were carried out in a temperature-controlled (inverter cooling bath, OMRON, Japan) three-electrode electrochemical cell as shown in **Fig. 2.3** at 25 °C using a CHI701E electrochemical workstation (CH Instruments, USA). In alkaline media, a Ag/AgCl electrode (ALS, Japan, RE-1B, 3.0 M NaCl) was served as the reference electrode. For acidic electrolyte, RHE (RHEK Reversible hydrogen electrode kit, ALS, Japan, catalogue no # 013597) was constructed before each electrochemical measurement. To

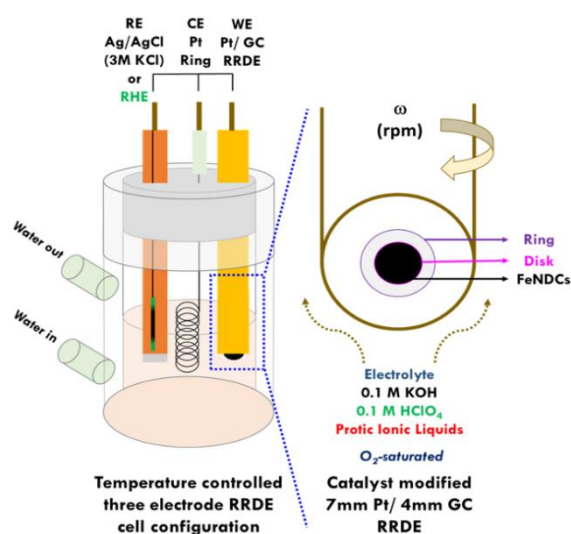


Fig. 2.2. Electrochemical cell design.

prepare RHE, in the electrochemical cell (water-jacketed glass cell, ALS, japan, catalogue no # 012652) containing the 0.1 M HClO<sub>4</sub>, RHE was set as the working electrode and a Pt coil (ALS, Japan, 0.5 mm diameter) as the counter electrode. Then, chronoamperometric *i-t* was performed until the charge reached two coulombs to generate hydrogen gas *in-situ* via the electrolysis of the acid solution. In both electrolytes, Pt coil (ALS, Japan, 0.5 mm diameter) were used as the counter electrode. As the working electrode, a Pt ring/GC disk rotating ring-disk electrode (RRDE; ALS, Japan) with 5.0/7.0 mm inner/outer ring diameters and a 4.0 mm disk diameter was employed to evaluate the catalytic activity and stability of materials investigated in this work. To compare results in alkaline and acidic media, the electrode potentials vs. the Ag/AgCl electrode in alkaline solutions (0.1 M KOH) were converted to the potential vs. RHE at pH = 13 using **Eq. 2.1**.

$$E_{\text{vs RHE}} = E_{\text{vs Ag/AgCl}} + 0.209 + 0.059 \text{ pH} \quad (\text{Eq. 2.1})$$

**Electrode Preparation.** Briefly, for iron doped carbons, catalyst ink (9.42 mg mL<sup>-1</sup>) was prepared by adding 9.42 mg of catalyst to a 1.0 mL mixture of deionized water (0.75 mL), ethanol (0.20 mL), and Nafion as an ionomer (0.05 mL, 5.0 wt%; Sigma-Aldrich, Nafion 117). Then, the mixture was ultrasonicated enough to make a well-dispersed ink, and finally dropped (8.0 μL) into a mirror polished GC surface of Pt/GC electrode by using a microsyringe (ITO corporation, Japan). For commercial Pt/C (20 wt%), concentration of the catalyst ink was 4.0 mg mL<sup>-1</sup>, of which 8.0 μL was casted onto the electrode. Before casting the catalyst ink, the GC electrode surface was purged with Ar to remove any surface moisture.

**Electrocatalytic activity and stability test.** All cyclic voltammetry (CV) and linear sweep voltammetry (LSV) measurements were carried out at scan rates of 100 and 10 mV s<sup>-1</sup>, respectively. Before each measurement, the electrodes were first conditioned in N<sub>2</sub>-saturated 0.1 M KOH (Wako, analytical research grade) by cycling the potential from

+0.25 V to -0.95 V at a scan rate of 100 mV s<sup>-1</sup> for 50 cycles. For RRDE voltammograms for 0.1 M KOH, the ring potential of the RRDE was held constant at +0.5 V against the Ag/AgCl reference electrode and at +1.2 V for 0.1 M HClO<sub>4</sub>. After scanning the potential three times without any rotation (0 rpm), the RRDE voltammogram was acquired at 1600 rpm. For kinetic analysis, the rotation speed was varied from 600 to 2500 rpm. The displayed current density and potential in LSVs for all the samples were background and *i*R corrected. In all cases, to evaluate the catalytic activity, the onset potential was determined from the LSV curves at 0.1 mA cm<sup>-2</sup>.

To construct Tafel plots, the kinetic current (*J<sub>k</sub>*) was calculated from the mass-transport correction of the RDE voltammograms using the following equation:

$$J_k = \frac{J_D J}{J_D - J} \quad (\text{Eq. 2.2})$$

where *J<sub>k</sub>* is the kinetic current density, *J* is the measured current density, and *J<sub>D</sub>* is the diffusion-limiting current density.

Detailed analysis of the kinetics of the ORR was carried out using the Koutecky-Levich (K-L) equations (**Eqs. (2.3) -(2.5)**).

$$\frac{1}{J} = \frac{1}{B\omega^{1/2}} + \frac{1}{J_k} \quad (\text{Eq. 2.3})$$

where *J* is the measured current density, *J<sub>k</sub>* is the kinetic current density,  $\omega$  is the angular velocity of the disk ( $\omega = 2\pi N$ , *N* is the linear rotation speed), and *B* is the Levich slope, which is given by:

$$B = 0.201nFC_0D_0^{2/3}\nu^{-1/6} \quad (\text{Eq. 2.4})$$

where *n* is the overall number of electrons transferred during oxygen reduction, *F* is the Faraday constant (*F* = 96485 C mol<sup>-1</sup>), *C<sub>0</sub>* is the bulk concentration of O<sub>2</sub> (*C<sub>0</sub>* = 1.2 × 10<sup>-6</sup> mol cm<sup>-3</sup> for both alkaline and acidic media), *D<sub>0</sub>* is the diffusion coefficient of O<sub>2</sub> (*D<sub>0</sub>* = 1.9 × 10<sup>-5</sup> cm<sup>2</sup> s<sup>-1</sup> for 0.1 M KOH and *D<sub>0</sub>* = 1.93 × 10<sup>-5</sup> cm<sup>2</sup> s<sup>-1</sup> for 0.1 M HClO<sub>4</sub>), and  $\nu$  is the kinematic viscosity of ( $\nu = 0.01$  cm<sup>2</sup> s<sup>-1</sup> for both electrolytes).<sup>84</sup>

$$\frac{1}{J_k} = \frac{1}{nFkC_0} \quad (\text{Eq.2.5})$$

**Eq. (2.5)** is the intercept of **Eq. (2.3)** and *k* is the electron transfer rate constant. Per Eqs. (3) and (2), *n* and *J<sub>k</sub>* could be estimated from the slope and the intercept of the K-L plot, respectively. From Eq. (4), using the obtained values of *n* and *J<sub>k</sub>*, the heterogeneous rate constant for electron transfer (*k*) could be calculated.

The mass activity, *J<sub>m</sub>* (A g<sup>-1</sup>) of the catalyst in 0.1 M KOH was calculated using the following equation:

$$J_m = \frac{J_k(0.8 \text{ V vs RHE})}{L_{\text{cat}}} \quad (\text{Eq. 2.6})$$

where  $J_k$  ( $\text{mA cm}^{-2}$ ) is the kinetic current density at 0.8 V vs reversible hydrogen electrode (RHE) calculated by the **Eq. (2.5)** and  $L_{\text{cat.}}$  ( $\mu\text{g cm}^{-2}$ ) is the amount of catalyst loaded on the GC surface of the RRDE.

$$J_k = \frac{J_k(0.8 \text{ V vs RHE}) * J_{\text{Lim}}}{J_{\text{Lim}} - J_k(0.8 \text{ V vs RHE})} \quad (\text{Eq. 2.7})$$

where  $J_{\text{Lim}}$  ( $\text{mA cm}^{-2}$ ) is diffusion-limited current density in the  $\text{O}_2$ -saturated electrolyte after background correction.

In 0.1 M  $\text{HClO}_4$ , same **Eqs. (2.6) -(2.7)** were used for mass activity calculation at 0.7 V vs RHE.

Chronoamperometry (i-t) experiments were conducted in an  $\text{O}_2$ -saturated environment at 1600 rpm. The current density was monitored for  $10^4$  s at the peak potential of the electrocatalyst in both electrolytes. Cyclic stability tests were conducted using CV by cycling the potential from +0.25 V to -0.95 V at a scan rate of  $100 \text{ mV s}^{-1}$  for 2000 cycles in 0.1 M KOH. To compare the inherent kinetic activity of the catalysts, LSV measurements were obtained before and after the chronoamperometry and cyclic stability measurements under the same experimental conditions.

## 2.3. Results and Discussion

### 2.3.1. Structural insight of protic salt derived iron-doped porous carbons

A series of carbon materials were prepared by carbonization of the mixture of PS,  $\text{FeCl}_3$  and LUDOX-HS40, as described in the Introduction. Sample abbreviations (**Table 2.1**) were given the general form  $\text{Fe}_w\text{NDC-T}$ , where  $w$  is the wt% of iron (in  $\text{Fe}^{3+}$  form) in the precursor and  $T$  °C is the temperature of carbonization. Additional suffixes are also used, with -NT referring to a sample prepared without silica template, - $W_{2M}$ -9 referring to a wash with 2M HCl after the carbonization and a second carbonization at 900 °C. A summary of the precursor compositions and preparation conditions is shown in **Table 2.1**, and described in detail in the Experimental section. In this part, iron doped carbons and nitrogen doped carbons are termed as FeNDCs and NDCs respectively.

Sample abbreviation	Preparation conditions						
	FeCl <sub>3</sub> in precursor (mol%)	Fe content in precursor (wt%)	Template	Temperature of 1 <sup>st</sup> carbonization (°C)	Acid wash	Temperature of 2 <sup>nd</sup> carbonization (°C)	Fe content in product* (wt%)
<b>NDC-9</b>	None	None	LUDOX HS-40	900	None	None	None
<b>Fe<sub>14</sub>NDC-9</b>	20	14	LUDOX HS-40	900			3.5
<b>Fe<sub>14</sub>NDC-9-NT</b>	20	14	None	900			7.92
<b>Fe<sub>14</sub>NDC-9-W<sub>2M</sub>-9</b>	20	14	LUDOX HS-40	900	2M HCl	900	1.67
<b>Fe<sub>14</sub>NDC-9-9</b>	20	14	LUDOX HS-40	900	None	900	Not determined
<b>Fe<sub>14</sub>NDC-6</b>	20	14	LUDOX HS-40	600		8.8	
<b>Fe<sub>14</sub>NDC-8</b>	20	14	LUDOX HS-40	800		7.4	
<b>Fe<sub>14</sub>NDC-10</b>	20	14	LUDOX HS-40	1000		0.8	
<b>Fe<sub>3.5</sub>NDC-9</b>	5	3.5	LUDOX HS-40	900		1.95	
<b>Fe<sub>7</sub>NDC-9</b>	10	7	LUDOX HS-40	900		2.42	
<b>Fe<sub>28</sub>NDC-9</b>	40	28	LUDOX HS-40	900		Not determined	

\*mass % of iron salt determined by ICP-AES in final product after carbonization etc.

Table 2.1. Details of the preparation conditions for carbons.

The porous architecture of Fe<sub>14</sub>NDC-9 was initially probed by HRTEM, revealing large, disordered, and spherical mesopores (Fig. 2.3a and c) as was previously observed for a Pt/C material prepared with the same silica template,<sup>47</sup> whereas, for Fe<sub>14</sub>NDC-9-NT (Fig. 2.3b), this porous network was absent, with large aggregated nanocrystals and amorphous particles being observed. For the porous Fe<sub>14</sub>NDC-9, bent graphene layers were found at the edge of the carbon, as indicated by arrows in Fig. 2.3c. Such distorted graphene layers suggest the presence of a perturbed graphitic structure in Fe<sub>14</sub>NDC-9.

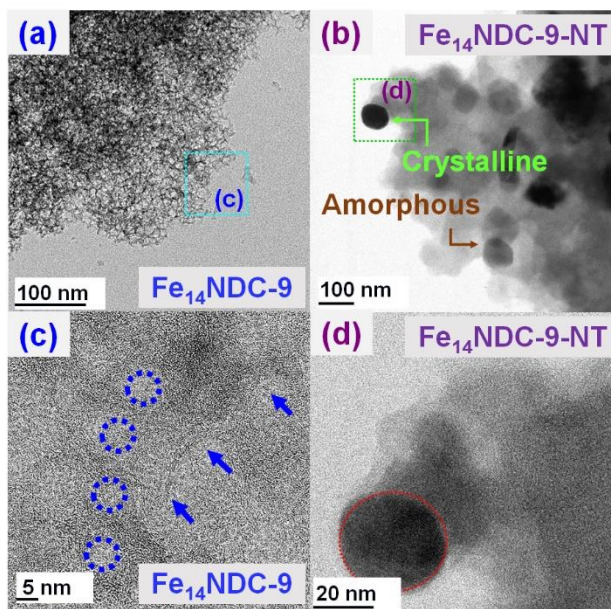


Fig. 2.3. HRTEM micrographs of (a, c) Fe<sub>14</sub>NDC-9, and (b, d) Fe<sub>14</sub>NDC-9-NT. Circles indicate mesopores and arrows indicate bent graphitic layers at the edge of the carbon.

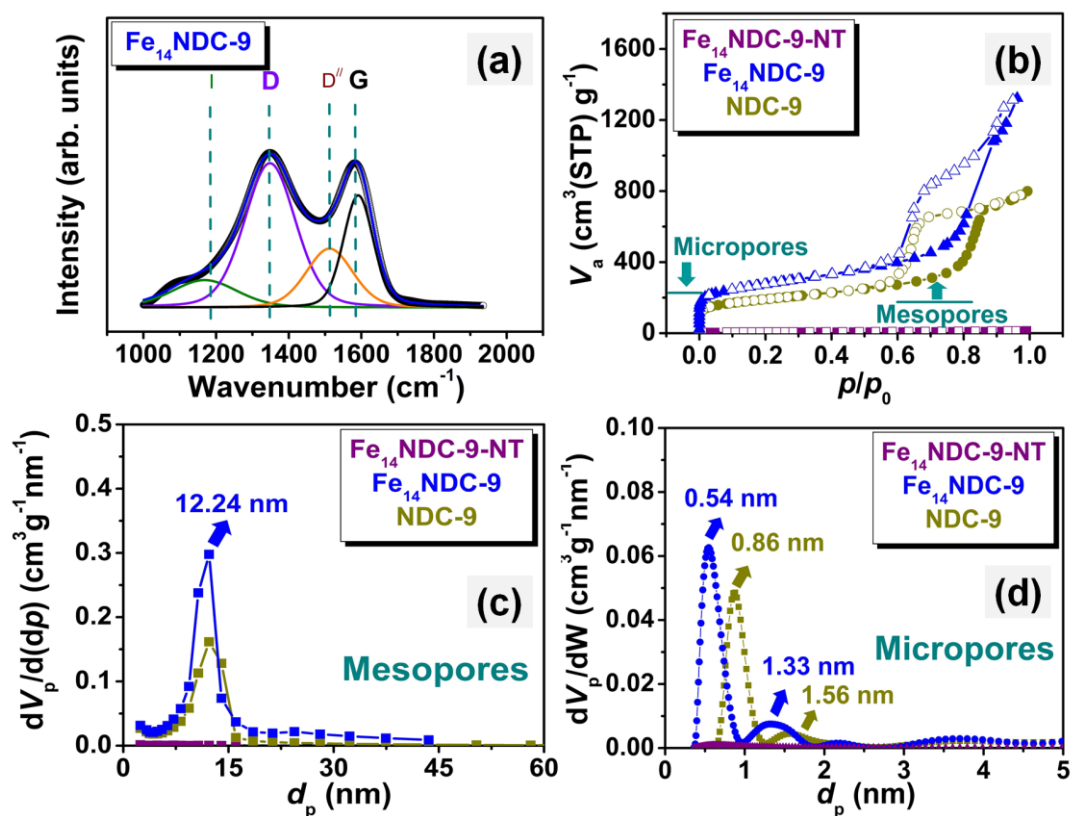


Fig. 2.4. (a) Raman spectra (b) Adsorption-desorption isotherms, (c) BJH plots, and (d) 2D-NLDFT plots.

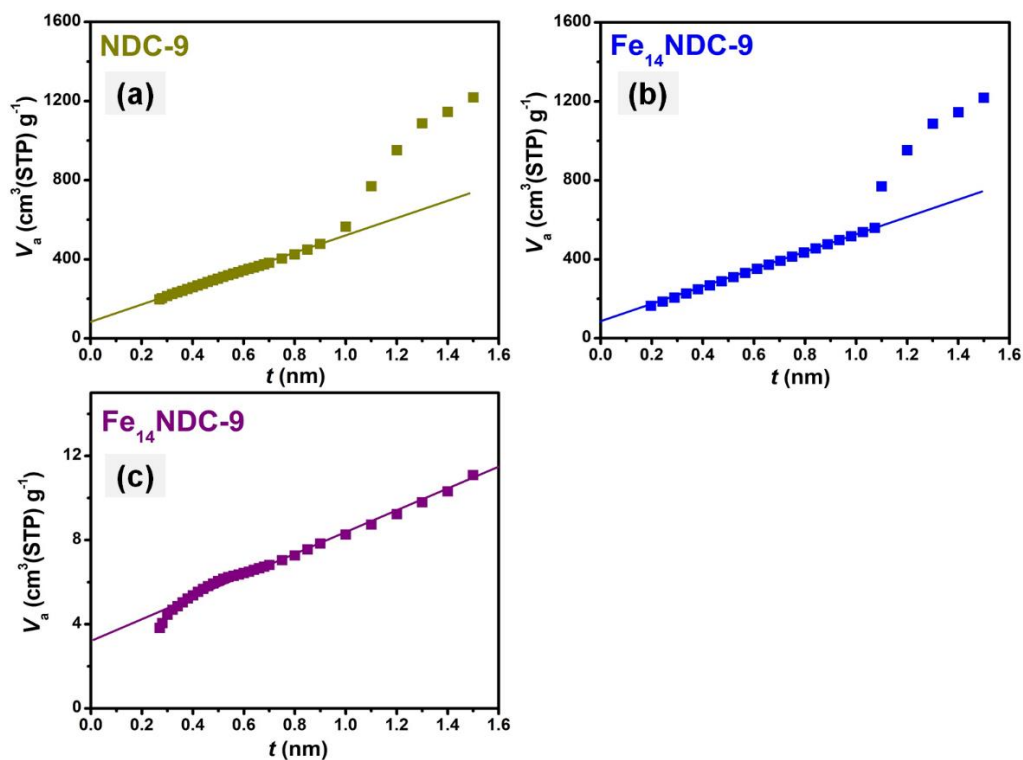
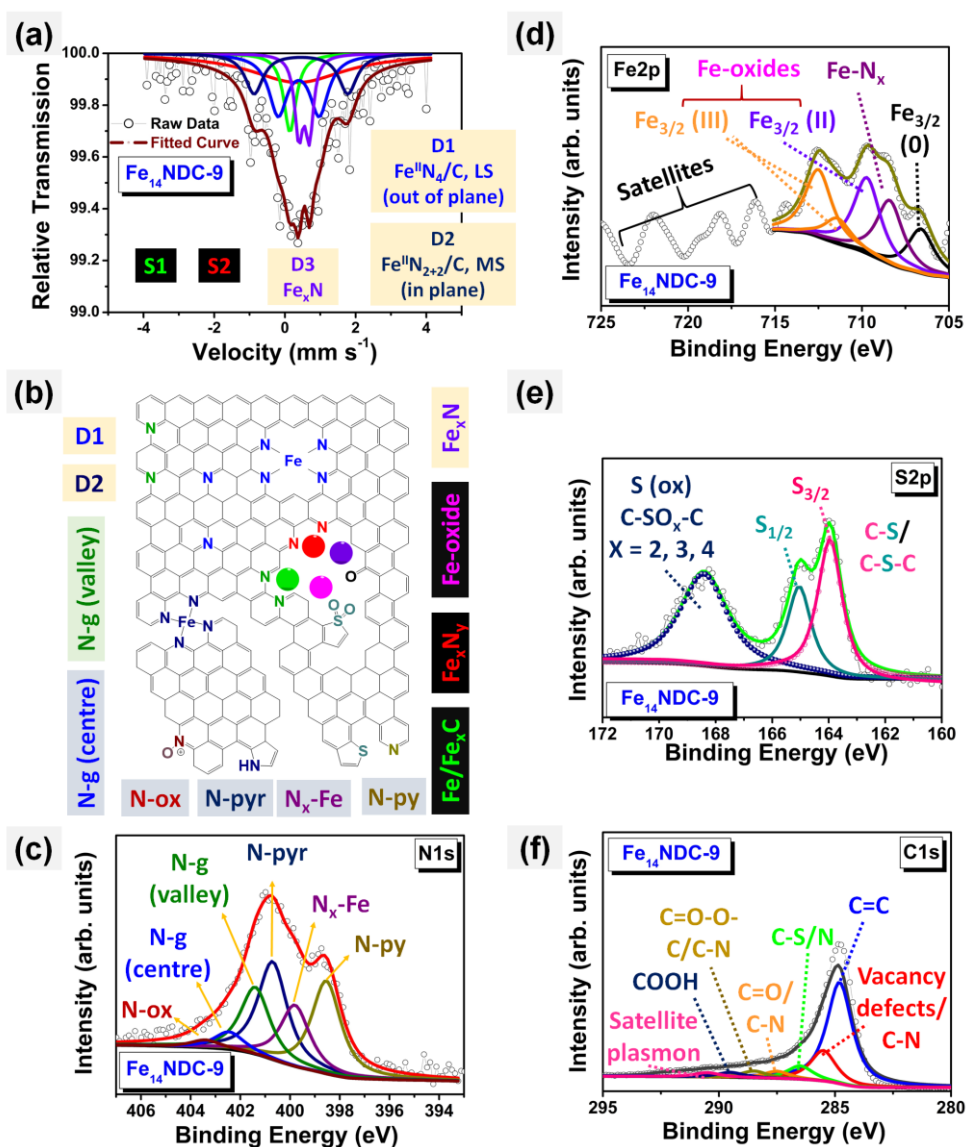
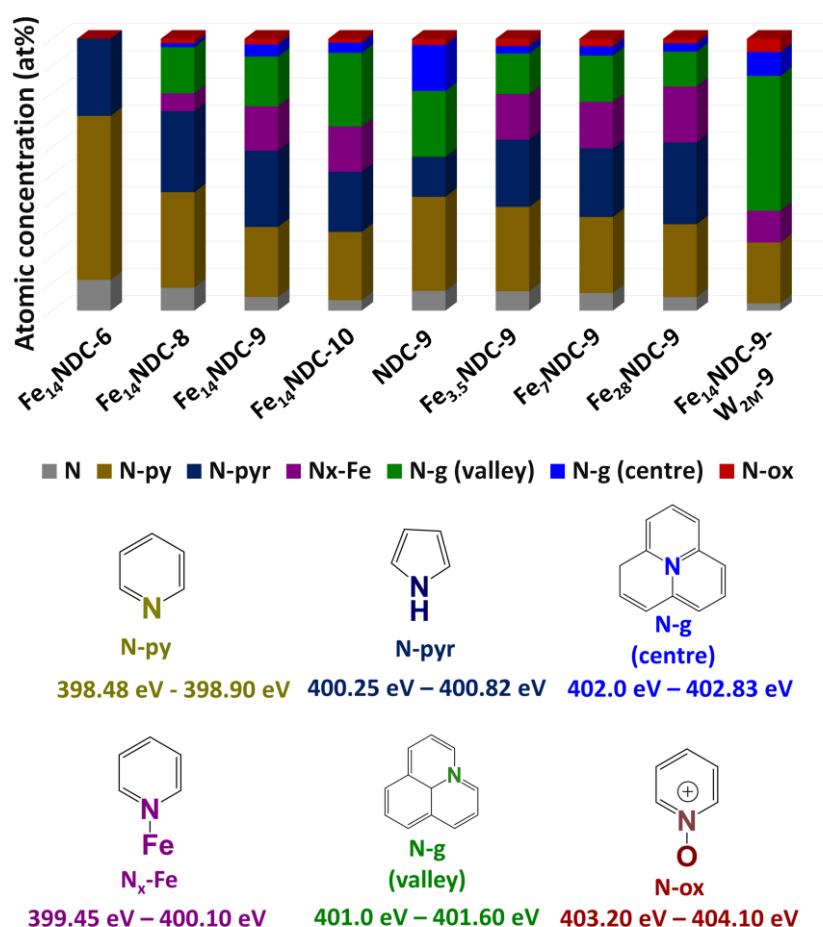


Fig. 2.5.  $t$ -plots for doped carbons showing presence of micropores.

Upon deconvoluting the Raman spectra, four bands were located for Fe<sub>14</sub>NDC-9 (**Fig. 2.4a**) at approximately 1200, 1350, 1530, and 1597 cm<sup>-1</sup>, denoted as I (impurity), D (in-plane defects), D// (interstitial defects), and G (graphitic structure), respectively, as per convention.<sup>55-58</sup> This Raman spectrum is similar to those observed for NDC-9 and Fe<sub>14</sub>NDC-9-NT (**Fig. A 2.1a, b**) indicating that both iron doping and template incorporation in Fe<sub>14</sub>NDC-9 did not compromise the formation of a partial graphitic structure with quasi-ordered doping of carbon.<sup>57</sup> The XRD pattern for Fe<sub>14</sub>NDC-9 (**Fig. A 2.1c**) further supports the Raman result. In depth physisorption analysis demonstrated that the Fe<sub>14</sub>NDC-9 possessed a high specific surface area (SSA) of 959 m<sup>2</sup> g<sup>-1</sup> with narrow pore size distribution between 6-17 nm (**Fig. 2.4b-c**). t-plots analysis as shown in **Fig. 2.5**, exhibited upward deviation from linearity at large film thicknesses with a small positive intercept indicating presence of micropores at smaller fraction. Furthermore, micropore analysis<sup>60</sup> based on NLDFT revealed micropores centred at 0.54 nm and 1.33 nm for Fe<sub>14</sub>NDC-9, as shown in **Fig. 2.4d**. These micropores were smaller than those of NDC-9 inferring the additional development of smaller micropores in Fe<sub>14</sub>NDC-9 by iron doping (**Fig. 2.4d**).



**Fig. 2.6.** (a) Mössbauer spectrum, (b) Schematic representation of various bonding configurations of heteroatoms (Fe, N, S and O) in Fe<sub>14</sub>NDC-9. High resolution (c) N1s, (d) Fe2p, (e) S2p, and (f) C1s XPS spectra.



**Fig. 2.7.** Atomic concentration for nitrogen (Table S3) and its different configurations with the binding energy range for each site obtained from the deconvoluted N1s HR-XPS spectra (Fig. A 2.2, and Table A 2.3).

Furthermore, to detect the presence of pyridinic nitrogen (N-py) that is in co-ordination with Fe, X-ray photoelectron spectroscopy (XPS) was utilized. However, nitrogen can also adopt several other bonding configurations depending on its position in the carbon plane. The high resolution XPS N1s spectrum of Fe<sub>14</sub>NDC-9 exhibited six peaks after deconvolution, as shown in Fig. 2.6c and depicted in Fig. 2.6b. Peaks corresponding to N-py, iron coordinated with nitrogen (N<sub>x</sub>-Fe),<sup>62,65-67</sup> pyrrolic nitrogen (N-pyr),<sup>62,65-68</sup> graphitic nitrogen at the valley (N-g (valley)),<sup>69-71</sup> graphitic nitrogen at the centre (N-g (centre)),<sup>69-72</sup> and oxidized forms of nitrogen (N-ox)<sup>73</sup> were positioned at 398.54 eV, 399.80 eV, 400.7 eV, 401.4 eV, 402.5 eV, and 403.4 eV respectively (Fig. 2.6c, Table A 2.2, Fig. 2.7). Iron interacts with the N-py directly due to its high reactivity in contrast to N-g demonstrated by many reports.<sup>65-68,74-78</sup> Also, Fe<sup>3+</sup> ion interacts with the oxidized functional group in graphene resulting in aggregation and increase of the oxide content as observed in heat treated graphene oxide and iron.<sup>78</sup> Furthermore, reduction of Fe<sup>3+</sup> into Fe can catalyse the graphitization of carbon.<sup>55,79-81</sup>

Due to these metal/metal ion-carbon interactions, the binding energies of peaks for FeNDCs in N1s HR-XPS spectra usually shift into the higher energy in contrast with NDCs (no iron), as observed in recent studies of FeNDCs.<sup>63-68,74-78</sup> The binding energy range of the deconvoluted peaks and atomic concentration for all the samples studied here are shown in **Fig. 2.7**, **Fig. 2.8**, **Table A 2.2**, and **Table A 2.3**.

To shed more light on the presence of the N<sub>x</sub>-Fe centre for Fe<sub>14</sub>NDC-9, the Fe2p XPS spectrum was analysed as well. Due to the poor signal observed for iron (**Fig. 2.8a-b**), the thorough deconvolution of the Fe2p spectrum was difficult, however a tentative deconvolution exhibited a peak for Fe-N<sub>x</sub> at 708.40 eV (**Fig. 2.6d**). Additionally, Fe (706.60 eV) and Fe-oxides (709.71 eV, 711.40 eV, 712.50 eV) were observed. Satellite peaks were present at binding energies > 715.00 eV. These peak assignments for Fe were previously reported.<sup>74-76</sup> In contrast, for Fe<sub>14</sub>NDC-9-NT, the Fe2p spectral resolution was improved and the deconvoluted peaks corresponded to Fe-N<sub>x</sub> and Fe<sub>3</sub>O<sub>4</sub> species (**Fig. 2.8c**). Combined TG-DTA (**Fig. 2.8d**) and ICP-AES (**Table 2.1**) showed that iron content in Fe<sub>14</sub>NDC-9-NT (7.92 wt%) was much higher than Fe<sub>14</sub>NDC-9 (3.5 wt%). This is suggestive of leaching by HF during the removal of the template for Fe<sub>14</sub>NDC-9, resulting in the low signal for iron in the XPS (**Fig. 2.8a-b**).

From survey spectra in **Fig. 2.8a**, we could see the higher intensity of Fe2p peak in Fe<sub>14</sub>NDC-9-NT in comparison with Fe<sub>14</sub>NDC-9. Thus, the resolution of the Fe2p was more suitable for the deconvolution as shown in **Fig. 2.8c**. Then, TG measurement under oxygen environment which burned off the carbons resulting in only the oxide of iron as residue (**Fig. 2.8d**) which was 3.48 wt% and 9.87 wt% and for Fe<sub>14</sub>NDC-9 and Fe<sub>14</sub>NDC-9-NT respectively. It was conspicuous that in addition to the removal of silica template, HF also leached out fraction of soluble, free and unprotected inorganic particles.

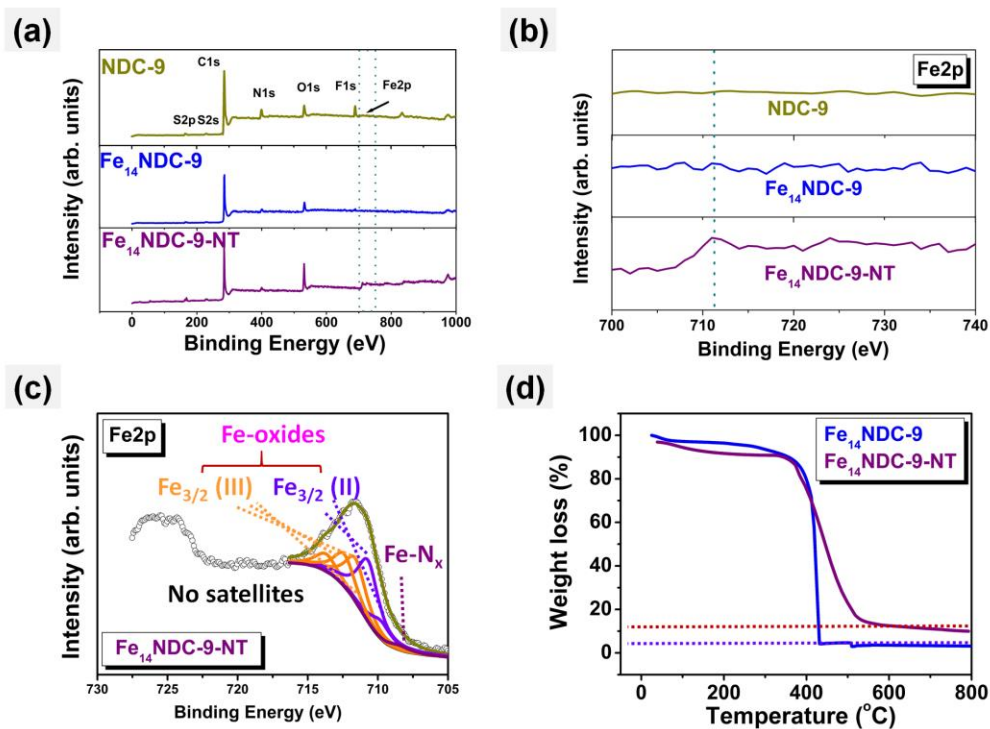


**Fig. 2.8.** (a) Survey XPS spectra, (b) enlarged view of Fe2p survey spectra, (c) Fe2p HR-XPS deconvoluted spectrum, and (d) TG-DTA curves under 100 mL min<sup>-1</sup> flow rate of O<sub>2</sub>.

Additionally, S2p spectral deconvolution displayed (Fig. 2.6e) peaks at 163.89 eV and 165.06 eV referring to thiophene-like species, and at 168.70 eV stemming from the oxidized sulfur species respectively.<sup>82</sup> C1s XPS deconvolution showed peaks (Fig. 2.6f) assigned to  $C_{sp^2}$ , C-heteroatoms supporting the N1s, Fe2p, and S2p spectra as shown in Fig. 2.6c-e and shake-up satellites at higher binding energy.<sup>70,82</sup> EDS mapping further supported the presence of heteroatoms in Fe<sub>14</sub>NDC-9 (Fig. 2.6).

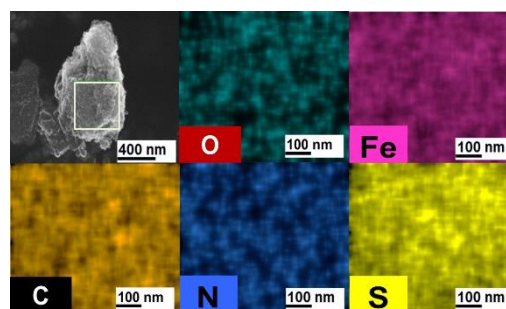


Fig. 2.9. EDS elemental mapping image of Fe<sub>14</sub>NDC-9 showing the distribution of carbon, nitrogen, oxygen, sulfur, and iron over the selected area of FE-SEM image of the corresponding sample.

Combining these results, it was evident that during template removal by HF, composition of iron in Fe<sub>14</sub>NDC-9 was changed and we obtained relatively lower loading of iron in the final product comparing the initial loading in the precursor. This also clarifies the noisy response of Fe2p spectra of Fe<sub>14</sub>NDC-9 described in the main text (Fig. 2.6d) and the difficulty in deconvolution. Moreover, in-detail spectroscopic analysis gave us solid understanding about the textural (micro-mesoporous network) and microscopic features (states and configuration of iron, nitrogen and sulfur on graphene layer) of the FeNDCs, which could be crucial to their catalytic activity.

### 2.3.2. Catalytic activity and stability of protic salt derived iron-doped porous carbons

Firstly, as a prototype example, Fe<sub>14</sub>NDC-9 was investigated in detail via hydrodynamic voltammetry and compared with commercial Pt/C.

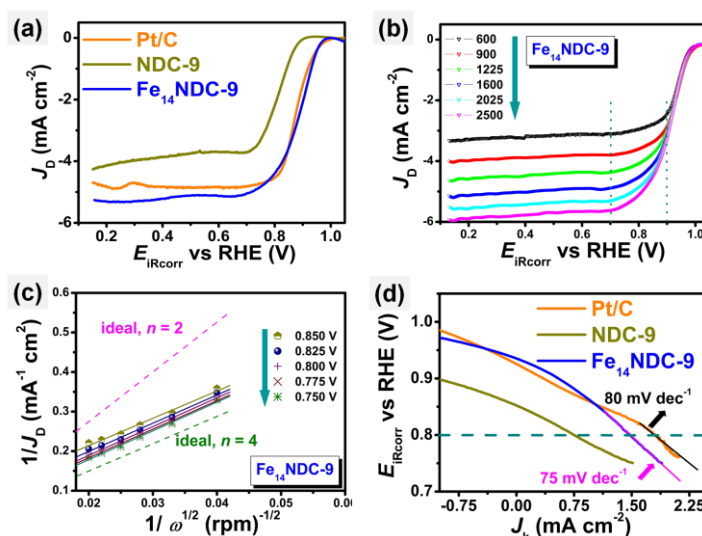


Fig. 2.10. (a) RDE voltammograms showing disk current density in O<sub>2</sub>-saturated 0.1 M KOH at a scan rate of 10 mV s<sup>-1</sup> under rotation rate of 1600 rpm. (b) RDE voltammograms as a function of rotation rate (600–2500 rpm) and the corresponding (c) Koutecky-Levich plots at potentials from 0.85 to 0.75

V. (d) Tafel plots. In all cases, the temperature was 25 °C and the loading amounts of NPM-based catalyst and Pt/C were 600  $\mu\text{g cm}^{-2}$  and 50  $\text{mg}_{\text{Pt}} \text{cm}^{-2}$  respectively.

As shown in Fig. 2.10a, in an alkaline medium,  $\text{Fe}_{14}\text{NDC-9}$  exhibited an onset potential of 0.968 V, which was notably higher than that of NDC-9 (0.893 V) and close to that of commercial Pt/C (0.986 V). Moreover, the ring current response was significantly lower than NDC-9 (Fig. 2.11a) for  $\text{Fe}_{14}\text{NDC-9}$  (Fig. 2.11b), owing to the reduced amount of peroxide formation. Thus, the electron transfer number for  $\text{Fe}_{14}\text{NDC-9}$  was 4.0 akin to that of Pt/C, in contrast with NDC-9 at low overpotential (Fig. 2.11d).

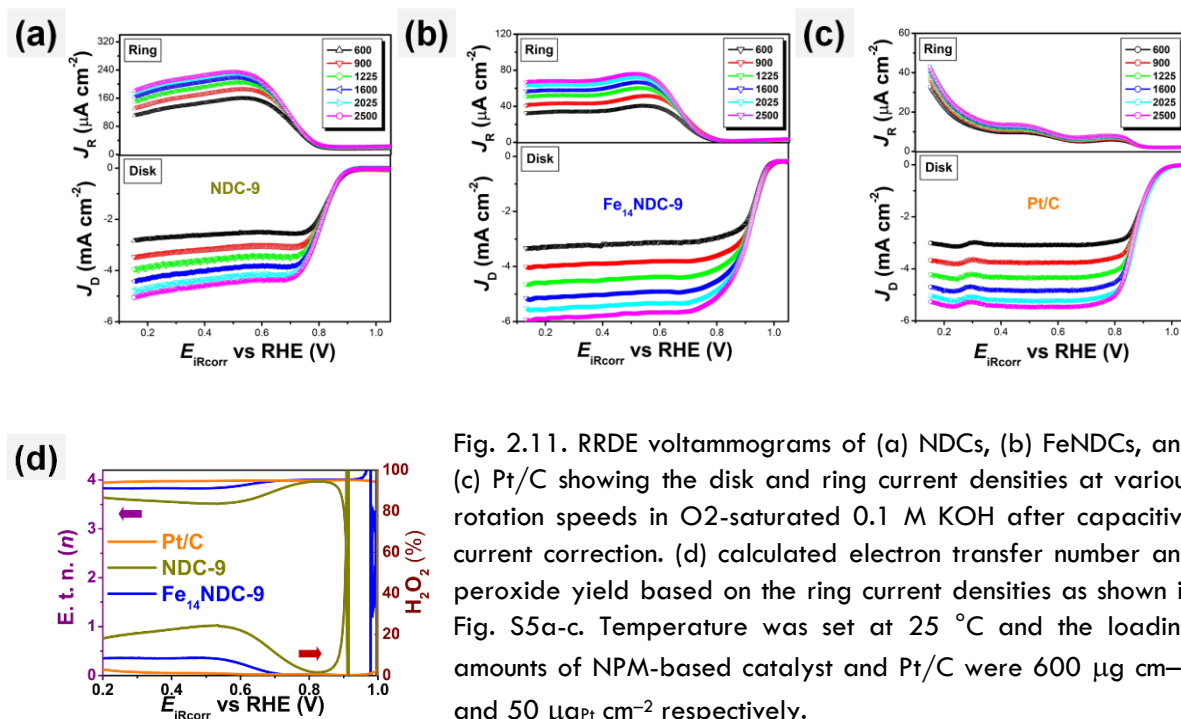


Fig. 2.11. RRDE voltammograms of (a) NDCs, (b) FeNDCs, and (c) Pt/C showing the disk and ring current densities at various rotation speeds in  $\text{O}_2$ -saturated 0.1 M KOH after capacitive current correction. (d) calculated electron transfer number and peroxide yield based on the ring current densities as shown in Fig. S5a-c. Temperature was set at 25 °C and the loading amounts of NPM-based catalyst and Pt/C were 600  $\mu\text{g cm}^{-2}$  and 50  $\mu\text{g}_{\text{Pt}} \text{cm}^{-2}$  respectively.

This outlines the beneficial effect of iron addition in NDCs, which can enhance the activity of framework of NDCs by creating new active sites such as  $\text{N}_x\text{-Fe}^{7,9-10,74-75}$  or enhancing the activity of pre-existing sites i. e., N-py/N-g (valley) by interacting/integrating into the carbon network, as mentioned in earlier studies.<sup>8,34,83</sup> The electron transfer number was also assessed by K-L plot analysis (Fig. 2.10b-c) suggested that the ORR kinetics of  $\text{Fe}_{14}\text{NDC-9}$  were consistent with 4e transfer, supporting the high activity of  $\text{Fe}_{14}\text{NDC-9}$  in alkaline media. The nearly 4e transfer process was further supported by the high half-wave potential ( $E_{1/2} = 0.888 \text{ V}$ ) for  $\text{Fe}_{14}\text{NDC-9}$  (Fig. 2.10a).

Furthermore, the Tafel slope for  $\text{Fe}_{14}\text{NDC-9}$  ( $75 \text{ mV dec}^{-1}$ ) was lower than Pt/C ( $80 \text{ mV dec}^{-1}$ ), again supporting the existence of high kinetic current density in the low overpotential region (Fig. 2.10d).<sup>84</sup> The result of the Tafel plot implies that the first electron transfer is the rate-determining step for  $\text{Fe}_{14}\text{NDC-9}$ , like that of platinum.<sup>75</sup> Such high activity of FeNDCs has already been noted for various precursors such as MOF, polymer, carbon fibers etc.<sup>1,8-10,14-17,34,75,83</sup> and our results are comparable (see Table A 2.4) with the top ranked catalysts reported so far, without any support/additive nor complicated synthetic recipe.

In addition to this, the catalytic activity of Fe<sub>14</sub>NDC-9 was also investigated in 0.1 M HClO<sub>4</sub>, exhibiting lower activity in contrast with 0.1 M KOH (**Fig. 2.12a-d**), which has been reviewed by Masa *et. al.*<sup>85</sup> in detail.

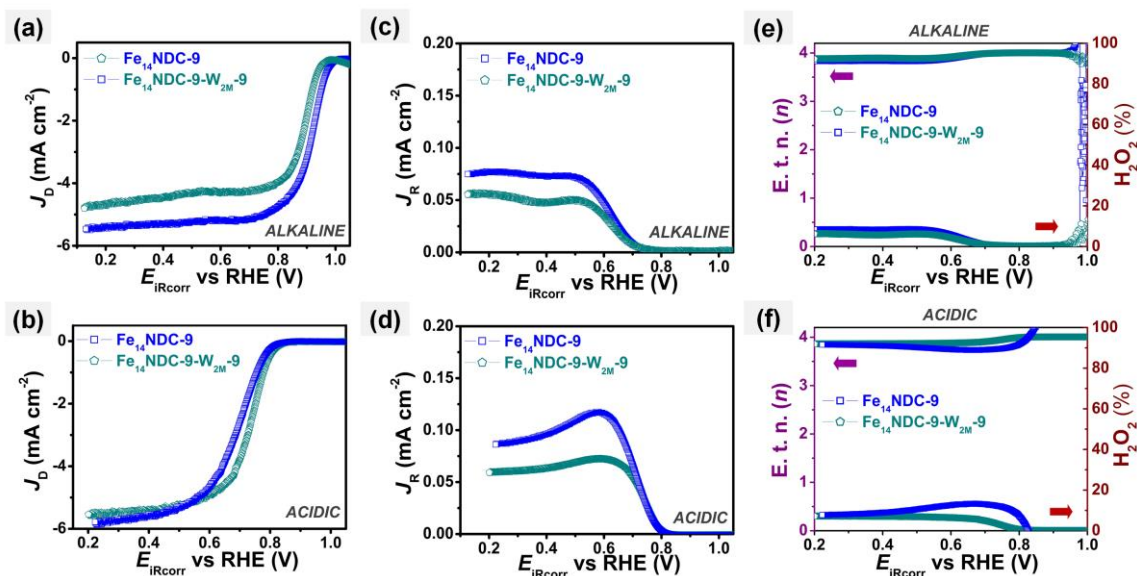


Fig. 2.12. RRDE voltammograms for iron doped carbons showing disk and ring current densities and the calculated electron transfer number based on the ring current densities for (a,c,e) alkaline (0.1 M KOH) and (b,d,f) acidic (0.1 M HClO<sub>4</sub>) electrolytes respectively in O<sub>2</sub>-saturated under 1600 rpm with scan rate of 10 mV s<sup>-1</sup> at 25 °C. Loading of the catalyst was 600 μg cm<sup>-2</sup>.

Considering the likely instability in acidic electrolyte of free and unprotected inorganic particles that exist in Fe<sub>14</sub>NDC-9 (**Fig. 2.6d**), the post treated sample Fe<sub>14</sub>NDC-9-W<sub>2M</sub>-9 was selected for further analysis in acidic electrolyte. Previously, it was shown by Kramm *et. al.* that such treatment was pivotal for the enhanced activity of iron doped carbons.<sup>86</sup>

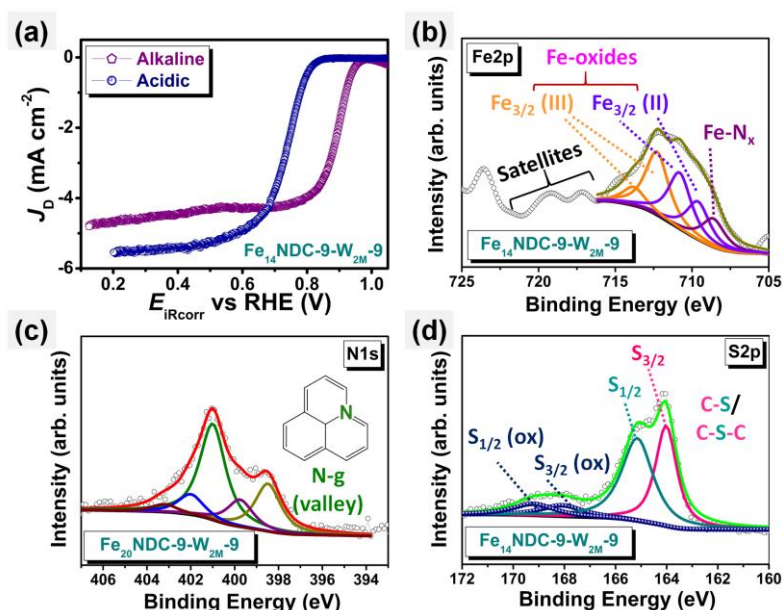


Fig. 2.13. (a) LSV in 0.1 M KOH and 0.1 M HClO<sub>4</sub>, deconvoluted (b) N1s, (c) Fe2p, and (d) S2p XPS spectra.

In **Fig.2.13a**, Fe<sub>14</sub>NDC-9-W<sub>2M</sub>-9 displayed an onset potential of 0.821 V and a 159 mV negatively shifted half-wave potential, like a MOF-based active material.<sup>8</sup> Additionally, the electron transfer number for Fe<sub>14</sub>NDC-9-W<sub>2M</sub>-9 was 4.0 in the low overpotential region (> 0.6 V) in acidic media as shown in **Fig.2.13d**, further supporting the K-L analysis (**Fig.2.14a-b**).

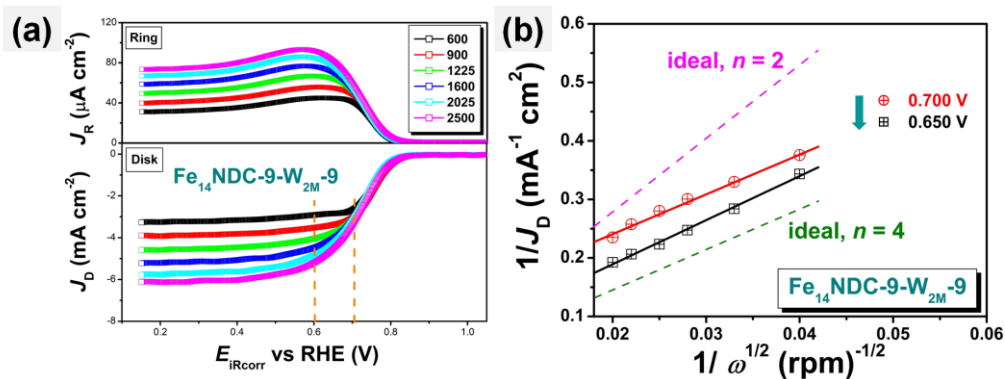


Fig. 2.14. (a) RRDE voltammograms showing the disk and ring current densities, and (b) K-L plot between 0.6 to 0.7 V in O<sub>2</sub>-saturated 0.1 M HClO<sub>4</sub> under 1600 rpm with scan rate of 10 mV s<sup>-1</sup> at 25 oC. Loading of the catalyst was 600 □g cm<sup>-2</sup>.

In comparison with Fe<sub>14</sub>NDC-9, Fe<sub>14</sub>NDC-9-W<sub>2M</sub>-9 demonstrated similar peroxide yield and electron transfer in 0.1 M KOH (**Fig.2.12e**). In contrast, in 0.1 M HClO<sub>4</sub>, Fe<sub>14</sub>NDC-9-W<sub>2M</sub>-9 displayed lower peroxide yield and thus higher electron transfer number in the entire potential range (**Fig.2.12f**).

During the hot acid leaching step, unprotected particles were removed, supporting the Fe2p spectra in **Fig.2.13b** (c.f. **Fig.2.6d**). The second pyrolysis step increased the dominance of N-g (valley) site over N<sub>x</sub>-Fe as shown in **Fig.2.13c** (c.f. **Fig.2.6c**) and **Fig. 2.7**, and oxidized sulfur species were notably reduced (**Fig.2.13d**, c.f. **Fig.2.6e**). These phenomena were previously observed for Fe based catalyst.<sup>87</sup> Thus, post treatment of Fe<sub>14</sub>NDC-9 was beneficial towards ORR at lower pH. It is important to note here the pH dependence of the catalytic site, for instance N<sub>x</sub>-Fe.<sup>8,17,34</sup>

Recently, the Sun group<sup>88</sup> reported that N-py undergoes protonation in acidic electrolyte, which has a negative impact on the catalytic activity of N<sub>x</sub>-Fe, due to the resulting anion adsorption.<sup>89</sup> It has been further suggested that N-g is less susceptible to protonation in acidic electrolyte,<sup>88</sup> and high activity was observed for FeNDCs with a N1s (XPS) band position akin to our result;<sup>87-88</sup> we speculate that the reported material therefore also contained a higher amount of N-g. Gewirth *et. al.*<sup>90</sup> also noted that N<sub>x</sub>-Fe is not essential for ORR activity in acidic electrolyte, also echoed by other reports.<sup>8,91</sup> In this case, non-coordinated iron encapsulated by a graphitic shell could act as an efficient active site.<sup>8,34,83,91</sup>

We hypothesize that in acidic electrolyte, enrichment of the N-g (valley) site could be important to increase the mass activity of the catalyst. Furthermore, as shown in Fig. 12a and Fig. 13a, even in alkaline electrolyte, Fe<sub>14</sub>NDC-9-W<sub>2M</sub>-9 displayed relatively high mass activity. This suggests that N-g (valley) could contribute to the catalytic activity in

electrolytes with different pH. Designing a catalyst with the enrichment of this type of active site could be useful for application of FeNDCs in electrolytes with wider pH range.

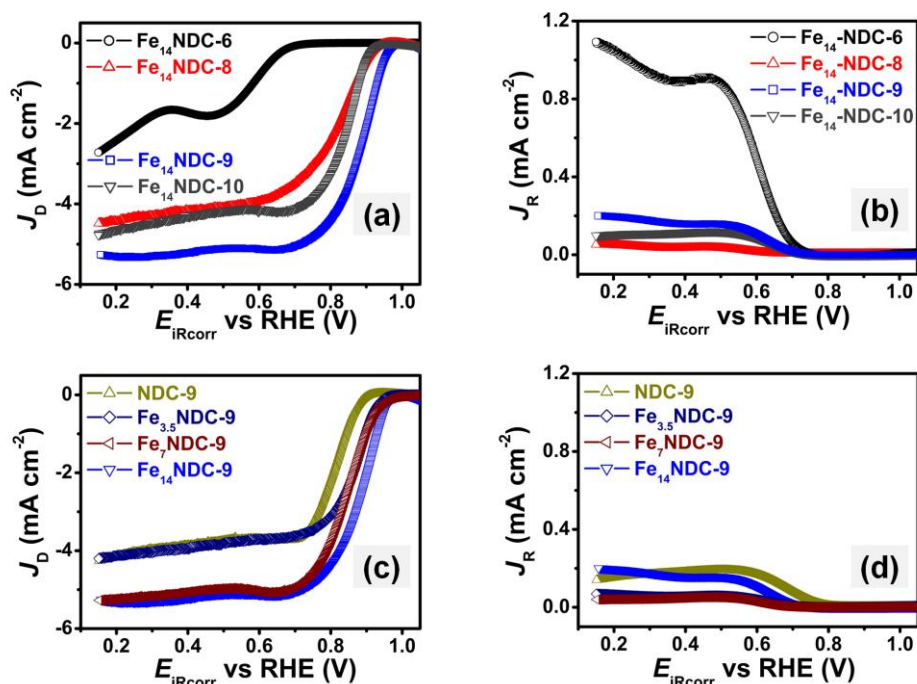


Fig. 2.15. RRDE voltammograms as a function of (a) carbonization temperature, (b) iron loading showing the disk and ring current densities in O<sub>2</sub>-saturated 0.1 M KOH 1600 rpm with scan rate of 10 mV s<sup>-1</sup> at 25 oC. Loading of the catalyst was 600 □g cm<sup>-2</sup>.

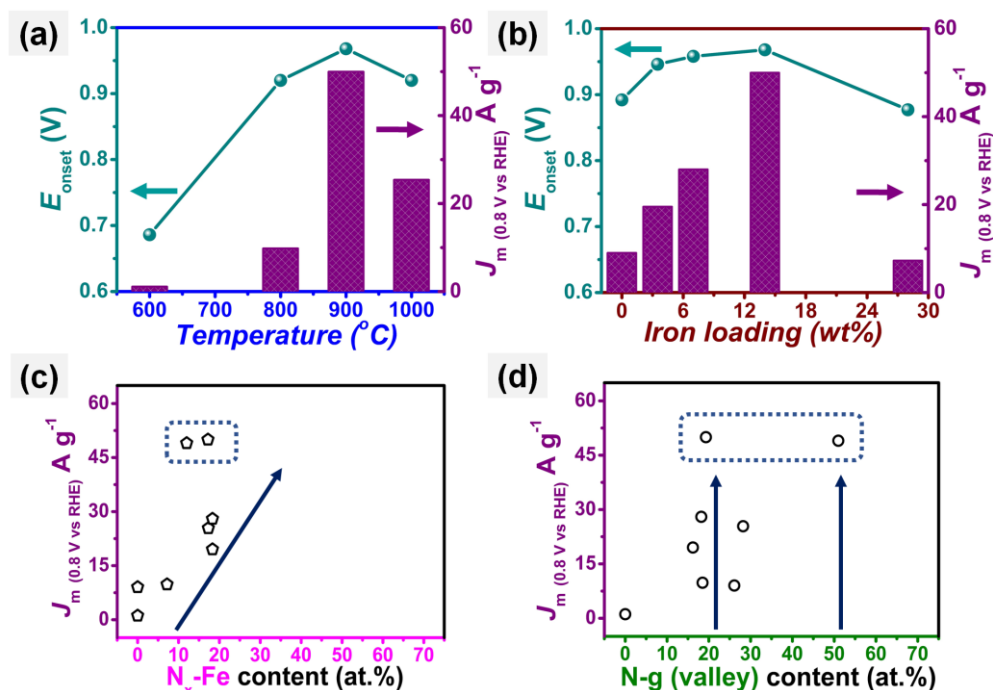


Fig. 2.16. Change in onset potential and mass activity of carbons as a function of (a) annealing temperature, and (b) iron loading in 0.1 M KOH. Mass activity correlation plot with respect to (c) N<sub>x</sub>-Fe, and (d) N-g (valley). Onset potential was calculated from the LSV of each sample shown in Fig. S6a,

S8a, c, and S9a. Content of  $N_x$ -Fe, and N-g (valley) was taken from Table S3 which is also shown as a bar chart in Fig. 5.

To further validate the hypothesis, oxygen reduction activity of FeNDCs prepared under different synthetic conditions was evaluated (Fig. 2.15a-d) as a function of  $N_x$ -Fe and N-g (valley) in alkaline media, as shown in Fig. 2.16a-d.  $Fe_{14}NDC-9$  exhibited the most positive onset potential of 0.968 V and highest mass activity of  $49.98 \text{ A g}^{-1}$  as shown in Fig. 2.16a-b with dominant  $N_x$ -Fe content (shown in the dotted blue box in Fig. 2.16c, the other data point is for the acid treated  $Fe_{14}NDC-9-W_{2M}-9$ ).

Interestingly, mass activity was found to be dependent on the concentration of  $N_x$ -Fe, as was previously reported for  $FeN_xC$  type catalysts.<sup>74,79,88, 91</sup> Conversely, FeNDCs displayed an efficient catalytic response at moderate and high content of N-g (valley), which is known to exhibit ORR activity.<sup>92</sup> Here we note a report on CNT based FeNDCs demonstrating that  $Fe/Fe_3C$  nanocrystals boosted the activity of  $Fe-N_x$ <sup>93</sup> owing to the enhancement in the content of the N-g component in the material. So, with a combination of  $Fe-N_x$  and N-g aided by  $Fe/Fe_3C$  nanocrystals, the catalyst ( $Fe@C$ -FeNC-2) exhibited the best performance.<sup>8,91,92</sup> In contrast, in our system we could see that increase of iron loading promoted the formation of N-g (valley) except for  $Fe_{28}NDC-9$  as shown in Fig. 2.7. Interestingly, activity dropped significantly at high iron loading ( $Fe_{28}NDC-9$ , Fig. 2.17a-b) owing to the aggregation of iron derived nanoparticles, further filling the porous network observed by TEM (Fig. 2.17 inset).

Furthermore, we note that activity of N-py has been unraveled by Guo *et. al.*<sup>94</sup> by precise doping of HOPG with nitrogen. As shown in Fig. 2.16 (dashed blue box,  $Fe_{14}NDC-9$  and  $Fe_{14}NDC-9-W_{2M}-9$ ), for N-py at moderate content (Table 2.5), high catalytic activity was observed, but only when  $N_x$ -Fe ( $Fe_{14}NDC-9$ ) or N-g (valley) ( $Fe_{14}NDC-9-W_{2M}-9$ ) was in higher content in the FeNDCs. Here some caution is pertinent, as in the XPS spectral deconvolution for N1s, the peak assigned to N-py also corresponds to disordered  $N_x$ -Fe, another active spot for ORR.<sup>74,78</sup> Henceforth, in the case of  $Fe_{14}NDC-9-W_{2M}-9$ , high mass activity was maintained in 0.1 M KOH as displayed in Fig. 2.16d (the blue dotted region, the other data point with high activity, at lower % N-g valley content, is  $Fe_{14}NDC-9$ ) with dominant N-g (valley) sites.

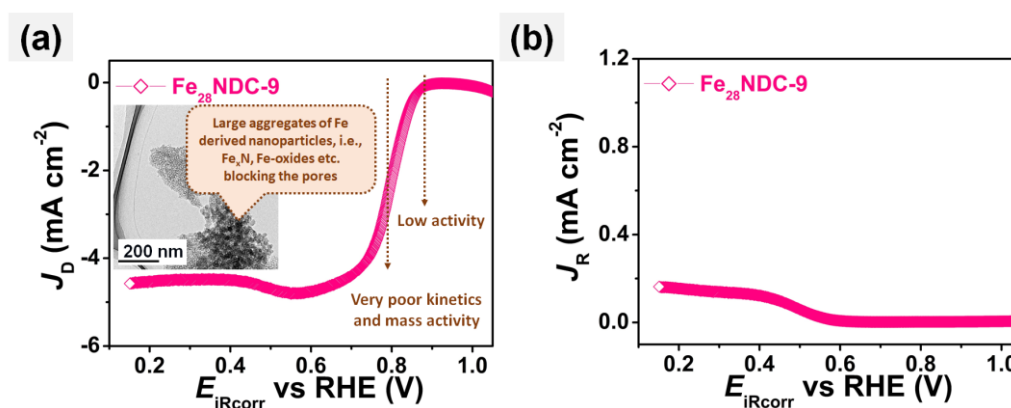


Fig. 2.17. RRDE voltammogram of FeNDCs showing (a) disk (inset: TEM micrograph) and (b) ring current density in O<sub>2</sub>-saturated 0.1 M KOH 1600 rpm with scan rate of 10 mV s<sup>-1</sup> at 25 °C. Loading of the catalyst was 600  $\square$ g cm<sup>-2</sup>.

Overall, this is supportive of the fact that N-g (valley) can act as a co-catalytic centre in FeNDCs. For Fe<sub>14</sub>NDC-9, balanced doping of N<sub>x</sub>-Fe and N-g (valley) was achieved at intermediate synthetic conditions, i.e. 900 °C.<sup>19</sup>

This is very intriguing as the precursor mixture of Fe<sub>14</sub>NDC-9 consisted of two phases (**Fig. 2.19**). From 3.5-7 wt% of iron, the mixture was homogeneous, consisting of only the miscible FeCl<sub>3</sub> phase. On the contrary, from 14-28 wt% of iron, the mixture was composed of both miscible (Fe-Phen complex) and immiscible phases of FeCl<sub>3</sub>, presumably owing to the formation of a hydrated FeCl<sub>3</sub> complex (**Fig. 2.19**).

So, during carbonization from the miscible phase, the maximum N<sub>x</sub>-Fe (of samples studied in this work) was generated, and excess FeCl<sub>3</sub> was reduced into Fe/Fe<sub>x</sub>C, which facilitates graphitization and possibly formation of N-g (valley).<sup>93</sup> So, from Fe<sub>3.5</sub>NDC-9 and Fe<sub>7</sub>NDC-9, mass activity was controlled by the N<sub>x</sub>-Fe site and then further increased by the increase of N-g site. On the contrary, for Fe<sub>28</sub>NDC-9, mass activity reduced greatly owing to the blocking of active sites by the aggregated particles as shown in **Fig. 2.17a-b**. However, considering the acidic medium, 0.1 M HClO<sub>4</sub>, both Fe<sub>14</sub>NDC-9 (**Fig. 2.12a-b**) and Fe<sub>14</sub>NDC-9-W<sub>2M</sub>-9 (**Fig. 2.12a-b** c.f. **Fig. 2.13a**) displayed much lower mass activity of 9.55 and 20.77 A g<sup>-1</sup> respectively, a common observation for other FeNDCs catalysts as well.<sup>8,34,14-17,87,95-96</sup>

Sulfur has been found to be a catalyst promoter in iron doped carbons co-doped with dual non-metallic heteroatoms, such as nitrogen and sulfur.<sup>87</sup> Using aprotic ionic liquid as carbonaceous precursor, Strasser *et. al.*<sup>97</sup> mentioned the superior effect of sulfur-nitrogen co-doping in contrast with phosphorous-nitrogen and boron-nitrogen co-doping in iron doped catalyst. However, in the current system, sulfur stems from the anion of the PS which undergoes oxidative polymerization during annealing,<sup>29,45</sup> and composition of sulfur was low and essentially invariant in the FeNDCs synthesized in this study (maximum 1.37% (atom), **Table 2.5**). Additionally, we have only assessed one anion (HSO<sub>4</sub><sup>-</sup>) so far. Thus, correlation between the mass activity and the sulfur was not possible.

Finally, we consider the stability of the prepared electrocatalysts in acidic and alkaline solution. The stability of the catalyst was assessed by chronoamperometry (i-t) and cyclic stability tests. Firstly, chronoamperometric analysis (**Fig. 2.20a, b**) revealed higher retention of current density for Fe<sub>14</sub>NDC-9 (84.7%) than for Pt/C (77.5%). It was further improved for Fe<sub>14</sub>NDC-9-W<sub>2M</sub>-9 (87.9%) stressing the effect of post treatment.<sup>96</sup>

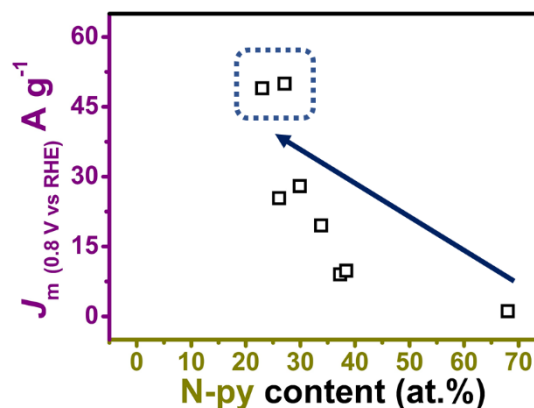


Fig. 2.18. Mass activity of FeNDCs as a function of N-py in 0.1 M KOH.

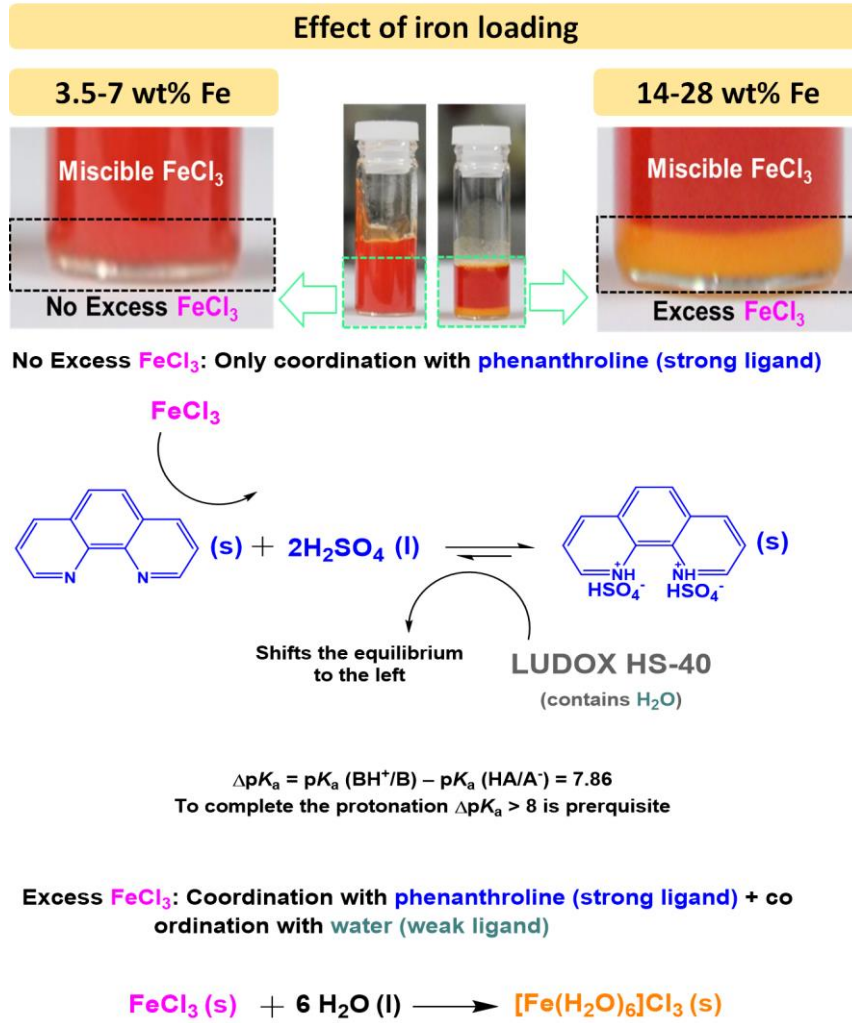


Fig. 2.19. Effect of iron loading from 3.5 to 28 wt.% in a 2.0 g mixture of protic salt and FeCl<sub>3</sub> combined with colloidal silica.<sup>38</sup>

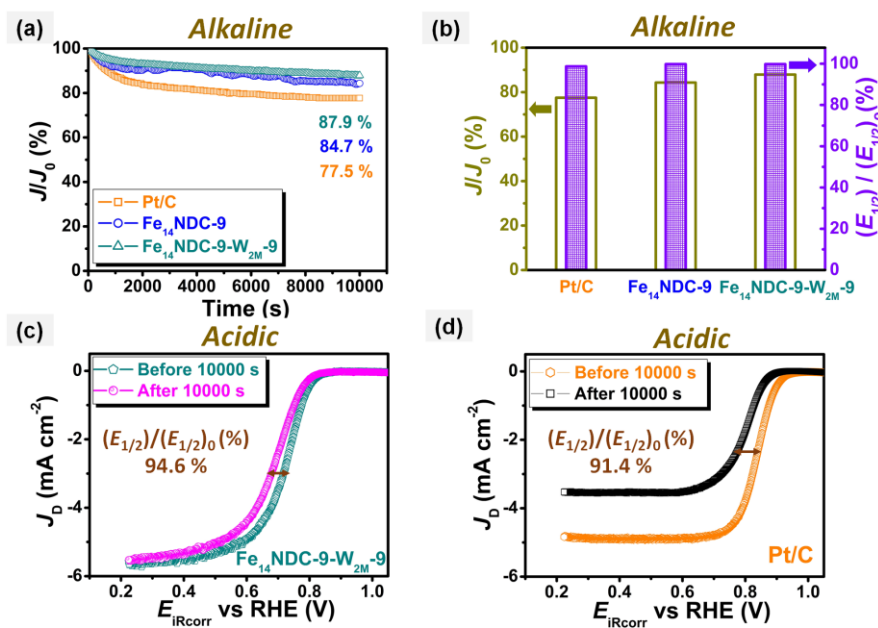


Fig. 2.20. (a) Chronoamperometry (i-t) at 0.8 V under 1600 rpm, (b) retention of current density and half-wave potential after 10000s, and 2000 CV cycles, (c-d) LSV before and after 2000 CV cycles. All the experiments were conducted in O<sub>2</sub>-saturated 0.1 M KOH and 0.1 M HClO<sub>4</sub>.

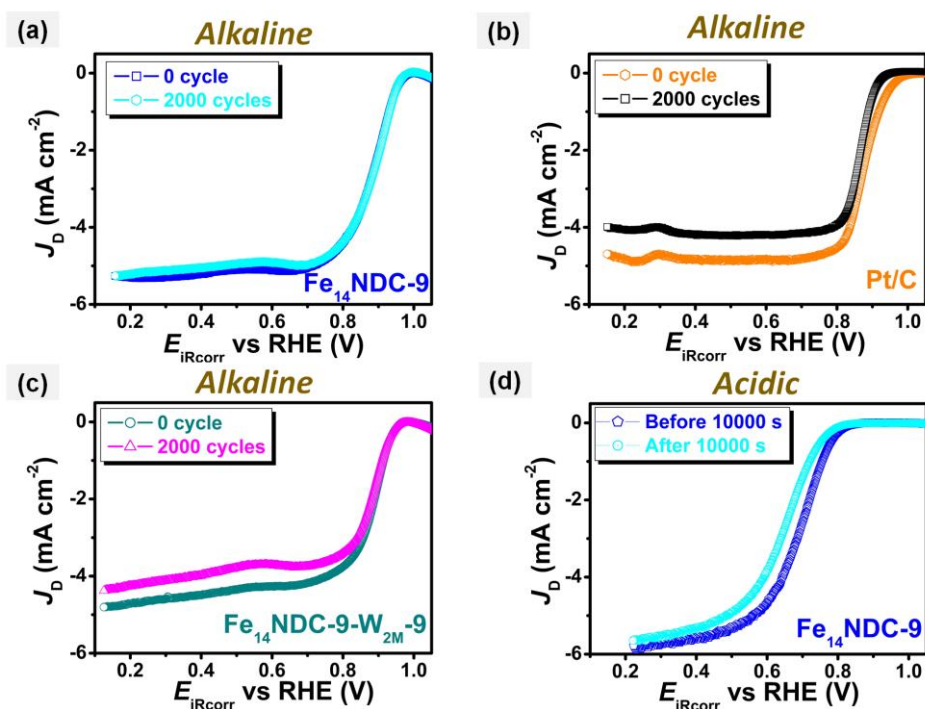


Fig. 2.21. RDE voltammograms before and after (a-c) 2000 cycles cyclic stability test in 0.1 M KOH, and (d) chronoamperometric test in 0.1 M HClO<sub>4</sub>.

As demonstrated in **Fig. 2.20b**, the RDE voltammograms of Fe<sub>14</sub>NDC-9 exhibit 99.8% (**Fig. 2.21a**) retention of the half-wave potential after 2000 CV cycles in O<sub>2</sub>-saturated 0.1 M KOH, which is comparable to the behavior of Pt/C (98.7%, **Fig. 2.21b**). Moreover, in LSV negligible loss of the onset potential was observed for Fe<sub>14</sub>NDC-9 (**Fig. 2.21a**), whereas only 70% of the initial activity was retained for Pt/C (**Fig. 2.21b**) in alkaline electrolyte, further validated by an earlier report.<sup>93</sup> The loss in intrinsic activity (onset potential) of the materials might result from deactivation of some part of the electrocatalyst in the catalyst layer during the stability test. A loss in current density was also apparent (**Fig. 2.21a-b**), possibly owing to loss of the catalyst material during long cycle operations.<sup>90</sup>

In addition to this, Fe<sub>14</sub>NDC-9-W<sub>2M</sub>-9 also displayed high retention of current density (**Fig. 2.20a-b**) and half-wave potential (**Fig. 2.20b**, **Fig. 2.21c**) in 0.1 M KOH. On the other hand, in 0.1 M HClO<sub>4</sub>, Fe<sub>14</sub>NDC-9-W<sub>2M</sub>-9 showed higher retention (94.6%) of the half-wave potential after chronoamperometry at 0.7 V (**Fig. 2.20c**) in contrast with Pt/C (91.4%, **Fig. 2.20d**). Moreover, and expectedly, it was also more effective than Fe<sub>14</sub>NDC-9 as shown in **Fig. 2.21d**. But, we acknowledge that a more rugged stability test is necessary to further validate this outcome.

These preliminary stability results for Fe<sub>14</sub>NDC-9 are promising in both electrolytes and can be attributed to the following factors. The porous architecture allows efficient transport of reactants and products. Iron-precursor-derived species, such as Fe-N<sub>x</sub>, Fe/Fe-oxides are well-integrated within the carbon phase.<sup>3</sup> Also, for Fe<sub>14</sub>NDC-9-W<sub>2M</sub>-

9, stability of the catalyst was further enhanced in both alkaline and acidic media (**Fig. 2.20b-c**) owing to the removal of free acid soluble particles and reduction of oxide content, i. e.,  $-\text{SO}_x-$  during the post treatment processes. Thus, removal of unstable and less active species was beneficiary for reduction in ring current density observed for  $\text{Fe}_{14}\text{NDC-9-W}_{2\text{M-9}}$  in RRDE voltammograms as shown in **Fig. 2.12c-d**. So, lesser amount  $\text{H}_2\text{O}_2$  was generated and thereby suppressed the degradation of active sites in the FeNDCs.<sup>25,98</sup>

#### 2.4. Conclusion

In summary, we have reported herein the fabrication of a highly efficient ORR catalyst based on a low-cost and robust carbonaceous precursor, protic salt. This impressive performance was achieved via the successful incorporation of a silica template with the combination of a protic salt and a simple iron salt. The derived carbon materials had interesting microscopic features, including high specific surface area, micro-mesoporosity with dominant mesopores and active motifs such as  $\text{N}_x\text{-Fe}$ , N-py, and N-g (valley). The prototype catalyst,  $\text{Fe}_{14}\text{NDC-9}$ , displayed the highest onset potential of 0.968 V and a half-wave potential of 0.888 V in alkaline media. For  $\text{Fe}_{14}\text{NDC-9}$ , the ORR proceeded exclusively via a 4e transfer process. Also, in acidic media,  $\text{Fe}_{14}\text{NDC-9-W}_{2\text{M-9}}$  showed onset potential at 0.821 V, 4e transfer process in the low overpotential region, and a half-wave potential of 0.730 V. Short-term stability tests in both electrolytes were reasonable. Overall, this result is encouraging, as the developed catalyst is free from any additional high-surface-area carbon support or additives like MOFs. Moreover, simplicity of the synthesis of the protic salt,  $[\text{Phen}][2\text{HSO}_4]$ , and the versatility of the ionic liquid platform make this molecular-level carbon precursor a unique approach for developing transition metal based catalysts, i.e., iron for fuel cells.

#### 2.5. References

- 1 F. Jaouen, E. Proietti, M. Lefevre, R. Chenitz, J.-P. Dodelet, G. Wu, H.T. Chung, C. M. Johnston, and P. Zelenay, *Energy Environ. Sci.*, 2011, **4**, 114–130.
- 2 L. Dai, D. Wook Chang, J.-B. Baek, and W. Lu, *Small*, 2012, **8**, 1130–1166.
- 3 D. Banham, S. Ye, K. Pei, J.-I. Ozaki, T. Kishimoto and Y. Imashiro, *J. Power Sources*, 2015, **285**, 334–348.
- 4 T. Sawaguchi, T. Matsue, K. Itaya and I. Uchida, *Electrochim. Acta*, 1991, **36**, 703–708.
- 5 R. Jasinski, *J. Electrochem. Soc.*, 1965, **112**, 526–528.
- 6 G. Faubert, R. Cote, D. Guay, J.-P. Dodelet, G. Denes and P. Bertrand, *Electrochim. Acta*, 1998, **43**, 341–353.
- 7 S. Bruller, H. W. Liang, U. I. Kramm, J. W. Krumpfer, X. L. Feng and K. Müllen, *J. Mater. Chem. A*, 2015, **3**, 23799–23808.
- 8 K. Strickland, E. Miner, Q. Jia, U. Tylus, N. Ramaswamy, W. Liang, M.-T. Sougrati, F. Jaouen and S. Mukerjee, *Nat. Commun.*, 2015, **6**, 7343 (1–8).
- 9 M. Lefèvre, E. Proietti, F. Jaouen and J.-P. Dodelet, *Science*, 2009, **324**, 71–74.
- 10 E. Proietti, F. Jaouen, M. Lefèvre, N. Larouche, J. Tian, J. Herranz and J.-P. Dodelet, *Nat. Commun.*, 2011, **2**, 416 (1–9).
- 11 Y. Zheng, Y. Jiao, and S. Z. Qiao, *Adv. Mater.*, 2015, **27**, 5372–5378.

- 12J. Zhang, D. He, H. Su, X. Chen, M. Pan and S. Mu, *J. Mater. Chem. A*, 2014, **2**, 1242–1246.
- 13B. Winther-Jensen, O. Winther-Jensen, M. Forsyth and D. R. Macfarlane, *Science*, 2008, **321**, 671–674.
- 14H. Liu, Z. Shi, J. Zhang, L. Zhang and J. Zhang, *J. Mater. Chem.*, 2009, **19**, 468–470.
- 15X. Yan, K. Liu, T. Wang, Y. You, J. Liu, P. Wang, X. Pan, G. Wang, J. Luo and J. Zhu, *J. Mater. Chem. A*, 2017, **5**, 3336–3345.
- 16L. Yang, Y. Bai, H. Zhang, J. Geng, Z. Shao and B. Yia, *RSC Adv.*, 2017, **7**, 22610–22618.
- 17L. Lin, Q. Zhu, and A.-W. Xu, *J. Am. Chem. Soc.*, 2014, **136**, 11027–11033.
- 18M. Lefèvre, J.-P. Dodelet and P. Bertrand, *J. Phys. Chem. B*, 2000, **104**, 11238–11247.
- 19T. Onodera, T. Mizukami, S. Suzuki, J. Kawaji, K. Yamaga and T. Yamamoto, *Catal. Commun.*, 2014, **43**, 66–71.
- 20M. Bron, J. Radnik, M. Fieber-Erdmann, P. Bogdanoff and S. Fiechter, *J. Electroanal. Chem.*, 2002, **535**, 113–119.
- 21S. Brocato, A. Serov and P. Atanassov, *Electrochim. Acta*, 2013, **87**, 361–365.
- 22M. Bron, S. Fiechter, M. Hilgendorff and P. Bogdanoff, *J. Appl. Electrochem.*, 2002, **32**, 211–216.
- 23T. Palaniselvam, B. P. Biswal, R. Banerjee and S. Kurungot, *Chem. Eur. J.*, 2013, **19**, 9335–9342.
- 24J. Shuia, C. Chena, L. Grabstanowicza, D. Zhaod and D.-J. Liu, *PNAS*, 2015, **112**, 10629–10634.
- 25G. Zhang, R. Chenitz, M. Lefèvre, S. Sun and J.-P. Dodelet, *Nano Energy*, 2016, **29**, 111–125.
- 26F. Charreteur, F. Jaouen and J.-P. Dodelet, *Electrochim. Acta* 2009, **54**, 6622–6630.
- 27G. Wu, K. Artyushkova, M. Ferrandon, J. Kropf, D. Myers and P. Zelenay, *ECS Trans.*, 2009, **1**, 1299–1311.
- 28N. Larouchea, R. Chenitz, M. Lefèvre, E. Proietti and J.-P. Dodelet, *Electrochim. Acta*, 2014, **115**, 170–182.
- 29S. Zhang, M. S. Miran, A. Ikoma, K. Dokko and M. Watanabe, *J. Am. Chem. Soc.*, 2014, **136**, 1690–1693.
- 30J. S. Lee, R. T. Mayes, H. Luo and S. Dai, *Carbon*, 2010, **48**, 3364–3368.
- 31G. Rohan, Y. Chen, A. Serov, K. Artyushkova and P. Atanassov, *Electrochem. Commun.*, 2016, **72**, 140–143.
- 32D. Sebastián, V. Baglio, A. S. Aricò, A. Serov and P. Atanassov, *Appl. Catal. B: Environ.*, 2016, **182**, 297–305.
- 33R. Kothandaraman, V. Nallathambi, K. Artyushkova and S. C. Barton, *Appl. Catal. B: Environ.*, 2009, **92**, 209–216.
- 34R. Zhou and S. Z. Qiao, *Chem. Commun.*, 2015, **51**, 7516–7519.
- 35S. Gupta, D. Tryk, I. Bae, W. Aldred and E. Yeager, *J. App. Electrochem.*, 1989, **19**, 19–27.
- 36C. D. Liang, K. L. Hong, G. A. Guiochon, J. W. Mays and S. Dai, *Angew. Chem. Int. Ed.*, 2004, **43**, 5785–5789.
- 37F. Pan, Z. Cao, Q. Zhao, H. Liang and J. Zhang, *J. Power Sources*, 2014, **272**, 8–15.

- 38J. Tian, A. Morozan, M.-T. Sougrati, M. Lefèvre, R. Chenitz, J.-P. Dodelet, D. Jones and F. Jaouen, *Angew. Chem. Int. Ed.*, 2013, **52**, 6867–6870.
- 39P. Su, H. Xiao, J. Zhao, Y. Yao, Z. Shao, C. Li and Q. Yang, *Chem. Sci.*, 2013, **4**, 2941–2946.
- 40X. Wang, H. Zhang, H. Lin, S. Gupta, C. Wang, Z. Tao, H. Fua, T. Wang, J. Zheng, W. Gang and X. Li, *Nano Energy*, 2016, **25**, 110–119.
- 41K. Parvez, S. Yang, Y. Hernandez, A. Winter, A. Turchanin, X. Feng and K. Müllen, *ACS Nano*, 2012, **6**, 9541–9550.
- 42Z. Li, G. Li, L. Jiang, J. Li, G. Sun, C. Xia, and F. Li, *Angew. Chem. Int. Ed.*, 2015, **54**, 1494–1498.
- 43F. He, X. Chen, Y. Shen, Y. Li, A. Liu, S. Liu, T. Moric and Y. Zhang, *J. Mater. Chem. A*, 2016, **4**, 6630–6638.
- 44S. Zhang, K. Dokko and M. Watanabe, *Mater. Horiz.*, 2015, **2**, 168–197.
- 45S. Zhang, K. Dokko and M. Watanabe, *Chem. Mater.*, 2014, **26**, 2915–2916.
- 46S. Zhang, A. Ikoma, K. Ueno, Z. Chen, K. Dokko and M. Watanabe, *ChemSusChem*, 2015, **8**, 1608–1617.
- 47D. Banham, F. Feng, T. Fürstenthaupt, K. Pei, S. Ye and V. Birss, *Catalysts*, 2015, **5**, 1046–1067.
- 48X.-K. Ma, N.-H. Lee, H.-J. Oh, J.-W. Kim, C.-K. Rhee, K.-S. Park and S.-J. Kim, *Colloids and Surf. A: Physicochemical and Engineering Aspects*, 2010, **358**, 172–176.
- 49I. M. Kolthoff, D. L. Leussing and T. S. Lee, *J. Am. Chem. Soc.*, 1950, **72**, 2173–2177.
- 50J. A. Bautista-Martinez, L. Tang, J.-P. Belieres, R. Zeller, C. A. Angell and C. Friesen, *J. Phys. Chem. C*, 2009, **113**, 12586–12593.
- 51A. J. Pallenberg, T. M. Marschnera and D. M. Barnhart, *Polyhedron*, 1997, **16**, 2711–2719.
- 52G. A. Renovitch and W. A. Baker, jun., *J. Chem. Soc. A*, 1969, **0**, 75–78.
- 53C. Kaes, A. Katz and M. W. Hosseini, *Chem. Rev.*, 2000, **100**, 3553–3590.
- 54S. Zhang, T. Mandai, K. Ueno, K. Dokko and M. Watanabe, *Nano Energy*, 2015, **13**, 376–386.
- 55A. Cuesta, P. Dhamelincourt, J. Laureyns, A. Martinezalonso and J. M. D Tascon, *Carbon*, 1994, **32**, 1523–1532.
- 56S. Maldonado, S. Morin and K. J. Stevenson, *Carbon*, 2006, **44**, 1429–1437.
- 57L. Yang, N. Larouche, R. Chenitz, G. Zhang, M. Lefèvre, J.-P. Dodelet, *Electrochim. Acta*, 2015, **159**, 184–197.
58. D. W. Marquadt, *J. Soc. Ind. Appl. Math.*, 1963, **11**, 431–441.
59. A. V. Neimark and P. I. Ravikovitch, *Microporous and Mesoporous Mater.*, 2001, **44–45**, 697–707.
60. J. Jagiello and J. P. Olivier, *J. Phys. Chem. C*, 2009, **113**, 19382–19385.
61. U. I. Kramm, J. Herranz, N. Larouche, T. M. Arruda, M. Lefèvre, F. Jaouen, P. Bogdanoff, S. Fiechter, I. Abs-Wurmbach, S. Mukerjee and J.-P. Dodelet, *Phys. Chem. Chem. Phys.*, 2012, **14**, 11673–11688.
62. K. Mamtani, D. Singh, J. Tian, J.-M. M. Millet, J. T. Miller, A. C. Co and U. S. Ozkan, *Catal. Lett.*, 2016, **146**, 1749–1770.
63. U. I. Koslowski, I. Abs-Wurmbach, S. Fiechter and P. Bogdanoff, *J. Phys. Chem. C*, 2008, **112**, 15356–15366.

64. Q. Jia, N. Ramaswamy, H. Hafiz, U. Tylus, K. Strickland, G. Wu, B. Barbiellini, A. Bansil, E. F. Holby, P. Zelenay and S. Mukerjee, *ACS Nano*, 2015, **9**, 12496–12505.
65. K. Artyushkova, B. Kiefer, B. Halevi, A. Knop-Gericke, R. Schlogl and P. Atanassov, *Chem. Commun.*, 2013, **49**, 2539–2541.
66. S. Kattel, P. Atanassov and B. Kiefer, *Phys. Chem. Chem. Phys.*, 2013, **15**, 148–153.
67. S. Kabir, K. Artyushkova, A. Serov, B. Kiefer and P. Atanassov, *Surf. Interface Anal.*, 2016, **48**, 293–300.
68. M. Bron, J. Radnik, M. Fieber-Erdmann, P. Bogdanoff and S. Fiechter, *J. Electroanal. Chem.*, 2002, **535**, 113–119.
69. J. Casanovas, J. M. Ricart, J. Rubio, F. Illas, and J. M. Jimenez-Mateos, *J. Am. Chem. Soc.*, 1996, **118**, 8071–8076.
70. Y. Yamada, J. Kim, S. Matsuo and S. Sato, *Carbon*, 2014, **70**, 59–74.
71. Y. Yamada, Y. Suzuki, H. Yasuda, S. Uchizawa, K. Hirose-Takai, Y. Sato, K. Suenaga and S. Sato, *Carbon*, 2014, **75**, 81–94.
72. H. Kiuchi, T. Kondo, M. Sakurai, D. Guo, J. Nakamura, H. Niwa, J. Miyawaki, M. Kawai, M. Oshimada and Y. Harada, *Phys. Chem. Chem. Phys.*, 2016, **18**, 458–465.
73. J. R. Pels, F. Kapteijn, J. A. Moulijn, Q. Zhu and K. M. Thomas, *Carbon*, 1995, **33**, 1641–1653.
74. K. Artyushkova, A. Serov, S. Rojas-Carbonell and P. Atanassov, *J. Phys. Chem. C*, 2015, **119**, 25917–25928.
75. A. Serov, K. Artyushkova and P. Atanassov, *Adv. Energy Mater.*, 2014, **4**, 1301735 (1–7).
76. M. C. Biesinger, B. P. Payne, A. P. Grosvenor, L. W. M. Lau, A. R. Gerson and R. St. C. Smart, *Appl. Surf. Sci.*, 2011, **257**, 2717–2730.
77. Y.-C. Lin, P.-Y. Teng, C.-H. Yeh, M. Koshino, P.-W. Chiu and K. Suenaga, *Nano Lett.*, 2015, **15**, 7408–7413.
78. U. I. Kramm, I. Abs-Wurmbach, I. Herrmann-Geppert, J. Radnik, S. Fiechter and P. Bogdanoff, *J. Electrochem. Soc.*, 2011, **158**, B69–B78.
79. H. Marsh, D. Crawford and D. W. Taylor, *Carbon*, 1981, **21**, 81–87.
80. O. P. Krivoruchko, N. I. Maksimova, V. I. Zaikovskii and A. N. Salanov, *Carbon*, 2000, **38**, 1075–1082.
81. J. H. Hafner, M. J. Bronikowski, B. R. Azamian, P. Nikolaev, A. G. Rinzler, D. T. Colbert, K. A. Smith and R. E. Smalley, *Chem. Phys. Lett.*, 1998, **296**, 195–202.
82. Z. Yang, Z. Yao, G. Li, G. Fang, H. Nie, Z. Liu, X. Zhou, X. Chen and S. Huang, *ACS Nano*, 2012, **6**, 205–211.
83. Y. Hu, J. O. Jensen, W. Zhang, S. Martin, R. Chenitz, C. Pan, W. Xing, N. J. Bjerrum and Q. Li, *J. Mater. Chem. A*, 2015, **3**, 1752–1760.
84. C. Song and J. Zhang, in *PEM Fuel Cell Electrocatalysts and Catalyst Layers: Fundamentals and Applications*, ed. J. Zhang Springer, London, 2008, pp. 89–134.
85. J. Masa, W. Xia, M. Muhler and W. Schuhmann, *Angew. Chem. Int. Ed.*, 2015, **54**, 10102–10120.
86. U. I. Kramm, I. Herrmann-Geppert, J. Behrends, K. Lips, S. Fiechter and P. Bogdanoff, *J. Am. Chem. Soc.*, 2016, **138**, 635–640.

87. Y.-C. Wang, Y.-J. Lai, L. Song, Z.-Y. Zhou, J.-G. Liu, Q. Wang, X.-D. Yang, C. Chen, W. Shi, Y.-P. Zheng, M. Rauf and S.-G. Sun, *Angew. Chem. Int. Ed.*, 2015, **54**, 9907–9910.
88. M. Rauf, Y.-D. Zhao, Y.-C. Wang, Y.-P. Zheng, C. Chen, X.-D. Yang, Z.-Y. Zhou and S.-G. Sun, *Electrochem. Commun.*, 2016, **73**, 71–74.
89. J. Herranz, F. Jaouen, M. Lefèvre, U. I. Kramm, E. Proietti, J.-P. Dodelet, P. Bogdanoff, S. Fiechter, I. Abs-Wurmbach, P. Bertrand, T. M. Arruda and S. Mukerjee, *J. Phys. Chem. C*, 2011, **115**, 16087–16097.
90. J. A. Varnell, C. M. Tse. Edmund, C. E. Schulz, T. T. Fister, R. T. Haasch, J. Timoshenko, A. I. Frenkel and A. Gewirth, *Nat. Commun.*, 2016, **7**, 12582.
91. C. H. Choi, W. S. Choi, O. Kasian, Anna K. Mechler, M.-T. Sougrati, S. Brgller, K. Strickland, Q. Jia, S. Mukerjee, Karl J. J. Mayrhofer and F. Jaouen, *Angew. Chem. Int. Ed.*, 2017, **56**, 8809–8812.
92. H. Kim, K. Lee, S. I. Woo and Y. Jung, *Phys. Chem. Chem. Phys.*, 2011, **13**, 17505–17510.
93. W.-J. Jiang, L. Gu, L. Li, Y. Zhang, X.; Zhang, L.-J. Zhang, J.-Q. Wang, J.-S. Hu, Z. Wei and L.-J. Wan, *J. Am. Chem. Soc.*, 2016, **138**, 3570–3578.
94. D. Guo, R. Shibuya, C. Akiba, S. Saji, T. Kondo and J. Nakamura, *Science*, 2016, **351**, 361–365.
95. H. Meng, F. Jaouen, E. Proietti, M. Lefèvre and J.-P. Dodelet, *Electrochem. Commun.*, 2009, **11**, 1986–1989.
96. T.-N. Tran, M. Y. Song, K. P. Singh, D.-S. Yang and J.-S. Yu, *J. Mater. Chem. A*, 2016, **4**, 8645–8657.
97. N. R. Sahraie, J. P. Paraknowitsch, C. Göbel, A. Thomas and P. Strasser, *J. Am. Chem. Soc.*, 2014, **136**, 14486–14497.
98. J.-Y. Choi, L. Yang, T. Kishimoto, X. Fu, S. Ye, Z. Chen and D. Banham, *Energy Environ. Sci.*, 2017, **10**, 296–305.

## APPENDIX-A: SUPPLEMENTARY DATA

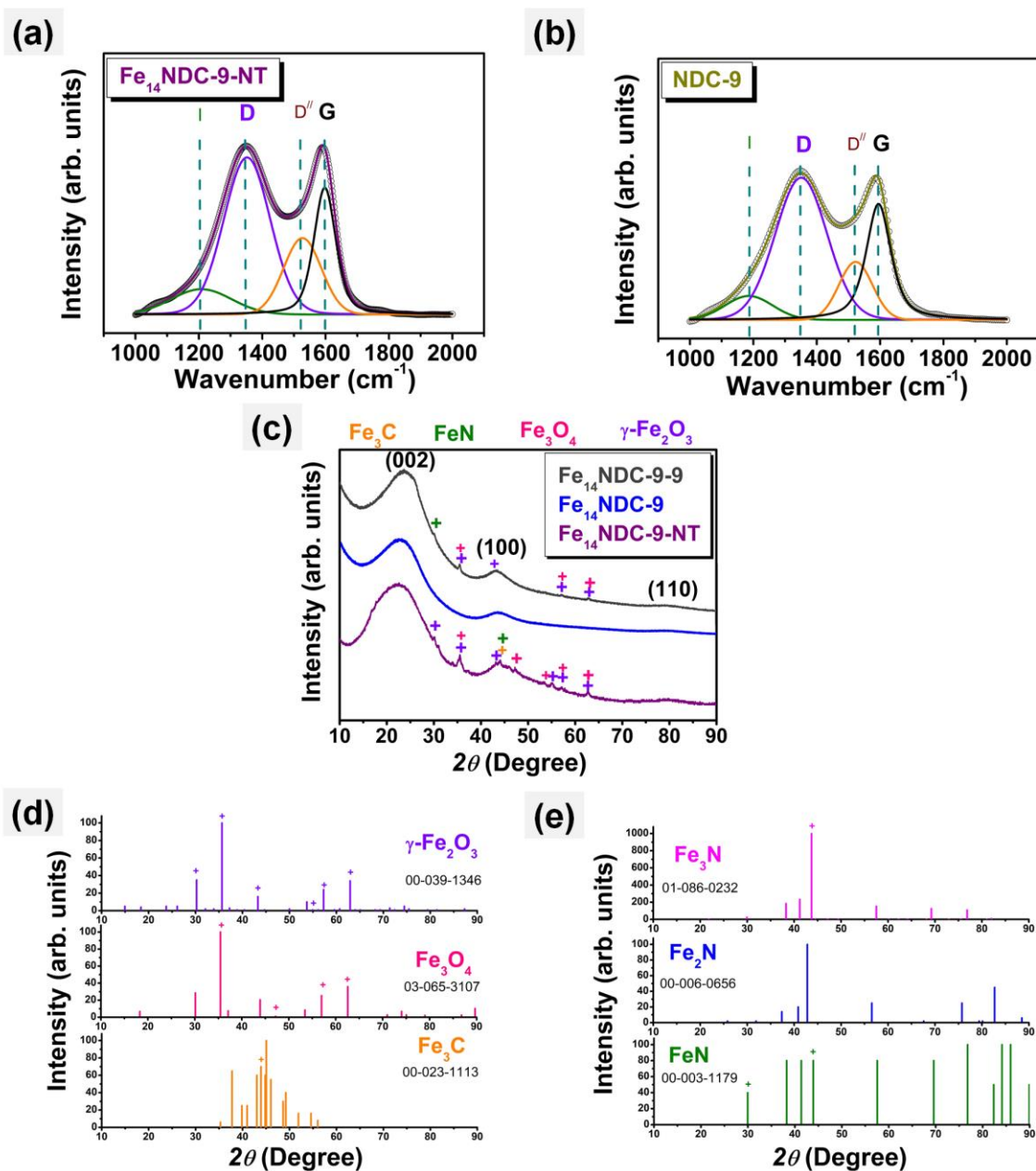


Fig. A 0.1. (a,b) Raman spectra, (c) XRD, and (d,e) Reference XRD pattern.

### ✧ Illustration for the assignment of Raman bands and XRD peaks:

Raw Raman spectra were fitted with four bands primarily located at around 1200, 1350, 1530 and 1600  $\text{cm}^{-1}$ , denoted as I, D, D' and G, respectively for  $\text{Fe}_{14}\text{NDC-9-NT}$  and  $\text{NDC-9}$  as shown in **Fig. A 2.1 a-b**.<sup>1-2</sup> In the case of 1st-order Raman spectra, I-band corresponds to the disordered graphitic carbon in which Gaussian shape means heterogeneous distribution of dopants. D-band generally accepted as the Raman inactive mode (e.g.,  $A_{1g}$ ) originating from the breathing modes of six-atom rings and requires a defect for its activation. D'-band is an indicator of defects in graphene layer stacking. G-band has four vibrational modes in which two of them are Raman vibrational

bands, one is Raman inactive ( $E_{1u}$ ), and other is active expressed as the  $E_{2g}$  mode stemming from the symmetric vibration of  $sp^2$  carbons.<sup>3-4</sup>

				Fe <sub>14</sub> NDC-9		
	Isomer shift, IS (mm s <sup>-1</sup> )	Quadrupole shift, QS (mm s <sup>-1</sup> )	Full-width half maxima, FWHM (mm s <sup>-1</sup> )	Structure	References	
Doublet D1	1, 0.38	1.16	0.62	Fe <sup>II</sup> N <sub>4</sub> /C, LS or Fe <sup>III</sup> N <sub>4</sub> /C, HS	9-16	
Doublet D2	2, 0.45	2.65	0.61	Fe <sup>II</sup> N <sub>2+2</sub> /C, MS	7, 9, 17-18	
Doublet D3	3, 0.54	0.30	0.28	Fe <sub>x</sub> N	19-23	
Singlet 1, S1	0.36	--	3.30	Disordered Fe <sub>x</sub> N <sub>y</sub>	23	
Singlet 2, S2	0.14	--	0.42	Fe/Fe <sub>x</sub> C	24	

Table A 0.1. Mossbauer peak parameters for Fe<sub>14</sub>NDC-9.

✧ **Illustration for the assignment of the peaks in the Mössbauer spectrum:**

In the transmission Mössbauer spectrum of Fe<sub>14</sub>NDC-9, a broad single line response with three doublets and two singlets was obtained indicating the presence various types of iron derived species in the carbon. Three doublets have been assigned to Fe<sup>x</sup>N<sub>4</sub>-C like centers with different electronic states due to changes in their coordination environment and/or different oxidation states (x).<sup>6-7</sup>

**D1:** This doublet feature usually corresponds to Fe<sup>II</sup>N<sub>4</sub>/C, LS, which is well documented in the wide range of heat treated pyrolyzed macrocycles and Fe/N/C catalysts synthesized from individual Fe, N, and C precursors in carbon support.

In this site, the ORR activity is dependent on the electron density on the iron centers.<sup>8</sup> From the seminal work of Lefevre et. al.<sup>9</sup> we understood that irrespective of the ligand type, basic structural motif that comprise FeN<sub>x</sub>C centre has nitrogen atoms of the phenanthroline type complexing the iron ion which itself is a part of the graphene layer at the Basal plane or edge site. In our case, we have used 1,10-phenanthroline which is in co-ordination with the iron cation. So, we assigned the Fe<sup>II</sup>N<sub>4</sub>/C, LS (out of plane) as of Fe-ion connected by four pyridinic N-groups, part of carbon structure in the top of graphene layer of a carbon crystallite. It is worth mentioning that the low spin Fe<sup>II</sup>N<sub>4</sub>/C, LS moiety is indistinguishable from the high-spin Fe<sup>III</sup>N<sub>4</sub>/C moiety only based on Mössbauer analysis owing to their comparable Mössbauer parameters, such as- isomer shift (IS) and quadrupole splitting (QS).<sup>10</sup> On the contrary, D1 could be to a six-coordinate Fe<sup>III</sup> compound.<sup>11-12</sup> However, due to coordination saturation Fe<sup>III</sup> compound is not accessible by oxygen molecules and not been reported yet.<sup>13</sup> Also, it has been mentioned that Fe<sup>II</sup>N<sub>4</sub>/C, LS (out of plane) could undergo structural switching into Fe<sup>III</sup>N<sub>4</sub>/C, HS (in plane) when the catalyst is in contact with the electrolyte.<sup>14-16</sup> Due to the lack of other experimental evidence like- *in-situ* XANES, we are unable to support this conjecture.

**D2:** From the pyrolyzed macrocycles, it has been shown that irrespective of the ligand type the basic structural unit constitute the active part is FeN<sub>2</sub>C<sub>4</sub> at the edge of the graphene layer of the carbon support as the two-adjacent nitrogen of the phenanthroline

type complexing the Fe ion.<sup>9</sup> Both N-groups in the 1,10 phenanthroline structure are of the pyridinic-type (i.e., a N atom contributing to the  $\pi$  band with one electron). Two neighbouring FeN<sub>2</sub>C<sub>4</sub> segment in graphene layer bridged together to comprise FeN<sub>2+2</sub>C<sub>8</sub> structure and thus developing a micropore in the carbon.<sup>17-18</sup> Furthermore, hierarchical mesoporous structure of iron doped carbons allows the diffusion of oxygen to the catalytic site which is usually hidden inside the catalyst architecture in the case of non-porous structure.<sup>7</sup>

**D3:** The assignment of this doublet was difficult. Based on the IS and QS, the peak was assigned as nitrogen rich Fe<sub>x</sub>N,  $x < 2.1$  owing to the IS reported previously.<sup>19-22</sup> But, generally such species are developed during nitrification of carbons by NH<sub>3</sub>.<sup>23</sup> On top of that, the phase of such species was not conclusive via XRD (**Fig. S1** d-f) which has already been discussed earlier.

**Singlet, S1:** This singlet corresponds to disordered FeN<sub>x</sub>C<sub>y</sub>.<sup>23</sup>

**Singlet, S2:** Presence of iron with minor carbide phase, Fe/Fe<sub>3</sub>C could be assigned to S2.<sup>24</sup>

Sample/Peaks	N-py (eV)	N <sub>x</sub> -Fe (eV)	N-Pyr (eV)	N-g (valley) (eV)	N-g (centre) (eV)	N-ox (eV)
Fe <sub>14</sub> NDC-6	398.57	-	400.10	-	-	-
Fe <sub>14</sub> NDC-8	398.55	399.45	400.25	401.20	402.20	404.10
Fe <sub>14</sub> NDC-9	398.54	399.80	400.70	401.40	402.50	403.40
Fe <sub>14</sub> NDC-10	398.90	400.10	400.82	401.60	402.83	403.92
NDC-9	398.41		399.70	400.60	401.40	403.20
Fe <sub>3.5</sub> NDC-9	398.45	399.80	400.60	401.40	402.40	403.80
Fe <sub>7</sub> NDC-9	398.50	399.70	400.60	401.40	402.60	403.90
Fe <sub>28</sub> NDC-9	398.50	399.95	400.80	401.50	402.70	403.50
Fe <sub>14</sub> NDC-9-W <sub>2M</sub> -9	398.48	399.75	-	401.00	402.00	403.20

Table A 0.2. List of XPS binding energy peak of different bonding configurations of nitrogen in doped carbons.

Sample Name	Atomic concentration (at%)						
	N	N-py	N-pyr	N <sub>x</sub> -Fe	N-g (valley)	N-g (centre)	N-ox
Fe <sub>14</sub> NDC-6	12.77	68.0	32.0	-	-	-	-
Fe <sub>14</sub> NDC-8	9.18	38.4	32.5	7.2	18.5	1.6	1.8
Fe <sub>14</sub> NDC-9	5.31	27.1	29.5	17.2	19.3	4.7	2.2
Fe <sub>14</sub> NDC-10	4.05	26.1	23.0	17.3	28.2	3.9	1.5
NDC-9	7.87	37.3	15.9	-	26.1	18.2	2.5
Fe <sub>3.5</sub> NDC-9	7.70	33.4	26.6	18.1	16.1	2.9	2.9
Fe <sub>7</sub> NDC-9	6.95	29.9	27.0	18.3	18.2	3.6	3.0

<b>Fe<sub>28</sub>NDC-9</b>	5.26	28.2	31.6	21.7	13.5	3.2	1.8
<b>Fe<sub>14</sub>NDC-9- W<sub>2M</sub>-9</b>	2.78	23.0	-	12.0	51.0	9.0	5.0

Table A 0.3. Atomic concentration for nitrogen and its different configurations.

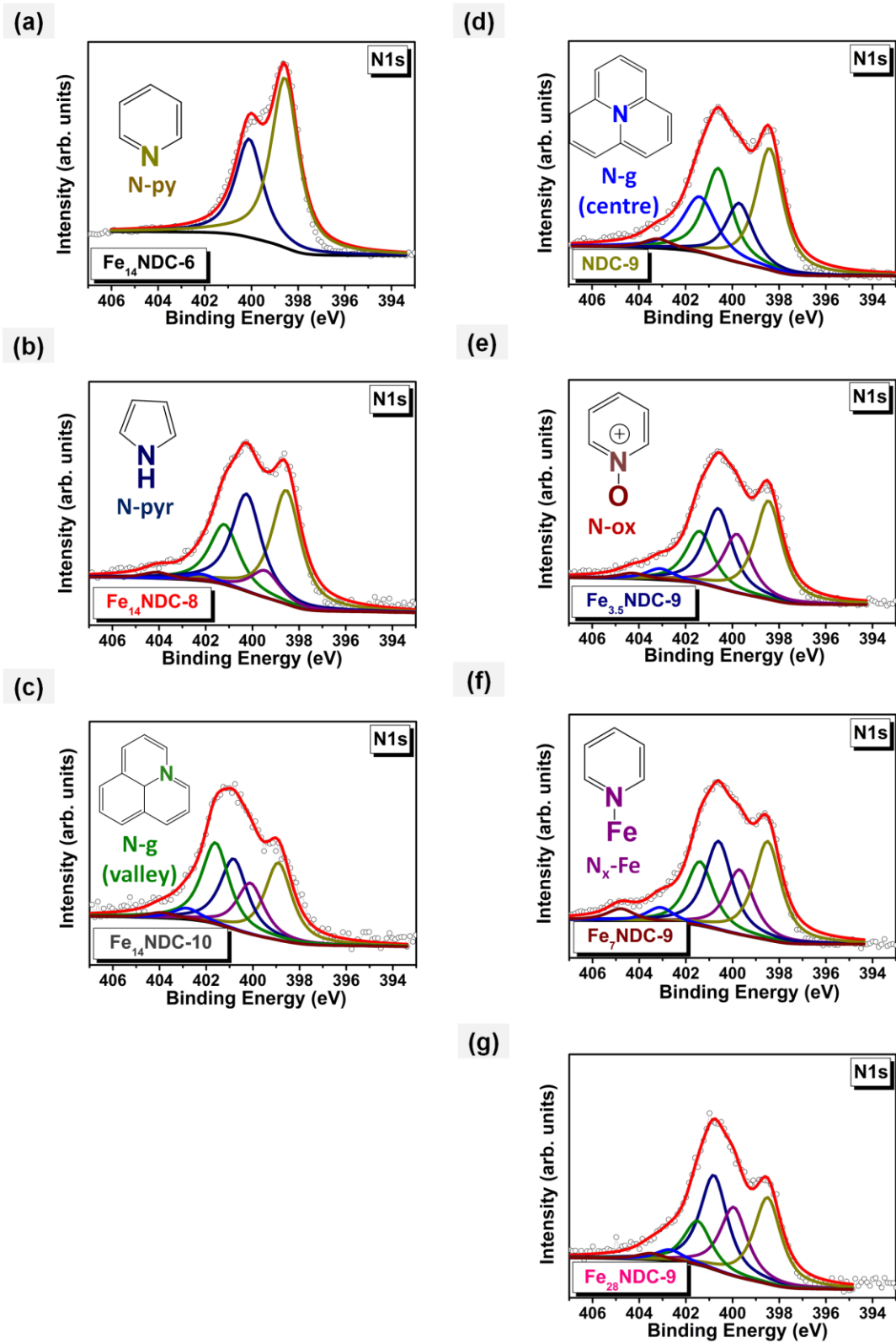


Fig. A 0.2. N1s HR-XPS spectra of doped carbons.

Catalyst and loading ( $\mu\text{g cm}^{-2}$ )	Precursors and conditions	Half-wave potential, $E_{1/2}$ (V) / Mass activity ( $\text{A g}^{-1}$ )	Electrolyte	Reference
<b>Fe-Phen @MOF-ArNH<sub>3</sub> 600</b>	Fe (oAc) <sub>2</sub> + Phen + MOF-Ar-1050-NH <sub>3</sub> -950	0.86 V (vs RHE)	0.1 M KOH	S5
		0.77 V (vs RHE)	0.1 M HClO <sub>4</sub>	
<b>BP-Ph-Fe-Ar-NH<sub>3</sub> 800</b>	Black pearls + Phen + Fe (oAc) <sub>2</sub> -Ar-1050-NH <sub>3</sub> -950	0.72 V (vs RHE)	0.5 M H <sub>2</sub> SO <sub>4</sub>	S29
<b>FePPyPhen/C</b>	FeCl <sub>3</sub> + pyrrole-COOH + Phen-NH <sub>2</sub>	0.29 V (vs RHE)	0.1 M PBS	S30
<b>NC-800</b>	Fe (oAc) <sub>2</sub> + Phen-Ar-900	2.37 A g <sup>-1</sup> @ 0.7 V (vs RHE)	0.5 M H <sub>2</sub> SO <sub>4</sub> @ 35 °C	S31
<b>1.14%Fe/BP-Phen</b>	Black pearls + Phen + FeSO <sub>4</sub> -Ar-900	0.65 V (vs RHE)	0.5 M H <sub>2</sub> SO <sub>4</sub>	S32
<b>Fe<sub>2</sub>-Phen/V 354</b>	Vulcan XC72 + Fe-Phen complex-NH <sub>3</sub> -800	3.44 A g <sup>-1</sup> (vs RHE)	0.5 M H <sub>2</sub> SO <sub>4</sub>	S33
<b>BP-N-Fe 400</b>	Carbon black + melamine + FeCl <sub>3</sub> -Ar-900	0.92 V (vs SCE)	0.1 M KOH	S34
<b>S/N_Fe27 800</b>	Carbon black + FeCl <sub>3</sub> + Aprotic ionic liquid-900-2 M H <sub>2</sub> SO <sub>4</sub> -900	0.87 V (vs RHE)	0.1 M KOH	S35
<b>IL-1-C 283</b>	[MIm] [FeBrCl <sub>3</sub> ]-N <sub>2</sub> -750-37 wt% HCl	124.0 A g <sup>-1</sup> @ -0.3 V (vs Ag/AgCl)	0.1 M KOH	S36
<b>Fe<sup>10</sup>@NOMC</b>	[FeN] [NTf <sub>2</sub> ] + [MCNIm] [N(CN) <sub>2</sub> ] + SBA-15	-0.05 V (vs Hg/HgO)	0.1 M NaOH	S37

Table A 0.4. ORR performance comparison between current study and earlier reports.

Sample abbreviation	Dopants content (at%)					Surface area S <sub>BET</sub> (m <sup>2</sup> g <sup>-1</sup> )	TPV <sub>p/po = 0.99</sub> (cm <sup>3</sup> g <sup>-1</sup> )
	C	N	Fe	S	O		
<b>Fe<sub>14</sub>NDC-6</b>	76.13	12.77	0.31	1.37	9.42	567.58	1.21
<b>Fe<sub>14</sub>NDC-8</b>	81.68	9.18	0.25	1.18	7.87	937.87	1.66
<b>Fe<sub>14</sub>NDC-9</b>	85.81	5.31	0.28	1.01	7.59	959.36	2.05
<b>Fe<sub>14</sub>NDC-10</b>	89.87	4.05	0.19	1.27	4.63	986.77	2.25
<b>NDC-9</b>	85.05	7.87	-	1.20	5.87	658.41	1.10
<b>Fe<sub>3.5</sub>NDC-9</b>	85.91	7.70	0.21	0.64	5.62	853.36	1.54
<b>Fe<sub>7</sub>NDC-9</b>	85.45	6.95	0.23	0.97	6.98	857.32	1.66
<b>Fe<sub>28</sub>NDC-9</b>	86.79	4.88	0.29	0.65	7.39	935.21	1.95
<b>Fe<sub>14</sub>NDC-9-W<sub>2</sub>M-9</b>	92.61	2.78	0.17	0.86	3.55	Not determined	
<b>Fe<sub>14</sub>NDC-9-NT</b>						20.05	0.01
<b>Fe<sub>14</sub>NDC-9-9</b>	92.64	4.33	0.21	0.80	2.02	Not determined	

Table A 0.5. Atomic concentrations of the elements determined from XPS survey spectra, specific surface areas and total pore volumes estimate from the adsorption-desorption isotherms via BET analysis method.

## APPENDIX-B: REFERENCES

- A1 D. W. Marquadt, *J. Soc. Ind. Appl. Math.*, 1963, **11**, 431–441.
- A2 A. Cuesta, P. Dhamelincourt, J. Laureyns, A. Martinezalonso and J. M. D Tascon, *Carbon*, 1994, **32**, 1523–1532.
- A3 S. Maldonado, S. Morin and K. J. Stevenson, *Carbon*, 2006, **44**, 1429–1437.
- A4 S. Zhang, M. S. Miran, A. Ikoma, K. Dokko and M. Watanabe, *J. Am. Chem. Soc.*, 2014, **136**, 1690–1693.
- A5 K. Strickland, E. Miner, Q. Jia, U. Tylus, N. Ramaswamy, W. Liang, M.-T. Sougrati, F. Jaouen and S. Mukerjee, *Nat. Commun.*, 2015, **6**, 7343 (1–8).
- A6 P. Gülich, E. Bill and A. X. Trautwein, in *Mössbauer Spectroscopy and Transition Metal Chemistry: Fundamentals and Transition Metal Chemistry*, Springer, Heidelberg, 2011.
- A7 U. I. Kramm, M. Lefèvre, N. Larouche, D. Schmeisser and J.-P. Dodelet, *J. Am. Chem. Soc.*, 2014, **136**, 978–985.
- A8 U. I. Kramm, I. Abs-Wurmbach, I. Herrmann-Geppert, J. Radnik, S. Fiechter and P. Bogdanoff, *J. Electrochem. Soc.*, 2011, **158**, B69–B78.
- A9 M. Lefèvre, J.-P. Dodelet and P. Bertrand, *J. Phys. Chem. B*, 2000, **104**, 11238–11247.
- A10 F. Jaouen, in *Non-Noble Metal Fuel Cell Catalysts*, ed. Z. Chen, J.-P. Dodelet, J. Zhang, Wiley-VCH Verlag GmbH & Co. KGaA, 2014, p. 29.
- A11 Y. Zhu, B. Zhang, X. Liu, D.-W. Wang and D. S. Su, *Angew. Chem. Int. Ed.*, 2014, **53**, 10673–10677.
- A12 H. Schulenburg, S. Stankov, V. Schünemann, J. Radnik, I. Dorbandt, S. Fiechter, P. Bogdanoff and H. Tributsch, *J. Phys. Chem. B*, 2003, **107**, 9034–9041.
- A13 A. A. Tanaka, C. Fierro, D. Scherson and E. B. Yeager, *J. Phys. Chem.*, 1987, **91**, 3799–3807.
- A14 D. Scherson, A. A. Tanaka, S. L. Gupta, D. Tryk, C. Fierro, R. Holze, E. B. Yeager and R.P. Lattimer, *Electrochim. Acta*, 1986, **31**, 1247–1258.
- A15 Q. Jia, N. Ramaswamy, H. Hafiz, U. Tylus, K. Strickland, G. Wu, B. Barbiellini, A. Bansil, E. F. Holby, P. Zelenay and S. Mukerjee, *ACS Nano*, 2015, **9**, 12496–12505.
- A16 F. Jaouen, M. Lefèvre, J.-P. Dodelet and M. Cai, *J. Phys. Chem. B*, 2006, **110**, 5553–5558.
- A17 J. Li, S. Ghoshal, W. Liang, M.-T. Sougrati, F. Jaouen, B. Halevi, S. McKinney, G. McCool, C. Ma, X. Yuan, Z.-F. Ma, S. Mukerjee and Q. Jia, *Energy Environ. Sci.*, 2016, **9**, 2418–2432.
- A18 Csaba E. Szakacs, M. Lefèvre, U. I. Kramm, J.-P. Dodelet and F. Vidal, *Phys. Chem. Chem. Phys.*, 2014, **16**, 13654–13661.
- A19 D. M. Borsa and D. O. Boerma, *Hyperfine Interact.*, 2003, **151/152**, 31–48.
- A20 P. Schaaf, *Prog. Mater. Sci.*, 2002, **47**, 1–161.
- A21 F. Charreteur, F. Jaouen, S. Ruggeri and J.-P. Dodelet, *Electrochim. Acta*, 2008, **53**, 2925–2938.
- A22 G. M. Chen, N. K. Jaggl, J. B. Butt, E. B. Yeh and L. H. Schwartz', *J. Phys. Chem.*, 1983, **87**, 5326–5332.

- A23 U. I. Kramm, J. Herranz, N. Larouche, Thomas M. Arruda, M. Lefèvre, F. Jaouen, P. Bogdanoff, S. Fiechter, I. Abs-Wurmbach, S. Mukerjee and J.-P. Dodelet, *Phys. Chem. Chem. Phys.*, 2012, **14**, 11673–11688.
- A24 J. A. R. v. veen, H. A. Colijn and J. F. Van Baar, *Electrochim. acta*, 1988, **33**, 801–804.
- A25 J. Casanovas, J. M. Ricart, J. Rubio, F. Illas, and J. M. Jimé'nez-Mateos, *J. Am. Chem. Soc.*, 1996, **118**, 8071– 8076.
- A26 Y. Yamada, J. Kim, S. Matsuo and S. Sato, *Carbon*, 2014, **70**, 59– 74.
- A27 Y. Yamada, Y. Suzuki, H. Yasuda, S. Uchizawa, K. Hirose-Takai, Y. Sato, K. Suenaga and S. Sato. *Carbon*, 2014, **75**, 81– 94.
- A28 H. Kiuchi, T. Kondo, M. Sakurai, D. Guo, J. Nakamura, H. Niwa, J. Miyawaki, M. Kawai, M. Oshimad and Y. Harada, *Phys. Chem. Chem. Phys.*, 2016, **18**, 458– 465.
- A29 K. Mamtani, D. Singh, J. Tian, J.-M. M. Millet, Jeffrey T. Miller, A. C. Co and U. S. Ozkan, *Catal. Lett.*, 2016, **146**, 1749– 1770.
- A30 Y. Lua, X. Wang, M. Wang, L. Kong and J. Zhao, *Electrochim. Acta*, **2015**, 180, 86– 95.
- A31 T. Onodera, T. Mizukami, S. Suzuki, J. Kawaji, K. Yamaga and T. Yamamoto, *Catal. Commun.*, 2014, **43**, 66– 71
- A32 M. Bron, J. Radnik, M. Fieber-Erdmann, P. Bogdanoff and S. Fiechter, *J. Electroanal. Chem.*, 2002, **535**, 113– 119.
- A33 M. Bron, S. Fiechter, M. Hilgendorff and P. Bogdanoff, *J. Appl. Electrochem.* 2002, **32**, 211–216.
- A34 J. Liu, X. Sun, P. Song, Y. Zhang, W. Xing and W. Xu, *Adv. Mater.*, 2013, **25**, 6879– 6883.
- A35 N. R. Sahraie, J. P. Paraknowitsch, C. Göbel, A. Thomas, and P. Strasser, *J. Am. Chem. Soc.*, 2014, **136**, 14486–14497.
- A36 F. He, X. Chen, Y. Shen, Y. Li, A. Liu, S. Liu, T. Moric and Y. Zhang, *J. Mater. Chem. A*, 2016, **4**, 6630–6638.
- A37 Z. Li, G. Li, L. Jiang, J. Li, G. Sun, C. Xia and F. Li, *Angew. Chem. Int. Ed.*, 2015, **54**, 1494– 1498.
- A38 J. A. Bautista-Martinez, L. Tang, J.-P. Belieres, R. Zeller, C. A. Angell and C. Friesen, *J. Phys. Chem. C*, 2009, **113**, 12586–12593.

## CHAPTER 3 PROTIC SALTS AND PROTIC IONIC LIQUIDS DERIVED ELECTROACTIVE MATERIALS

### *Promising oxygen electroreduction performance of iron doped mesoporous carbons in tertiary alkylamine-PILs*

#### 3.1. Introduction

It is undeniable that global climate change is the most difficult challenge we are facing at present which has upsurge the interest in wide variety of clean and sustainable energy resources to reduce the burden on the depleting natural and fossil fuels. In such realm, there has been a boom in the research of energy conversion and storage electrochemical devices, such as batteries and fuel cells (FCs). FCs can convert hydrogen (fuel) into electricity via reacting with oxygen and producing water as the only product, a promising prospect nonetheless for the automotive sectors and stationary power sources. Amongst the broad classes of FCs, proton exchange membrane fuel cells (PEMFCs) has attracted much attention for fuel cells electric vehicles (FCEVs) due to its high-power density. Despite the initial promises, there are several technical challenges which needs to be met before we realize the highly efficient FCEVs for mass market. For conventional PEMFCs, in which humidification is quintessential as the membrane, that is Nafion must be always hydrated which is also a limitation in that the operating temperature cannot be exceeded 80 °C. Also, water management is problematic too for the engineers. In that perspective, non-aqueous proton conducting electrolyte has been explored so that PEMFCs could run well above 80 °C, such as between 120 °C to 150 °C. Increase of the reaction temperature not only enhance the reaction kinetics, in particularly the sluggish reduction reaction of oxygen at the cathode but also eradicate the water management issue. Protic ionic liquids (PILs), a subgroup of ionic liquids (ILs) synthesize via Bronsted acid-base reaction at certain stoichiometry having an active/exchangeable proton in their structure reported to be a promising candidate for mesothermal FCs. Since the early report of Susan and Angell, Nakamoto reported the outstanding electrochemical activity of PILs, that is, diethylmethylammonium triflate, [Dema][TFO] using Pt as cathode at 150 °C. Later, Lee demonstrated the feasibility of such PILs in the PEMFCs using SPI membrane under non-humidified conditions. On the contrary, to speed up the oxygen reduction kinetics Pt and its alloy has been utilized as electrocatalyst. Erlebacher's group pioneered the use of hydrophobic PILs ([MTBD][TFSA]) to boost the activity nanoporous Pt-Ni alloy oxygen reduction catalyst. After that, Etzold and others also demonstrated the boosting effect of PILs on commercial Pt/C in acidic media. No report has been found so far regarding such enhancing effect of PILs for non-precious metal catalyst. Owing to the high cost and rarity of precious metals, tremendous effort has been done to explore low cost, abundant, and efficient non-precious metal based catalyst. Iron ticks all the boxes to be useful for the development of catalyst of such variety. And, especially for acidic and alkaline PEMFCs, several promising catalysts have been reported. For that the general approach is mixing iron salt with a carbonaceous precursor (molecular/polymer) or molecular complex/macrocyclic complex of iron first and the subsequent carbonization at high temperature under Ar/NH<sub>3</sub>. Depending on the synthetic strategy different classes of iron doped carbons are prepared such as Fe/N/C or Fe@carbon shell core@shell catalysts. Apart from popular polymeric carbon precursors, ionic liquids have also been deployed as the new generation of precursors owing to its carbon rich nature and high thermal stability whereas most molecular solvents are evaporated at high temperature pyrolysis and polymers take multistep pre- and post-treatment steps. Protic ionic liquids/salts (PILs/PSs) have recently reported to be even more simpler, quicker and cost effective than conventional aprotic ionic liquids (AILs) by keeping the robust molecular designability of ILs platform. Simply combining PSs and iron salt, efficient Fe/N/C oxygen reduction catalyst has been reported recently in alkaline and acidic media. But, Fe-doped carbons (FeNDCs) have been explored in non-aqueous electrolyte media such as PILs.

In this study, to strike the synergy of non-aqueous electrolyte and non-precious metal catalyst, FeNDCs is employed to reduce the oxygen efficiently in [Dema][TFO]-PILs. Via hydrodynamic voltammetry, this study demonstrates that oxygen reduction reaction occurs exclusively via 4e<sup>-</sup> reduction pathway via FeNDCs in [Dema][TFO] with the onset potential of 0.864 V at 120 °C. Also, via hydrodynamic chronoamperometry with a rugged protocol, FeNDCs also displayed promising stability. Overall, this study opens a new avenue in the research of PEMFCs, and surely motivate the not only FCs purist but

also the material scientists in general to expand the horizon of novel combination of materials for energy applications.

### 3.2. Experimental Details

**Preparation of Electrocatalyst and Electrolyte.** Protic ionic liquids, that is [Dema][TFO] and salts, that is [Phen][HSO<sub>4</sub>]<sub>2</sub> were synthesized by following the previous procedures. [] Also, the prototype N, and S codoped catalyst (NDC-9) and Fe, N, and S codoped catalyst (Fe<sub>1.4</sub>NDC-9) were prepared per to the earlier report by Hoque et. al. []

**Electrochemical Cell Construction.** Electrochemical characterization was carried out in a three electrodes cell. GC/Pt (4mm/7mm) (BAS, Japan), graphite rod (BAS, Japan), and self-contained RHE (Gaskatel, Germany) were used as the working, counter, and reference electrodes respectively. A small amount of [Dema][TFO] was employed as the electrolyte in the U-shape 15.0 mL glass cell (AS ONE, Japan) with a Teflon cap (BAS, Japan) tightly wrapped by Teflon tape. Temperature was controlled between 80 °C and 120 °C via a constant temperature oil bath (NISSIN NWB.120N, Japan) with an accuracy of ± 0.5 to 1° C (when stirring). Oil bath was put on top of a high temperature resistant magnetic stirrer to constantly stir the oil to maintain uniform temperature at the cell surface covered by the hot oil in which temperature was monitored via a digital thermocouple. Gas flow of Ar (g), and O<sub>2</sub> (g) were controlled by a flow meter (Kofloc, Japan).

**Electrode Preparation.** Briefly, for iron doped carbons, catalyst ink (0.155 mg mL<sup>-1</sup>) was prepared by adding 2.00 mg of catalyst to a 0.310 mL mixture of deionized water (0.150 mL), iso-propanol (0.140 mL), and Nafion as an ionomer (0.020 mL, 5.0 wt%; Sigma-Aldrich, Nafion 117). Then, the mixture was ultrasonicated enough to make a well-dispersed ink, and finally dropped (10.0 μL) into a mirror polished GC surface of Pt/GC electrode by using a micropipette (Eppendorf, Japan). Then, the electrode was rotated at 300 rpm for 2 hours at room temperature for a smooth coating of the catalyst materials over the GC surface. Then, to ensure the removal of the solvents it was kept at room temperature at 0 rpm. Before casting the catalyst ink, the GC electrode surface was purged with Ar to remove any surface moisture.

**Electrocatalytic activity and stability test.** The modified RRDE was activated first by cycling the potential from +1.10 V to 0.10 V at a scan rate of 50 mV s<sup>-1</sup> for 50 cycles in Ar-saturated [Dema][TFO]. During RRDE voltammograms at a scan rate of 3 mV s<sup>-1</sup>, the ring potential of the RRDE was held constant at +0.3 V against the RHE. After scanning the potential three times without any rotation (0 rpm), the RRDE voltammogram was acquired at 400 rpm. For kinetic analysis, the rotation speed was varied from 200 to 1050 rpm. The displayed current density and potential in LSVs for all the samples were background and *i*R corrected. In all cases, to evaluate the catalytic activity, the onset potential was determined from the LSV curves at 0.1 mA cm<sup>-2</sup>.

To construct Tafel plots, the kinetic current (*J<sub>k</sub>*) was calculated from the mass-transport correction of the RDE voltammograms using the following equation:

$$J_k = \frac{J_D J}{J_D - J} \quad (\text{Eq. 3.1})$$

where *J<sub>k</sub>* is the kinetic current density, *J* is the measured current density, and *J<sub>D</sub>* is the diffusion-limiting current density.

Detailed analysis of the kinetics of the ORR was carried out using the Koutecky-Levich (K-L) equations (**Eqs. (3.3) -(3.5)**).

$$\frac{1}{J} = \frac{1}{B\omega^{1/2}} + \frac{1}{J_k} \quad (\text{Eq. 3.2})$$

where *J* is the measured current density, *J<sub>k</sub>* is the kinetic current density,  $\omega$  is the angular velocity of the disk ( $\omega = 2\pi N$ , *N* is the linear rotation speed), and *B* is the Levich slope, which is given by:

$$B = 0.201nFC_0D_0^{2/3}\nu^{-1/6} \quad (\text{Eq. 3.3})$$

where  $n$  is the overall number of electrons transferred during oxygen reduction,  $F$  is the Faraday constant ( $F = 96485 \text{ C mol}^{-1}$ ),  $C_0$  is the bulk concentration of  $\text{O}_2$  ( $C_0 = \text{mol cm}^{-3}$ ),  $D_0$  is the diffusion coefficient of  $\text{O}_2$  ( $D_0 = 1.9 \times 10^{-5} \text{ cm}^2 \text{ s}^{-1}$ ), and  $\nu$  is the kinematic viscosity of ( $\nu = \text{cm}^2 \text{ s}^{-1}$ ). □

$$\frac{1}{J_k} = \frac{1}{nFkC_0} \quad (\text{Eq.3.4})$$

**Eq. (3.5)** is the intercept of **Eq. (3.3)** and  $k$  is the electron transfer rate constant. Per Eqs. (3) and (2),  $n$  and  $J_k$  could be estimated from the slope and the intercept of the K-L plot, respectively. From Eq. (4), using the obtained values of  $n$  and  $J_k$ , the heterogeneous rate constant for electron transfer ( $k$ ) could be calculated.

The mass activity,  $J_m$  ( $\text{A g}^{-1}$ ) of the catalyst in [Dema][TFO] was calculated using the following equation:

$$J_m = \frac{J_k(0.75 \text{ V vs RHE})}{L_{\text{cat}}} \quad (\text{Eq. 3.5})$$

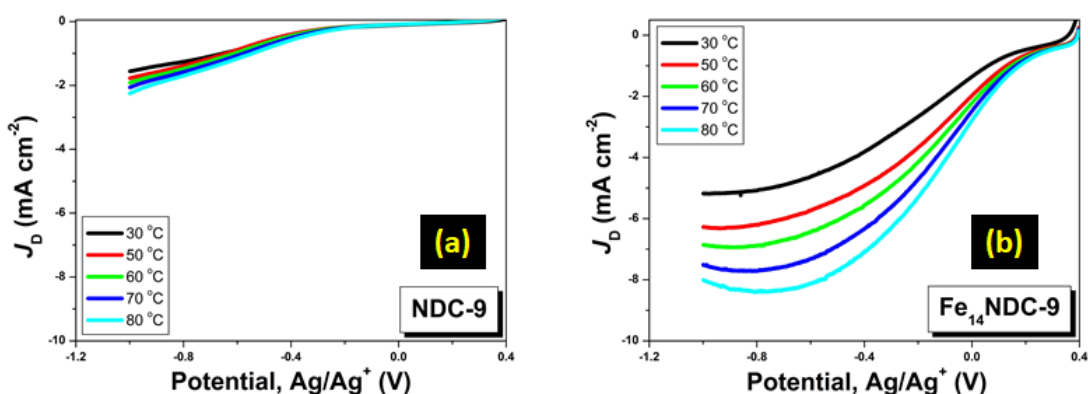
where  $J_k$  ( $\text{mA cm}^{-2}$ ) is the kinetic current density at 0.75 V vs reversible hydrogen electrode (RHE) calculated by the **Eq. (3.5)** and  $L_{\text{cat}}$  ( $\mu\text{g cm}^{-2}$ ) is the amount of catalyst loaded on the GC surface of the RRDE.

$$J_k = \frac{J_k(0.75 \text{ V vs RHE}) * J_{\text{Lim}}}{J_{\text{Lim}} - J_k(0.75 \text{ V vs RHE})} \quad (\text{Eq. 3.6})$$

where  $J_{\text{Lim}}$  ( $\text{mA cm}^{-2}$ ) is diffusion-limited current density in the  $\text{O}_2$ -saturated electrolyte after background correction.

Hydrodynamic chronoamperometry experiments were conducted in an  $\text{O}_2$ -saturated environment at 400 rpm. To compare the inherent kinetic activity of the catalysts, LSV measurements were obtained before and after the chronoamperometry measurements under the same experimental conditions.

### 3.3. Results and Discussion



Linear sweep voltammograms of ORR in  $\text{O}_2$ -saturated PILs, [Dema][TFO] using doped carbons synthesized using PS, [Phen][2HSO<sub>4</sub>] at different temperatures. Scan rate:  $10 \text{ mV s}^{-1}$ . Catalyst loading:  $500 \mu\text{g cm}^{-2}$ .

3.4. Concluding Remarks

3.5. References

(Electrochemical analysis regarding to this chapter is in progress)

## CHAPTER 4 PROTIC IONIC LIQUIDS DERIVED ELECTROLYTE

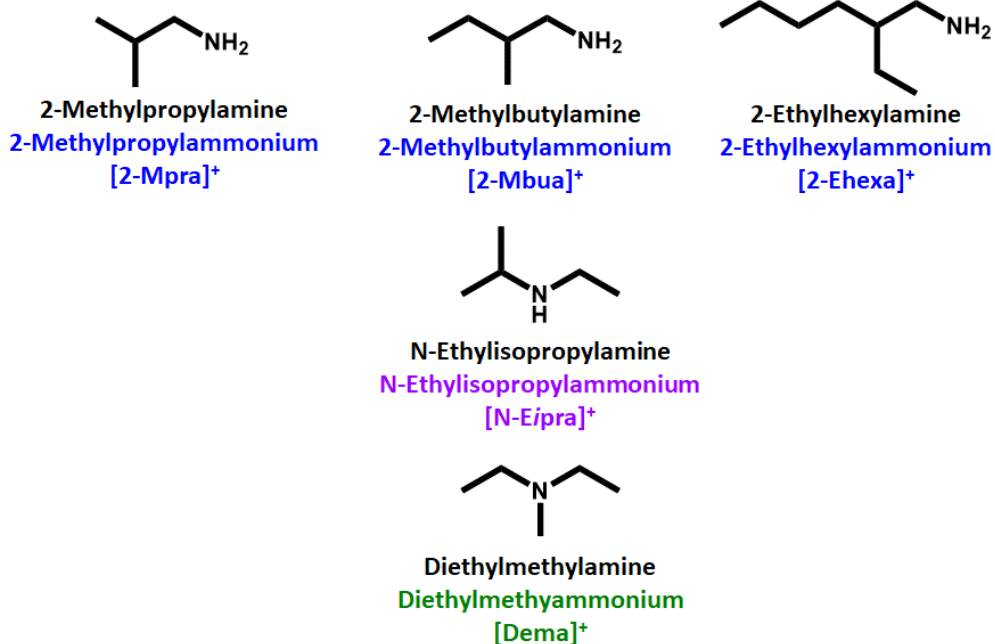
### ***Protic ionic liquids based on primary alkyl amine: Structure-property correlations and understanding their unique properties based on Hydrogen-bonding***

#### 4.1. Introduction

Ionic liquids (ILs) are defined as liquids comprised solely of ions (at the temperature of interest)<sup>1</sup>, and research study has evolved to incorporate several classes such as aprotic ionic liquids (AILs), protic ionic liquids (PILs), solvate ionic liquids (SILs) and related categories such as salt-in-solvent systems and mixtures etc.<sup>1-2</sup> Every variant of ILs has merits and shortcomings; their usefulness/functionality is dictated by their tunable fundamental properties.<sup>2-3</sup> In this robust branch of liquid chemistry, PILs are also unique in that they are easily synthesized via a stoichiometric Brønsted acid-base reaction involving proton transfer, in contrast to AILs.<sup>2</sup> The PIL ethylammonium nitrate (EAN),<sup>4</sup> is considered one of the earliest reported room-temperature ILs. Extensive research has been performed to understand its fundamental properties.<sup>5-8</sup> Ludwig *et. al.*<sup>8</sup> demonstrated that EAN forms a dense, co-operative hydrogen (H-) bonding network akin to water. Further study of H-bonding and its effects on the features of PILs beyond the EAN system is attractive. Despite its intriguing properties, EAN suffers from poor thermal stability<sup>9</sup> owing to the relatively low  $\Delta pK_a$ <sup>10-11</sup> and electrochemical instability in EAN-water binary mixtures due to the unstable nature of the anion.<sup>12</sup> However, beyond EAN and related combinations, further research has been hindered by the scarcity of room temperature liquid samples (or even low melting temperature salts).<sup>3</sup> Incorporation of more weakly Lewis-basic anions has opened new opportunities for alkylamine-based PILs, in particular for tertiary amines, and also for secondary amines.<sup>2-3</sup> Owing to the importance of hydrogen bonding networks in PILs (*vide supra*), further study of primary alkylamine-based PILs, with a higher number of potential H-bond donors, is also attractive. Moreover, primary alkylamine-PILs are promising for application in various areas, including, but not limited to: as non-aqueous solvents in molecular self-assembly of macromolecules,<sup>3</sup> as reagents/media in protein chemistry,<sup>13</sup> as precursors of nitrogen doped carbon materials,<sup>14</sup> in tribological applications<sup>15</sup> and in electrochemical devices.<sup>2</sup> Thus, from both a fundamental and applied perspective, primary alkylamine-based PILs with high  $\Delta pK_a$  are an appealing system. However, they are rarely reported in comparison with tertiary alkylamine-PILs owing to the synergy of intermolecular forces<sup>5-6</sup>, such as doubly ionic H-bonds,<sup>9,16</sup> and efficient packing of the ions promoting crystallization at relatively high temperatures comparable to that of molecular liquids such as water.<sup>5,9</sup>

In this article, we report several selected prototype examples of novel primary amine-PILs using branched alkylammonium cations and bis(trifluoromethanesulfonyl) amide ([TfSA]<sup>-</sup>) as anion. Herein, we present the structure-property relationships for the variation in cationic structure of 2-ethylhexylammonium ([2-Ehexa]<sup>+</sup>), 2-methylbutylammonium ([2-Mbua]<sup>+</sup>), and 2-methylpropylammonium ([2-Mpra]<sup>+</sup>) Furthermore, secondary and tertiary isomers of [2-Mbua]<sup>+</sup>, namely N-ethylisopropylammonium ([N-Eipra]<sup>+</sup>), and diethylmethylammonium ([Dema]<sup>+</sup>) were compared. Structures of cations and anions are shown in **Fig. 5.1**.

### Primary, secondary, and tertiary amines/Cations



### Acids/Anions

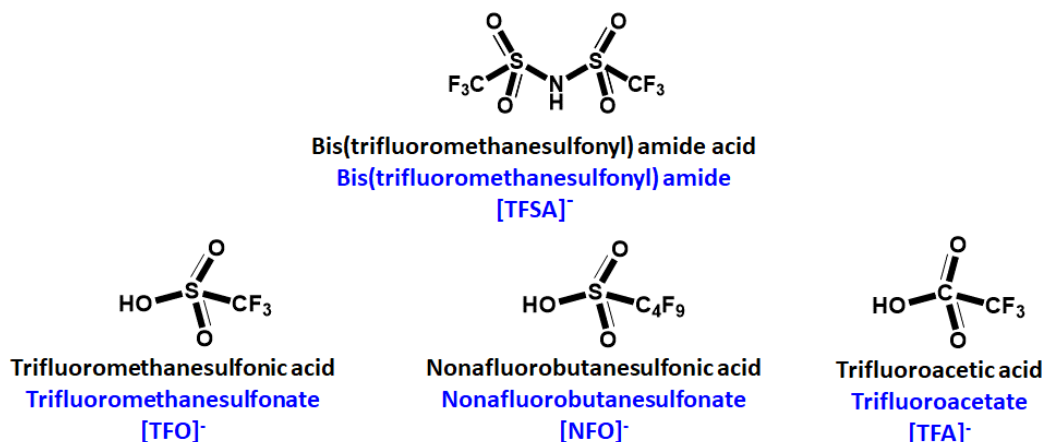


Fig. 4.1. Structure of amines and acids employed in this study.

## 4.2. Experimental Details

### 4.2.1. Synthesis of protic ionic liquids/protic salts

All the amines (TCI, Japan) and acids (Wako Chemicals, Japan), also shown in Scheme S1, were used as received. Prior to the synthesis, reagents were weighed and handled inside a dry box (Daikin, Japan). Glassware was dried in an oven at 80 °C before carrying out the synthesis under an inert atmosphere.

The PILs were synthesized by mixing amine and acid in a 1.05: 1 molar composition in an ice bath to control the heat of the exothermic acid-base reaction (**Fig. 4.2**). The neat amine was added dropwise very slowly (roughly 0.5 mL/h) by a pressure-equalizing dropping funnel (10 mL) to the neat acid (HTFSA) in a two-neck round bottom flask (100 mL) and mixed vigorously via magnetic stirrer (3000 rpm) to suppress the evolution of

the localized heat. During mixing, care must be taken as primary amine-PILs tend to solidify at low temperature; therefore, to ensure homogeneous mixing, the reaction vessel was occasionally taken out of the coolant while stopping the addition of the amine to the mixture and then mixed at room temperature by magnetic stirrer for several minutes. After that, the reaction vessel was put back in the coolant and addition of amine was restarted with the same rate as previous. In this way, colourless PILs was achieved efficiently.

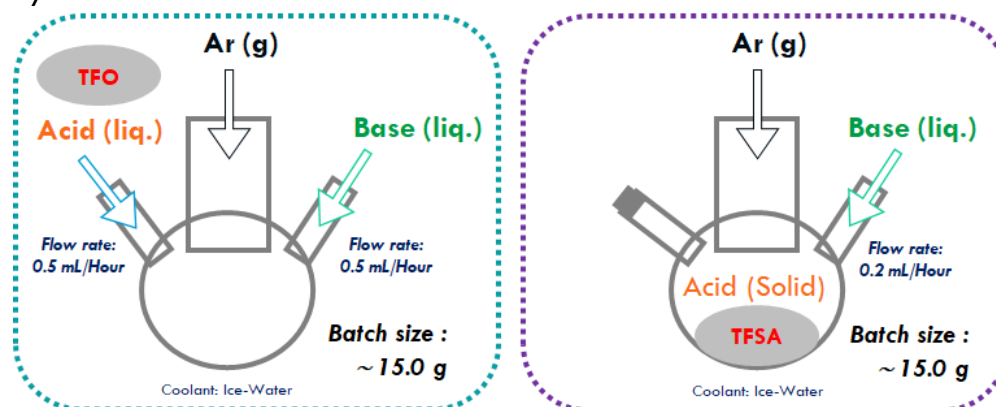


Fig. 4.2. Schematic presentation of the synthesis of PILs/PSs.

Also, in each case, around 15.0 g/batch of PILs was synthesized. To increase the batch size, a 2<sup>nd</sup> batch of 15.0 g PILs could be prepared in the same reaction vessel simply by adding acid in the already prepared PILs from the 1<sup>st</sup> batch with the subsequent addition of amine per the previous procedure.

In our observation, if a large amount of HTFSA/[TFSA]<sup>-</sup> is present in the flask (100 mL), then it was very difficult to control the residual heat and thus instead of transparent PILs, coloured sample was obtained. So, we recommend that during synthesis depending on the targeted batch size, reaction apparatus and synthetic condition, i.e., rate of addition should be carefully optimized as the purity of the product is very sensitive to the heat evolved during the reaction.

In general, after the preparation of [TFSA]<sup>-</sup> based PILs, the excess amine was removed by vacuum drying at 80 °C (24 h). But, for [2-Mpra][TFSA], [N-Eipra][TFSA] and [Dema][TFSA], the highest temperature for drying was 60 °C and was constant for 24 h. In all cases, the temperature for drying was gradually raised from 30 °C (6h) to the highest temperature.

In the case of other primary alkylamine-PILs based on oxo acids, both neat amine and acid was added simultaneously via pressure-equalizing dropping funnel in a three-neck round bottom flask. In such case, solid product was obtained so to mix them properly, small amount of acetonitrile was added as solvent and the mixture was mixed again overnight in a room temperature water bath. After that the solvent was removed by vacuum drying at 50 °C for 24 h. Due to the high melting point of these class of PILs, final temperature of drying was set at 100 °C for 48 h.

Finally, the PILs were kept in an Ar atmosphere glove box (VAC, [O<sub>2</sub>] < 1 ppm, [H<sub>2</sub>O] < 1 ppm). The water contents of PILs were determined to be below 200 ppm by Karl-Fischer titration.

#### 4.2.2. Physicochemical characterization of protic ionic liquids

Phase analysis were done via a DSC 7020 differential scanning calorimeter (Hitachi, Japan) under an N<sub>2</sub> atmosphere. In an Ar atmosphere inside of a dry glove box, the samples were sealed in aluminium pans. Then, the samples were subjected to the following thermo-profile in which temperature was scanned at first from 150 °C to -150 °C, then again from -150 °C to 150 °C (rate of heating/cooling: 10 °C min<sup>-1</sup>). DSC thermogram was recorded while performing the reheating scans.

Thermogravimetric measurements were conducted using a TG-DTA 7200 thermo-gravimetry/differential thermal analyzer (Hitachi, Japan) from room temperature to 550 °C at a heating rate of 10 °C min<sup>-1</sup> under an N<sub>2</sub> atmosphere with open aluminium pans. The decomposition temperature ( $T_d$ ) was determined as the temperature at which 5% mass loss was began.

FT-IR spectra were recorded on a Nicolet iS50 FT-IR spectrometer (Thermo-scientific, USA) in the 1000–4000 cm<sup>-1</sup> range using CaF<sub>2</sub> disks at room temperature. Samples for IR spectra were prepared inside the dry box.

The viscosity was measured via a Physica MCR 301 rheometer (Anton Paar, Austria) using a CP501 cone plate (50 mm in diameter, 1° angle) under dry air conditions at a temperature controlled in the range of 25 °C–100 °C. At zero shear rate, the sample was equilibrated at each temperature for 15 minutes prior to the measurement. Then, a steady preshear was applied at a shear rate of 1 s<sup>-1</sup> for 60 s followed by a 120 s rest period before each measurement to remove any previous shear histories. The viscosity value was taken at zero shear rate. For, shear thinning behaviour, shear rate was varied from 10 s<sup>-1</sup> to 8000 s<sup>-1</sup>. At temperatures above 25 °C, viscosity of the sample reduces greatly which in turn results the expulsion of samples under very high shear rate, i.e., 8000 s<sup>-1</sup>. Thus, the highest shear rate was kept at 4000 s<sup>-1</sup> for measurements at 40 °C, 60 °C, 80 °C, and 100 °C.

Conductivities were obtained by deploying a CG-511 B electrical conductivity cell (DKK-TOA corporation, Japan). The cell was comprised of two platinum black electrodes. Prior to the measurement, the cell was cleaned by water and ethanol respectively for three times each. After drying, the conductivity cell was immersed in a test tube containing ~1.5 mL of PILs. Then, the complex impedance spectra were measured using a Biologic VMP2 multi-potentiostat (Biologic, France) in the frequency range of 1 Hz to 1 MHz. The cell constant of the conductivity cell was determined with a solution of 0.01 M KCl at 25 °C. And, the impedance spectra of respective PILs were measured from 30 °C to 100 °C using a ESPEC SU-261 constant temperature oven (ESPEC, Japan). Prior to the measurement of impedance spectra, the samples were thermally equilibrated at each temperature for ~1 h. After acquiring the spectra, the conductance was determined from the actual axis touchdown point in the Nyquist plots of impedance data.

A DA-100 thermoregulated density/specific gravity meter (Kyoto Electronics Manufacturing Co. Ltd., Japan) was used to measure the density in the range of 15 °C–40 °C. For high melting temperature PILs, the measurement was hindered by the limitation of the instrument.

<sup>1</sup>H-NMR spectra were acquired with a JEOL JNM-AL 400 NMR spectrometer (JEOL, Japan) using a SC-002 5-mm coaxial capillary (Shigemi, Tokyo) with the sample in the inner tube and the reference solvent (DMSO-d<sub>6</sub> having 1% TMS) in the outer tube. <sup>1</sup>H

chemical shifts were externally referenced to the TMS peak. The NMR data was processed by using a data analysis software ALICE 2, version 6 (JEOL, Japan).

### 4.3. Results & Discussion

First, thermal properties in combination with FT-IR and NMR spectroscopy were performed to probe the N-H bond strength to provide detail on the effect of networking H-bonds. The thermal decomposition temperature ( $T_d$ , see ESI†) was higher for [2-Ehexa][TFSA] than the PILs with shorter alkyl chain in their cationic structure as shown in Fig. 4.3a.

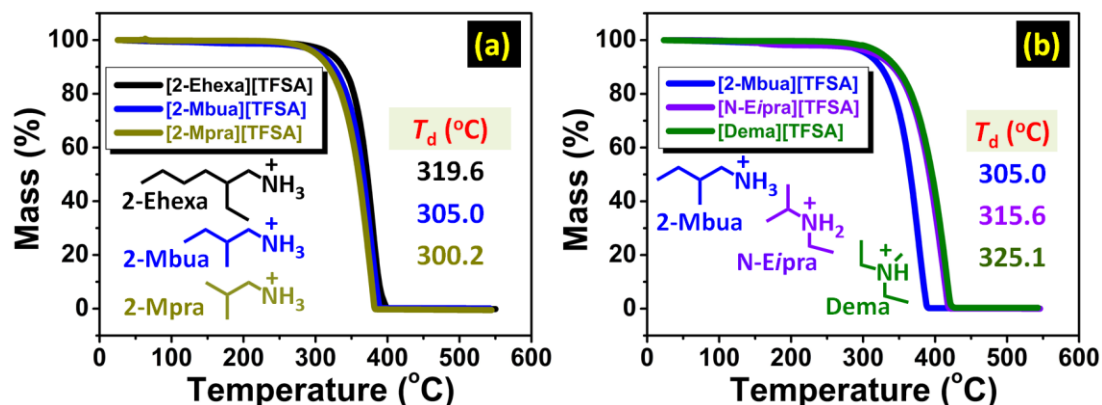


Fig. 4.3. Thermo-gravimetric curves for PILs with the variation in (a) alkyl chain length, and (b) number of hydrogen bond donors.

Moreover, it was lowest for [2-Mbua][TFSA] (Fig. 4.3b) than its isomeric counterparts. In general, the thermal stability of such PILs are superior to the EAN series due to high  $\Delta pK_a$ ,<sup>10-11</sup> but inferior to tertiary amine-PILs with alkylammonium cationic structure.<sup>17</sup> The change in  $T_d$  for primary alkylamine-PILs with different cations was relatively small owing to the somewhat similar  $\Delta pK_a$ . We further investigated [2-Ehexa]<sup>+</sup> with other anions providing greater variability in  $\Delta pK_a$  (see Fig. 4.4a-b), which was congruent with the previous report in which  $T_d$  was greatly influenced by  $\Delta pK_a$  because of the change in the strength of N-H bonds.<sup>18</sup> Thus, regarding TG for variation of cationic structure, we could infer that small variations in thermal stability are related to the perturbation in the weaker interactions, for example H-bonds, rather than stronger interaction i.e. N-H bond.

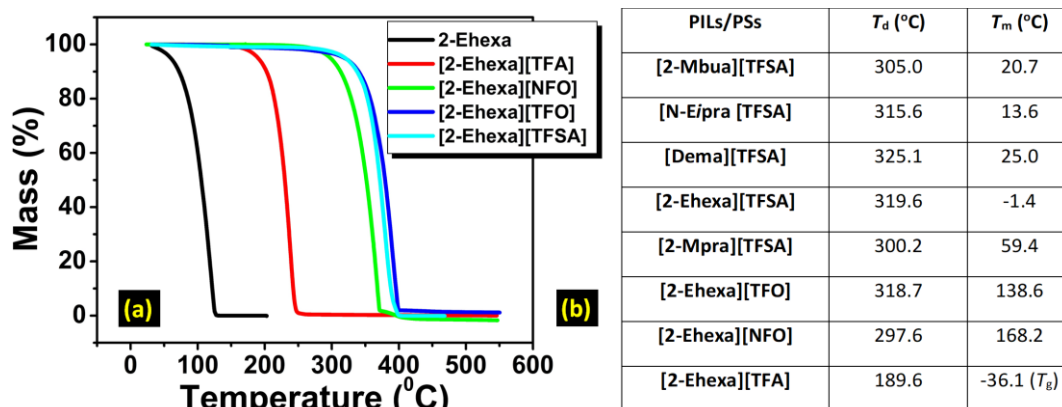


Fig. 4.4.(a) Thermogravimetry curves of primary alkylamine-PILs showing the effect of anionic structure. (b) Thermal properties of all the PILs/PSs synthesized in this work.

Furthermore, DSC measurements revealed an interesting change in phase behaviour for the primary alkylamine-PILs as shown in **Fig. 4.5a** and **Fig. 4.4b**. Reduction in alkyl chain length increased the melting point (**Fig. 4.5a**), attributed to the decrease of asymmetry of cation contributing to efficient ion-packing.<sup>11</sup> Here we again note that we further considered the role of the anion for [2-Ehexa]<sup>+</sup> (**Fig. 4.5a-b**).

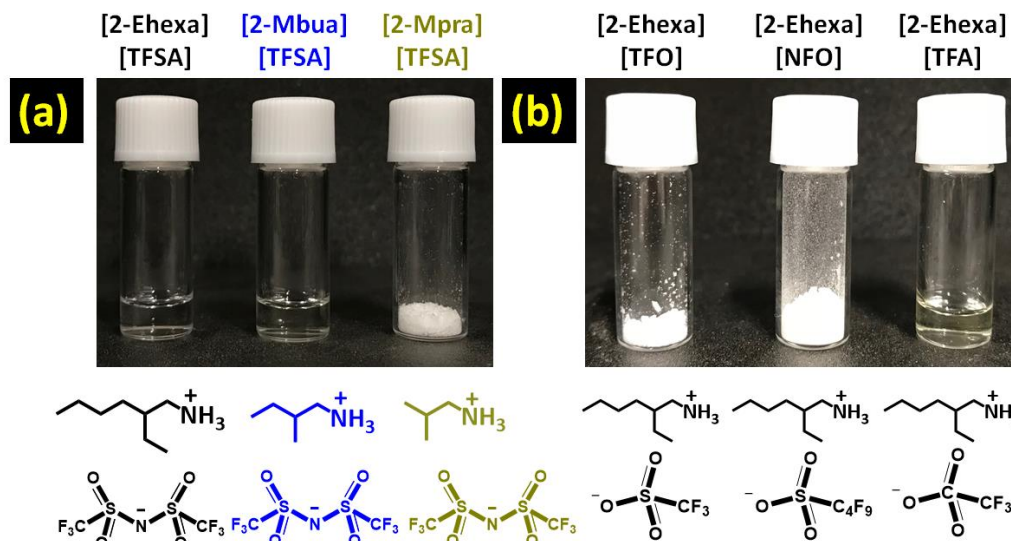


Fig. 4.5. Primary alkylamine (2-Ethylhexylamine) based PILs/PSs with the variation in the (a) alkyl chain length of cations, and (b) oxo-acids.

Aside from the [TFSA]<sup>-</sup> salt, further investigation of 2-Ehexa based PILs resulted in only one liquid product, that is, [2-Ehexa][TFA] due to reduction in  $\Delta pK_a$  as both [2-Ehexa][TFO] and [2-Ehexa][NFO] were high melting PSs (**Fig. 4.4b**). With the decrease of  $\Delta pK_a$ , in primary alkylamine-PILs, strength of N-H bond became weaker thereby reducing the ion-pair interaction energy as observed for tertiary alkylamine-PILs.<sup>5</sup> Therefore, change in phase behaviour was noticed. Although not included in this work, we attempted several other branched alkylamines in combination with [TFO]<sup>-</sup> which did not yield room temperature liquids. Therefore, although true reason for such contrasting phase behaviour is still unknown, H-bonds have the most significant effect in the phase transition of primary alkylamine-PILs as observed in EAN analogues.<sup>5-7</sup> At high  $\Delta pK_a$ , conformational robustness<sup>5</sup> of [TFSA]<sup>-</sup> than [TFO]<sup>-</sup> was crucial to off-set the interaction energy and in turn efficient ion-packing.

Also, reduction in the number of H-bond donors (primary amine to secondary amine) resulted in melting point suppression (**Fig. 4.6a** and **Fig. 4.7**) as the possibility of forming networking H-bonds<sup>9,16</sup> was lessened. However, considering previous reports in AILs,<sup>19</sup> H-bonding promoted fluidity and reduction in melting points. So, primary amine-PILs might represent a borderline solvent between PILs and molecular liquids, whereas tertiary amine-PILs could be considered more like AILs. This shift is presumably driven by subtle changes in the relative contributions of intermolecular interactions such as H-bonding, London forces etc. in these coulombic fluids as reported in earlier research.<sup>20</sup> Overall, these DSC results indicate that networking H-bonds might have a greater effect in primary amine-PILs.

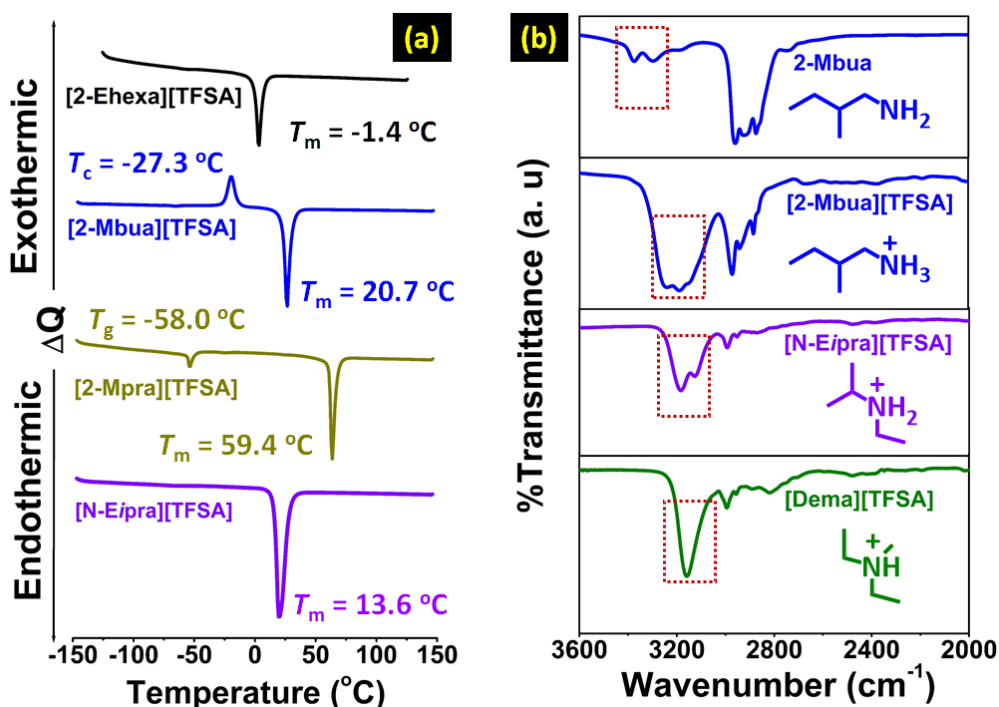


Fig. 4.6. (a) DSC patterns of PILs, (b) FT-IR spectra of the neutral amine 2-Mbua and PILs.

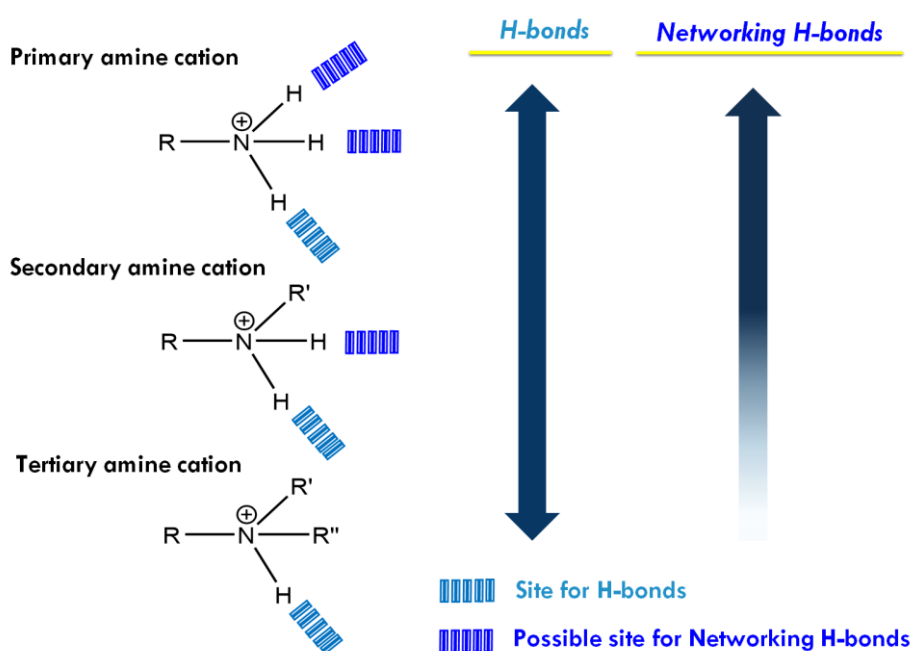


Fig. 4.7. Possible interaction sites for H-bonds and networking H-bonds in protic ionic liquids depending on the number of H-bond donors in the structure of cation.

FT-IR spectra of the PILs are shown in **Fig. 4.6b**. [2-Mbua][TFSA] exhibited a broad band corresponding to symmetric and asymmetric N-H stretching.<sup>21</sup> The broad band was comprised of maxima centered at  $\sim 3200$   $\text{cm}^{-1}$  flanked by two shoulder peaks around  $\sim 3260$   $\text{cm}^{-1}$ , and  $\sim 3140$   $\text{cm}^{-1}$  respectively. A similar spectral pattern was observed for EAN.<sup>8</sup> To confirm the assignment of the bands of [2-Mbua][TFSA], FT-IR spectrum of the (neutral) primary amine, 2-Mbua was also recorded exhibiting only two broad bands at  $\sim 3380$   $\text{cm}^{-1}$  and  $\sim 3290$   $\text{cm}^{-1}$ .<sup>21</sup> Thus, the additional band in [2-Mbua][TFSA] could arise

due to the N-H bonded species introduced via protonation. On the other hand, the secondary alkylamine-PIL, [N-Eipra][TFSA] exhibited two distinct peaks at  $\sim 3190\text{ cm}^{-1}$  and  $\sim 3130\text{ cm}^{-1}$ .<sup>21</sup> And, the tertiary alkylamine-PIL, [Dema][TFSA] showed only a narrow single peak at  $3159\text{ cm}^{-1}$  for the N-H bond.<sup>22</sup> For the longer chain cation in [2-Ehexa][TFSA], similar findings were obtained (Fig. 4.8).

If we consider the most intense N-H peak (Fig. 4.6a and Fig. 4.8), then in changing from a tertiary to primary amine cation, the N-H peak position shifted a little to higher wavenumber.<sup>23</sup> However, exact assignment of these bands to the specific chemical species is challenging due to the existence of rotational isomers of primary amine.<sup>23</sup>

<sup>1</sup>H-NMR spectra may support multiple H-bonds observed in FT-IR spectra for primary alkylamine-PILs, exhibiting the single N-H proton peak<sup>24</sup> (Fig. 4.9a-b) that indicates the time scale of NMR is sufficiently long to average the multiple H-bonds. Note that the chemical shift of [2-Mbua][TFSA] is 5.84 ppm, which is lower than [N-Eipra][TFSA] (5.93 ppm) and [Dema][TFSA] (6.72 ppm). The multiple H-bonds in [2-Mbua][TFSA] are averaged, and thus, the averaged electron density of N-H protons could become higher for [2-Mbua][TFSA]. This is also evident from the FT-IR spectra, where the lower wavenumber limit of the broad peaks in [2-Mbua][TFSA] and [N-Eipra][TFSA] do not appear at higher wavenumber than that of [Dema][TFSA], despite the previously discussed trend (*vide supra*) in the peak maxima. Similar proton chemical shifts were observed for all the primary alkylamine-PILs i.e. [2-Ehexa][TFSA], [2-Mbua][TFSA], and [2-Mpra][TFSA]. Generally, a large downfield shift for the N-H

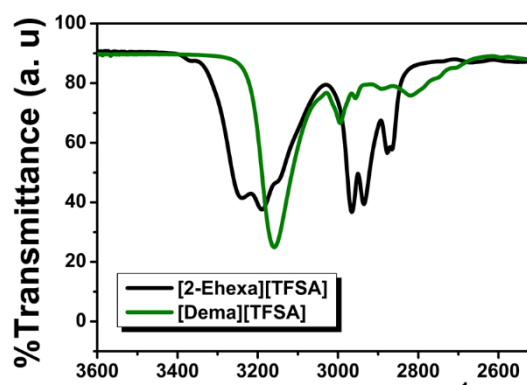


Fig. 4.8. FT-IR spectra of [2-Ehexa][TFSA] in comparison with [Dema][TFSA] at room temperature.

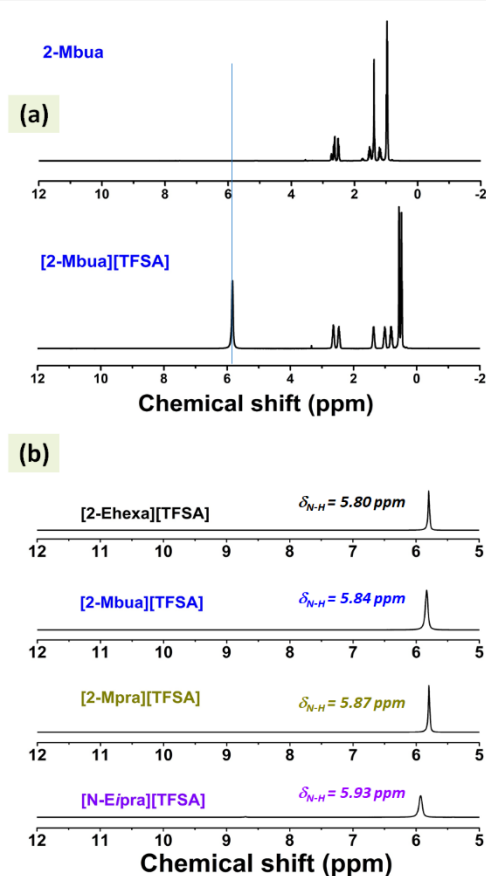


Fig. 4.9. <sup>1</sup>H-NMR spectra of (a) primary amine (neutral) and the corresponding PILs, (b) PILs with primary and secondary amine cations measured at 40 °C.

proton was demonstrated with the change in anion basicity/ $\Delta pK_a$ .<sup>24</sup> But, here, the difference in  $\Delta pK_a$  was marginal. Finally, rheological study coupled with transport properties as a function of temperature were performed to gain in-depth understanding about the dominant effect of H-bonds. Then, Walden plot analysis was performed to reveal the effect of such inter-ionic interaction over the ionic nature of primary alkylamine-PILs.

Stress controlled rheometric analysis has been perceived to be useful to unravel the role of H-bonding in ILs.<sup>25</sup> Herein, at zero shear rate, viscosity of [2-Mbua][TFSA] was approximately four and eight times higher than [N-Eipra][TFSA] and [Dema][TFSA] respectively at 25 °C (**Fig. 4.10a**). Interestingly, [2-Mbua][TFSA] exhibited a rapid decrease of viscosity above a shear rate of  $\sim 570 \text{ s}^{-1}$ ; an indication of shear thinning phenomena.<sup>26</sup> The onset of shear thinning for [TFSA]<sup>-</sup> based primary amine-PIL was higher than EAN, EAF (Ethylammonium formate), and PAN (Propylammonium nitrate) (above  $\sim 100 \text{ s}^{-1}$ ).<sup>26</sup>

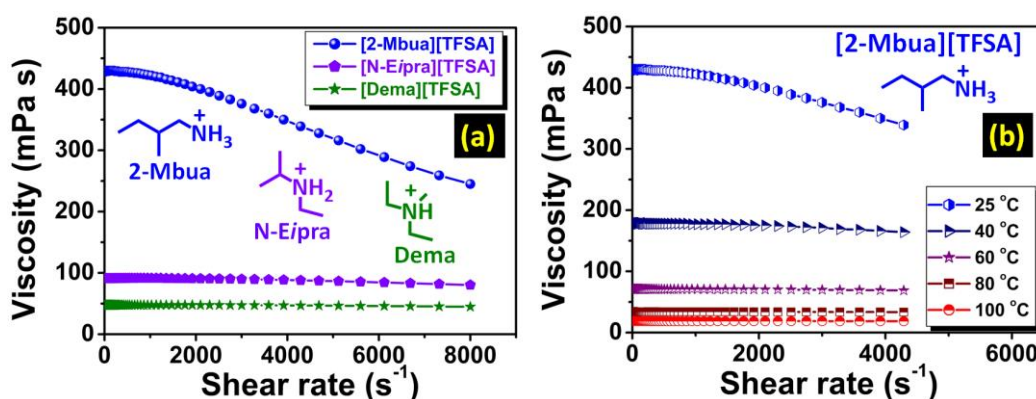


Fig. 4.10. Change of viscosity as a function of shear rate (a) at 25 °C, (b) under various temperatures. For Fig. 3b, shear rate was limited to  $4000 \text{ s}^{-1}$  at higher temperatures due to the expelling of the samples at very high shear rate.

The onset of shear thinning has been reported to be dependent on the number of H-bonds in PILs.<sup>27</sup> The usage of [TFSA]<sup>-</sup> ( $(\text{CF}_3\text{SO}_2)_2\text{N}^-$ ) as anion could serve as the multiple sites for H-bonding which includes the both O atoms<sup>28</sup> in the  $-\text{SO}_2-$  parts as well as the N<sup>-</sup><sup>28</sup> in contrast with  $\text{NO}_3^-$  in EAN.<sup>5,9</sup> So, an increment in the onset of shear thinning is indicative of the build-up of denser H-bonding networks in the current series of PILs compared to EAN. Additionally, the onset of shear thinning for [2-Ehexa][TFSA] ( $\sim 950 \text{ s}^{-1}$ ) was increased as shown in **Fig. 4.11 a**.

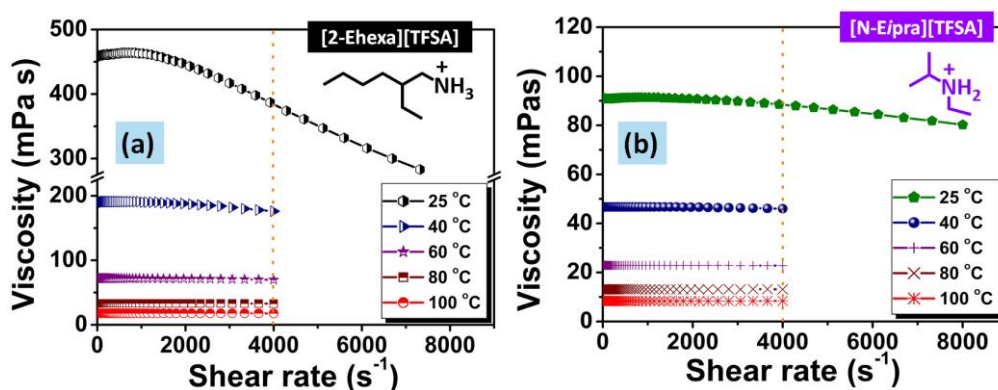


Fig. 4.11. Change of viscosity as a function of shear rate under various temperatures. Shear rate was limited to  $4000 \text{ s}^{-1}$  from  $40 \text{ °C}$  due to the expelling of the samples at very high shear rate.

For the EAN series, the onset value of shear thinning was correlated to their nanostructure in which the anion had less effect and cation with longer chains generated better defined nanostructure (bicontinuous microemulsions or more closely corresponding to  $L_3$  (sponge)

phases) without affecting its type.<sup>29</sup> The nanostructure of the current systems is still unknown right now. But, it could be assumed that the concomitant increases in the onset of shear thinning for current [TFSA]<sup>-</sup> based primary alkylamine-PILs could be associated with the amphiphilicity of the cation leading to the increased degree of segregation between polar and apolar domains and thus a well-defined nanostructure.<sup>29</sup> On the contrary, [N-Eipra][TFSA] displayed only a meagre loss of viscosity with shear rate, and for [Dema][TFSA] it was almost invariant akin to the observation of Separovic *et. al.*<sup>30</sup> for tertiary amine-PILs. Overall, this is the first conspicuous observation of the effect of networking H-bonds in primary amine-PILs with high  $\Delta pK_a$ , as previously reported for functionalized PILs like free/pendant -OH, -NH<sub>2</sub> and -SH groups.<sup>31</sup> As we know, although being coulombic fluids, in PILs, there is a competition between the non-covalent interactions such as H-bonding, London forces etc.<sup>29</sup> As evidenced from the rheological analysis, dominance of H-bonding could drastically shift the relative contribution of these forces. Therefore, at low temperature, primary amine-PILs exhibit properties resembling molecular liquids, but at high temperature resembling those of ALLs. The presence of H-bonds in ionic liquids is quite compelling and especially for PILs.<sup>16</sup> Like H-bonds in conventional media, they are quite responsive to external stimuli, such as temperature.<sup>30</sup> Under temperature variation, [2-Mbua][TFSA] displayed a change in shear thinning from 'strong' to 'no thinning' as shown in **Fig. 4.10b**. It was noticeable that from 60 °C, shear thinning was absent supporting the intrinsic *non-Newtonian* character of primary amine-PILs like EAN (**Fig. 4.10a**). Thus, microscopically, the local structure of [2-Mbua][TFSA] was strongly influenced by the short-range networking H-bonds controlling its macroscopic characteristics. During temperature increase, however, those short-range interactions become weaker owing to the thermal perturbations finally resulting a liquid structure dominated by the coulombic interactions and London forces instead of networking H-bonds. Such temperature-tuneable transitions of long range forces in PILs have also been highlighted recently by Rutland *et. al.*<sup>7</sup> for EAN. This further demonstrates the unique but more perplexing micro-heterogeneity in PILs, especially for primary amine-PILs which require further investigation.

As demonstrated in **Fig. 4.12a**, for [2-Mbua][TFSA], viscosity decreased more rapidly from 25 °C to 60 °C than from 60 °C to 120 °C. Conversely, the change in conductivity showed the opposite trend (**Fig. 4.12a**). Similar behaviour was noticed for [N-Eipra][TFSA] (**Fig. 4.13a**) but at below and above 40 °C in accordance with the rheological responses (**Fig. 4.11b**). For [Dema][TFSA], such transitional behaviour was not noticed (**Fig. 13b**). So, the PILs can switch their *non-Newtonian* fluidic character at certain threshold temperature pertaining to the degree of H-bonding in them. The order of maximum temperature for shear thinning was primary (60 °C) > secondary (40 °C) > tertiary (not applicable). Therefore, the order of number of networking H-bonds could be primary > secondary > tertiary (**Fig. 4.7**).

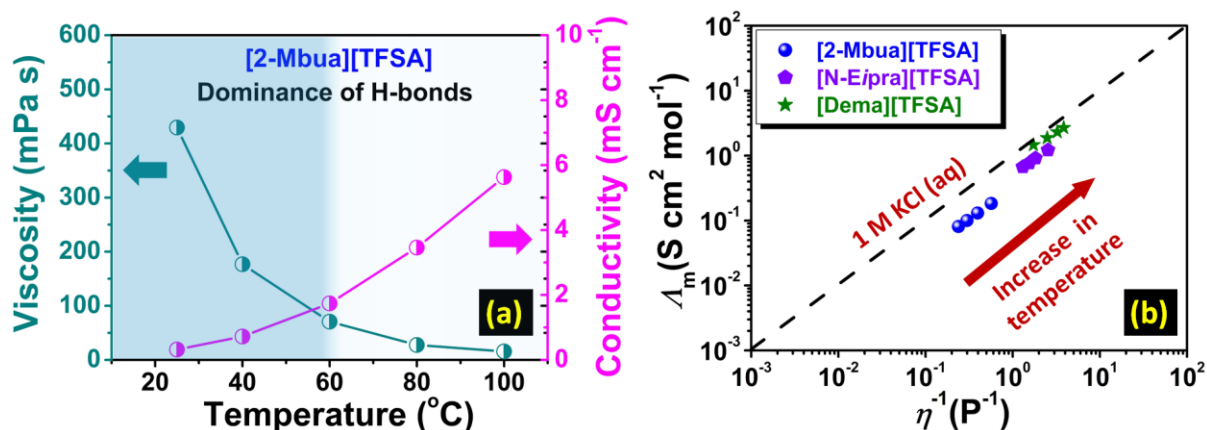


Fig. 4.12.(a) Change of viscosity and conductivity as a function of temperature, (b) Walden plot (25 °C–100 °C).

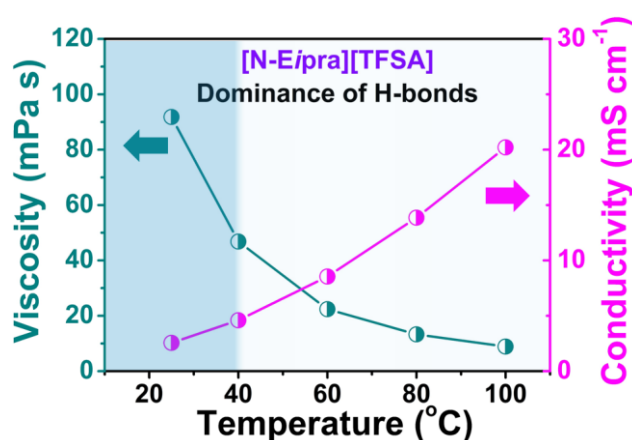


Fig. 4.13. Viscosity and conductivity as a function of temperature for (a) secondary and (b) tertiary amine-PILs.

Considering the above discussion, such a high extent of inter-ionic interactions could possibly affect the ionicity of primary amine-PILs, which was further explored via Walden plot analysis.<sup>32</sup> As shown in **Fig. 4.12b**, [2-Mbua][TFSA] lied farthest from the ideal KCl line. In comparison, [N-Ei/pra][TFSA] was much closer to the ideal line (**Fig. 4.12b**) than [2-Mbua][TFSA]. And, [Dema][TFSA] was located just beneath the ideal line as per the previous study.<sup>33</sup> The extent of the deviation from the Walden plot could be a rough estimation of ionicity typically known as the Walden rule.<sup>34</sup> Ideally, PILs should be closer to the ideal KCl line, because, at high  $\Delta pK_a$ , proton transfer is almost complete, and more so in primary amine-PILs even at low  $\Delta pK_a$  (10).<sup>35</sup> Instead, in [TFSA]<sup>-</sup> based primary amine-PILs ionicity was lowered due to the distinct segregation of ions into polar and apolar domains stemming from the enhanced networking H-bonds in them. A decrease in ionicity with increasing nanophase separation has been observed in typical imidazolium-based AILs.<sup>36</sup> Such an effect could be diminished in reducing the number of H-bond donors from primary amine-PILs to tertiary amine-PILs, and in turn enhancing the ionicity of PILs system (**Fig. 4.12b**). Observation of shear thinning also supported the deviation in the Walden plot for primary amine-PILs (**Fig. 4.10a**). Thus, the results of this work further invoke the common perception about the ionic nature of PILs, which was also highlighted in a recent study.<sup>7</sup>

#### 4.4. Conclusions

In closing, a novel series of primary alkylamine-PILs were successfully synthesized via judicious selection of amines with [TFSA]<sup>-</sup> anion. Via systematic variation in the cationic structures, we conclude that networking H-bonds unambiguously dictated the observed physicochemical properties of such PILs, for instance lower thermal stability, temperature driven inversion of *non-Newtonian* behaviour, and lower ionicity. These findings are quite fascinating and will surely ignite new interest in ionic liquid community to further explore the properties and microstructures of this important class of PILs, reminiscent of EAN, for task-specific applications.<sup>37</sup>

#### 4.5. Note and References

1. D. R. MacFarlane, A. L. Chong, M. Forsyth, M. Kar, R. Vijayaraghavan, A. Somers, and J. M. Pringle, *Faraday Discuss.*, 2018, **206**, 9–28.
2. M. Watanabe, M. L. Thomas, S. Zhang, K. Ueno, T. Yasuda, and K. Dokko, *Chem. Rev.*, 2017, **117**, 7190–7239.
3. T. L. Greaves, and C. J. Drummond, *Chem. Rev.*, 2015, **115**, 11379–11448.
4. P. Walden, *Bull. Acad. Imp. Sci.*, 1914, 1800.
5. R. Hayes, S. Imberti, G. G. Warr, and R. Atkin, *Angew. Chem. Int. Ed.*, 2013, **52**, 4623–4627.
6. A. Mondal, and S. Balasubramanian, *J. Phys. Chem. B*, 2015, **119**, 1994–2002.
7. N. Hjalmarsson, R. Atkin, and M. W. Rutland, *Chem. Commun.*, 2017, **53**, 647–650.
8. I. A. Sedov, T. I. Magsumov, T. M. Salikov, and B. N. Solomonov, *Phys. Chem. Chem. Phys.*, 2017, **19**, 25352–25359.
9. K. Fumino, A. Wulf, and R. Ludwig, *Angew. Chem. Int. Ed.*, 2009, **48**, 3184–3186.
10. pK<sub>a</sub> difference between the acid and base precursors.
11. J.-P. Belieres, and C. A. Angell, *J. Phys. Chem. B*, 2007, **111**, 4926–4937.
12. H. Abe, K. Nakama, R. Hayashi, M. Aono, T. Takekiyo, Y. Yoshimura, K. Saihara, and A. Shimizu, *Chem. Phys.*, 2016, **475**, 119–125.
13. A. Garlitz, C. A. Summers, R. A. Flowers, and G. E. O. Borgstahl, *Acta Cryst.*, 1999, **D55**, 2037–2038. H. Weingärtner, C. Cabrele, and C. Herrmann, *Phys. Chem. Chem. Phys.*, 2012, **14**, 415–426.
14. S. Zhang, M. S. Miran, A. Ikoma, K. Dokko, and M. Watanabe, *J. Am. Chem. Soc.*, 2014, **136**, 1690–1693.
15. C. Ridings, G. G. Warr, and G. G. Andersson, *J. Phys. Chem. Lett.*, 2017, **8**, 4264–4267.
16. P. A. Hunt, C. R. Ashworth, and R. P. Matthews, *Chem. Soc. Rev.*, 2015, **44**, 1257–1288.
17. H. Nakamoto, and M. Watanabe, *Chem. Commun.*, 2007, 2539–2541.
18. M. S. Miran, H. Kinoshita, T. Yasuda, M. A. B. H. Susan, and M. Watanabe, *Chem. Commun.*, 2011, **47**, 12676–12678.
19. K. Fumino, A. Wulf, and R. Ludwig, *Angew. Chem. Int. Ed.*, 2008, **47**, 8731–8734.
20. U. L. Bernard, E. I. Izgorodina, and D. R. MacFarlane, *J. Phys. Chem. C*, 2010, **114**, 20472–20478. K. Fumino, and R. Ludwig, *J. Mol. Liq.*, 2014, **192**, 94–102.
21. L. J. Bellamy, *The Infrared Spectra of Complex Molecules*, 3rd ed., Chapman and Hall, 1975, **1**, pp. 289–291.

22. K. Mori, S. Hashimoto, T. Yuzuri, and K. Sakakibara, *Bull. Chem. Soc. Jpn.*, 2010, **83**, 328–334.
23. L. J. Bellamy and R. L. Williams, *Spectrochim. Acta*, 1957, **9**, 341–345. P. J. Kruegera, and D. W. Smith, *Can. J. Chem.*, 1967, **45**, 1605–1610.
24. M. S. Miran, H. Kinoshita, T. Yasuda, M. A. B. H. Susan and M. Watanabe, *Phys. Chem. Chem. Phys.*, 2012, **14**, 5178–5186.
25. K.R. Seddon, A. Stark, and M. J. Torres, *ACS Symp. Ser.*, 2002, **819**, 34–49.
26. J. A. Smith, G. B. Webber, G. G. Warr, and R. Atkin, *J. Phys. Chem. B*, 2013, **117**, 13930–13935.
27. E. G. Blanco-Díaza, E. O. Castrejón-González, J. F. Javier Alvaradoa, A. Estrada-Baltazara, and F. Castillo-Borja, *J. Mol. Liq.*, 2017, **242**, 265–271.
28. A. E. Khudozhitkov, P. Stange, B. Golub, D. Paschek, A. G. Stepanov, D. I. Kolokolov, and R. Ludwig, *Angew. Chem. Int. Ed.*, 2017, **56**, 14310–14314.
29. R. Hayes, S. Imberti, G. G. Warr and R. Atkin, *Phys. Chem. Chem. Phys.*, 2011, **13**, 3237–3247. J. N. Israelachvili, D. J. Mitchell, and B. W. Ninham, *J. Chem. Soc. Faraday Trans. 2*, 1976, **72**, 1526–1568.
30. G. L. Burrell, N. F. Dunlop, and F. Separovic, *Soft Matter*, 2010, **6**, 2080–2086.
31. D. M. Teegarden, in *Polymer Chemistry: Introduction to an Indispensable Science*, National Science Teachers Association, NSTA Press, Arlington, VA, USA, 2004, p. 280.
32. P. Walden, *Z. Phys. Chem.*, 1906, **55**, 207.
33. M. S. Miran, T. Yasuda, M. A. B. H. Susan, K. Dokko, and M. Watanabe, *J. Phys. Chem. C*, 2014, **118**, 27631–27639.
34. W. Xu, E. I. Cooper, and C. A. Angell, *J. Phys. Chem. B*, 2003, **107**, 6170–6178.
35. J. Stoimenovski, E. I. Izgorodina, and D. R. MacFarlane, *Phys. Chem. Chem. Phys.*, 2010, **12**, 10341–10347.
36. H Tokuda, K Hayamizu, K Ishii, M. A. B. H. Susan, M Watanabe, *J. Phys. Chem. B*, 2005, **109**, 6103–6110.
37. K. Dong, S. Zhang and J. Wang, *Chem. Commun.*, 2016, **52**, 6744–6764.

## CHAPTER 5 PROTIC SALTS AND PROTIC IONIC LIQUIDS DERIVED ELECTROACTIVE MATERIALS

### ***Molecular level tuning of electro-materials based on protic ionic liquids/salts oxygen reduction electrocatalysis: Effect of cationic structure***

#### 5.1. Introduction

#### 5.2. Experimental Details

##### 5.2.1. Synthesis of protic ionic liquids/salts

Protic ionic liquids and salts were synthesized by following the previous procedures.

##### 5.2.2. Synthesis of carbon materials

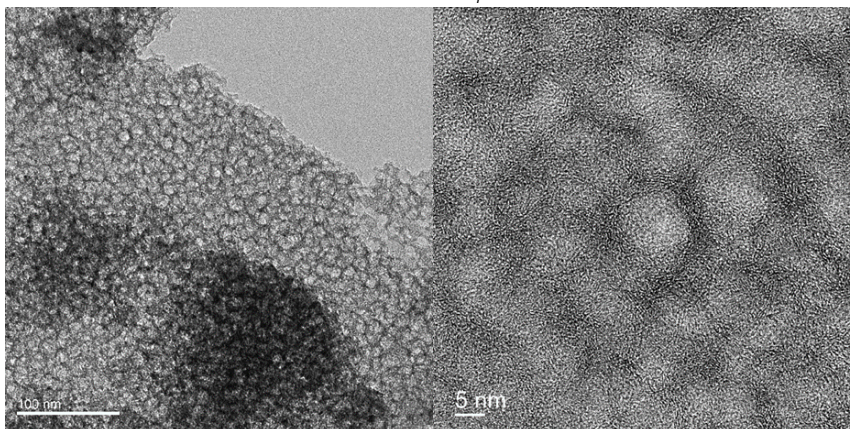
Carbon materials were synthesized via mixture of 80 mol% of protic salt, and 20 mol% of iron halide ( $\text{FeCl}_3$ ) in a 2.0 g mixture in which 4.5 g of colloidal silica (LUDOX-HS40) was added. Then, the mixture was vigorously mixed via a magnetic stirrer until a homogenous mixture was obtained. After that, it was dried at 80 °C in an electric oven for overnight and then grounded into fine powder form by mortar and pestle. Then, it was subjected into thermal annealing under Ar (g) via the following temperature ramp scheme: (1) holding the temperature at room temperature for 1 h. (2) increase of the temperature at the heating rate of 10 °C  $\text{min}^{-1}$  from room temperature to 900 °C. (3) holding the temperature at 900 °C for 2h. (4) cooling down the temperature to room temperature. Then the silica template was removed via HF (10.0 mL) and mixed slowly for 48h. Finally, after washing out the etched catalyst via deionized water until the pH reached neutrality, it was dried at 100 °C for overnight.

##### 5.2.3. Materials characterization

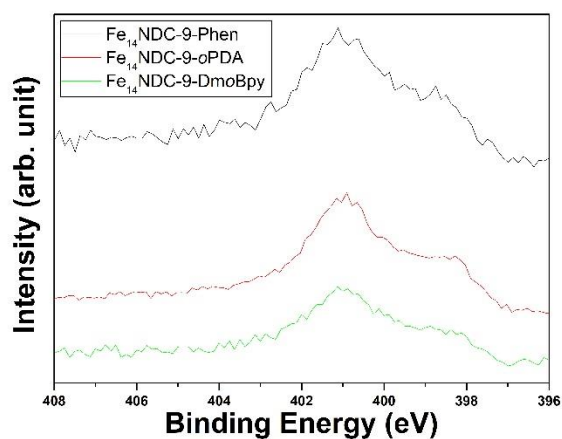
##### 5.2.4. Electrochemical characterization

#### 5.3. Results and Discussion

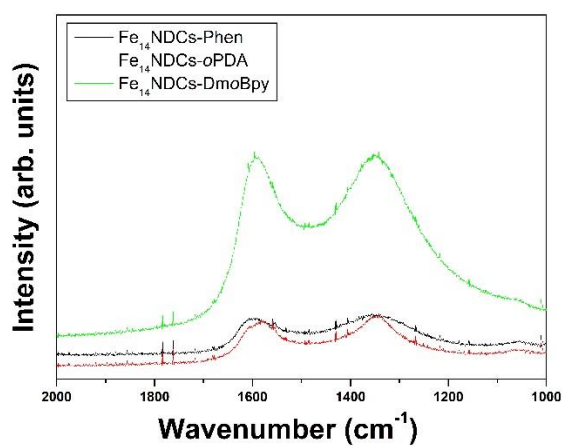
##### 5.3.1. Structural features of electro-materials based PILs/PSs



TEM micrographs of Fe<sub>14</sub>NDC<sub>9</sub>-Phen.



N1s HR-XPS of FeNDCs prepared from various PSs.



Raman spectra of FeNDCs prepared from various PSs.

### 5.3.2. Electrochemical features of electro-materials based PILs/PSs

### 5.4. Closing Remarks

(Electrochemical experiments and analysis regarding to this chapter is in progress)

## CHAPTER 6 GENERAL CONCLUSIONS AND PROSPECTS

### 6.1. Overall summary

In summary, we have reported herein the fabrication of a highly efficient ORR catalyst based on a low-cost and robust carbonaceous precursor, protic salt. This impressive performance was achieved via the successful incorporation of a silica template with the combination of a protic salt and a simple iron salt. The derived carbon materials had interesting microscopic features, including high specific surface area, micro-mesoporosity with dominant mesopores and active motifs such as  $N_x$ -Fe, N-py, and N-g (valley). Controlling the concentration of these motifs in the FeNDCs is pivotal to their relative activity and stability in electrolytes with wider pH.

The prototype catalyst, Fe<sub>14</sub>NDC-9, displayed the highest onset potential of 0.968 V and a half-wave potential of 0.888 V in alkaline media. For Fe<sub>14</sub>NDC-9, the ORR proceeded exclusively via a 4e transfer process. Also, in acidic media, Fe<sub>14</sub>NDC-9-W<sub>2M</sub>-9 showed onset potential at 0.821 V, 4e transfer process in the low overpotential region, and a half-wave potential of 0.730 V. Short-term stability tests in both electrolytes were reasonable. Overall, this result is encouraging, as the developed catalyst is free from any additional high-surface-area carbon support or additives like MOFs. Moreover, simplicity of the synthesis of the protic salt, [Phen][2HSO<sub>4</sub>], and the versatility of the ionic liquid platform make this molecular-level carbon precursor a unique approach for developing transition metal based catalysts, i.e., iron for fuel cells.

In terms of electrolyte, a novel series of primary alkylamine-PILs were successfully synthesized via judicious selection of amines with [TFSA]<sup>-</sup> anion. It is important to note that oxo anion such as trifluoromethanesulfonate yielded high melting PSs owing to their less flexible structure. Instead, bis(trifluoromethane sulfonimide) resulted PILs portraying their conformational superiority over oxo acids. Although, it is conceivable that [TFSA] based primary amine-PILs may not be suitable for electrochemical applications but understanding their physico-chemical properties is thus of great importance for application in molecular self-assembly of macromolecules and as reagents/media in protein chemistry etc. So, a prototype example of primary amine-PILs (2-methylbutylamine, [2-Mbua][TFSA]) was compared with its isomeric secondary (N-ethylisopropylamine, [N-Eipra][TFSA]) and tertiary (Diethylmethylamine, [Dema][TFSA]) counterparts. In detail structure-property relationships revealed that in primary amine-PILs, networking H-bonds have dominant effect which could be nullified by increasing temperature, such as temperature above 60 °C. Such fundamental knowledge paved the way to explore and select a suitable electrolyte to investigate for high temperature non-humidified fuel cells.

Therefore, [2-Mbua][TFA], a primary amine-PIL, was applied as non-aqueous electrolyte and compared with [N-Eipra][TFA], and [Dema][TFA] to understand the effect of protonic species during ORR at 80 °C. In such case, catalyst prepared with the variation in cationic structures such as [Phen][2HSO<sub>4</sub>], [oPDA][2HSO<sub>4</sub>], [DmoBpy][2HSO<sub>4</sub>] were also employed to investigate the microstructural features of the FeNDCs, such as ratio of  $N_x$ -Fe, and N-g (valley).

### 6.2. Future directions

Activity of the FeNDCs has been dictated by their microstructural composition. Especially, in FeNDCs, nitrogen can adopt several atomic configurations depending on its location in Basal plane of carbon lattice. These are known as pyridinic nitrogen (N-py), nitrogen in co-ordination with iron ( $N_x$ -Fe), graphitic nitrogen at the plane (N-g (centre)), graphitic nitrogen at the edge

(N-g (valley)), pyrrolic nitrogen (N-pyr), and oxidized nitrogen species (N-ox). N<sub>x</sub>-Fe and N-g (valley) have been reported to be the most active spots to catalyze the ORR in aqueous media such as alkaline and acidic media. Control over such atomic moieties is a linchpin towards designing FeNDCs applicable in various types of electrolytes. In future, by simply changing anion of the iron salt, such as Fe(SCN)<sub>3</sub>, it could be possible to further tune the ratio of N<sub>x</sub>-Fe, and N-g (valley). Other transition metals, such as cobalt (Co), can also combined with Fe to fabricate bimetallic Fe-CoNDCs for not only ORR but also other energy related electrochemical reactions, such as oxygen evolution reaction (OER), and hydrogen evolution reaction (HER). Switching from halide salt to thiocyanate salt could also pave the way to realize the effect of sulfur in the FeNDCs.

Furthermore, for the removal of silica template, usage of hydrofluoric acid (HF) is an obstacle towards scalability and has negative environmental impact. In such case, nanoparticles of ZnO could also be applied due to the similarity in size and surface functionality with silica (LUDOX-HS40).

### 6.3. List of publications

-  **M. Hoque**, S. Zhang, M. L. Thomas, Z. Li, S. Suzuki, A. Ando, M. Yanagi, Y. Kobayashi, K. Dokko and M. Watanabe, Simple combination of a protic salt and an iron halide: precursor for a Fe, N and S co-doped catalyst for the oxygen reduction reaction in alkaline and acidic media, *J. Mater. Chem. A*, 2018,**6**, 1138-1149.
-  **M. Hoque**, M. L. Thomas, M. S. Miran, M. Akiyama, M. Marium, K. Ueno, K. Dokko and M. Watanabe, Protic ionic liquids with primary alkylamine-derived cations: dominance of hydrogen bonding on observed physicochemical properties, *RSC Adv.*, 2018, **8**, 9790–9794.
-  **M. Hoque**, M. L. Thomas, M. Akiyama, S. Zhang, K. Ueno, K. Dokko and M. Watanabe, Promising oxygen electroreduction performance of iron doped mesoporous carbons in tertiary alkylamine-PILs, *ACS Appl. Energy Mater.*, 2018, *in preparation*.

### 6.4. Other publications by the Author

-  S. S. Satter, **M. Hoque**, M. M. Rahman, M. Y. A. Mollah, and M. A. B. H. Susan, An Approach Towards Synthesis and Characterization of ZnO@AgCore@shell Nanoparticles in Water-in-Oil Microemulsion, *RSC Adv.*, 2014, **4**, 20612–20615.
-  S. S. Satter, **M. Hoque**, M. M. Rahman, M. Y. A. Mollah, and M. A. B. H. Susan, in *Innovations in Nanomaterials*, ed. A.-N. Chowdhury, J. Shapter and A. B. Imran, Nova Publishers, New York, **2014**, pp. 195-227.